University of Groningen

Radium Ion Spectroscopy

Giri, Gouri Shankar

IMPORTANT NOTE: You are advised to consult the publisher's version (publisher's PDF) if you wish to cite from it. Please check the document version below.

Document Version
Publisher's PDF, also known as Version of record

Publication date:
2011

Link to publication in University of Groningen/UMCG research database

Citation for published version (APA):
Giri, G. S. (2011). *Radium Ion Spectroscopy: Towards Atomic Parity Violation in a single trapped Ion*. s.n.

Copyright
Other than for strictly personal use, it is not permitted to download or to forward/distribute the text or part of it without the consent of the author(s) and/or copyright holder(s), unless the work is under an open content license (like Creative Commons).

The publication may also be distributed here under the terms of Article 25fa of the Dutch Copyright Act, indicated by the “Taverne” license. More information can be found on the University of Groningen website: https://www.rug.nl/library/open-access/self-archiving-pure/taverne-amendment.

Take-down policy
If you believe that this document breaches copyright please contact us providing details, and we will remove access to the work immediately and investigate your claim.

Downloaded from the University of Groningen/UMCG research database (Pure): http://www.rug.nl/research/portal. For technical reasons the number of authors shown on this cover page is limited to 10 maximum.

Download date: 03-06-2022

Radium Ion Spectroscopy Towards Atomic Parity Violation in a Single Trapped Ion

To My Parents

Cover: First ever optical signal of trapped radium ions in a radiofrequency quadrupole trap. This is the fluorescence light at 468 nm which is collected from the trapped $^{212}\mathrm{Ra}^{+}$ cloud and imaged onto a photomultipler tube.

This work has been performed as part of the research program of the "Stichting voor Fundamenteel Onderzoek der Materie" (FOM) through programme 114 (TRIμP), which is financially supported by the "Nederlandse Organisatie voor Wetenschappelijk Onderzoek" (NWO). Additional funding was provided by the European Comission under contract HPRI-CT-2001-50034 (NIPNET) and HPRI-CT-2001-50022 (Ion Catcher).

Druk: Facilitair Bedrijf, University of Groningen, Groningen, August 2011

RIJKSUNIVERSITEIT GRONINGEN

Radium Ion Spectroscopy Towards Atomic Parity Violation in a Single Trapped Ion

Proefschrift

ter verkrijging van het doctoraat in de
Wiskunde en Natuurwetenschappen
aan de Rijksuniversiteit Groningen
op gezag van de
Rector Magnificus, dr. E. Sterken,
in het openbaar te verdedigen op
maandag 3 oktober 2011
om 16.15 uur

door

Gouri Shankar Giri

geboren op 16 mei 1981
te Nalagaja, India

Promotor: Prof. dr. K. H. K. J. Jungmann

Copromotor: Dr. L. Willmann

Beoordelingscommissie: Prof. dr. R. Morgenstern

Prof. dr. B. P. Das

Prof. dr. G. zu Putlitz

ISBN: 978-90-367-5058-5 (Printed Version)
ISBN: 978-90-367-5057-8 (Digital Version)

Contents

1 Introduction 1

1.1 The Standard Model and its Limits . . . 1

1.2 Outline of the Thesis . . . 2

2 Atomic Parity Violation and Standard Model 7

2.1 Parity Violation . . . 7

2.1.1 The Discrete Symmetries . . . 7

2.1.2 History of Parity Violation . . . 8

2.1.3 Electroweak Unification . . . 9

2.1.4 Experiments Worldwide . . . 11

2.2 Parity Violation Experiments . . . 14

2.2.1 Parity Violation in Atomic Systems . . . 14

2.2.2 APV: Low Energy Test of the SM . . . 16

2.2.3 Principle of APV Experiments . . . 17

3 Measuring Parity Violation in a Trapped Ion 19

3.1 Heavy Alkaline-earth Ions: Ba^+ and Ra^+ . . . 19

3.1.1 Atomic Properties of Ra^+ . . . 20

3.1.2 Atomic Properties of Ba^+ . . . 22

3.2 Ra^+: An Ideal Candidate for APV Experiment . . . 23

3.3 Signature of Parity Violation in Ra^+ . . . 24

4 Experimental Methods and Tools 27

4.1 Radium Isotope Production . . . 27

4.1.1 The AGOR Cyclotron and Ra Production Target Station . 28

4.1.2 Double Magnetic Separator . . . 29

4.1.3 Thermal Ionizer . . . 32

4.1.4 Wien Filter . . . 34

- 4.1.5 Results of Radium Production Experiments 35
- 4.2 Radium Ion Trapping and Spectroscopy 40
  - 4.2.1 Trapping in a Radio Frequency Quadrupole 40
  - 4.2.2 Spectroscopy of Trapped Radium in RFQ 42
  - 4.2.3 Trapping and Spectroscopy in a Linear Paul Trap 43
- 4.3 Lasers 49
  - 4.3.1 Lasers for Ra^+ 49
  - 4.3.2 Lasers for Ba^+ 52
  - 4.3.3 Overlap of Beams and Measurement of Spot Size 53
- 4.4 Spectroscopy 54
  - 4.4.1 Absolute and Relative Frequency Calibration 54
  - 4.4.2 Imaging System and Optical Detection 57
- 4.5 Computer Control and Data Acquisition 58

5 Spectroscopy of Short-Lived Radium Isotopes in an Ion Trap 59
- 5.1 Hyperfine Structure Interval of $6d\ ^2D_{3/2}$ State 59
- 5.2 Isotope Shifts 64
  - 5.2.1 Isotope Shifts of $6d\ ^2D_{3/2}$ - $7p\ ^2P_{1/2}$ Transition 65
  - 5.2.2 Isotope Shifts of $6d\ ^2D_{3/2}$ - $7p\ ^2P_{3/2}$ Transition 67
  - 5.2.3 Data Analysis and Results 69
- 5.3 Lifetime of Metastable $6d\ ^2D_{5/2}$ State 73
- 5.4 Conclusion 74

6 Towards Single Ion Parity Violation Measurement 77
- 6.1 Coupling of States 77
- 6.2 The AC Stark Shift 80
- 6.3 A Discussion of Original Proposal 81
  - 6.3.1 The Principle of Measuring the AC Stark Shift 81
  - 6.3.2 Radio Frequency Spectroscopy 83
- 6.4 Future Directions 85

7 Summary of Results and Conclusion 89

8 Samenvatting van de Resultaten en Conclusies 93

Appendices

A Discussion of Ion Trapping 97
A.1 Paul Trap 97
A.2 Stability of Ions in a Trap 100
A.3 Macromotion and Micromotion 101

B Discussion of Hyperfine Structure 105
B.1 Hyperfine Structure Interval 105
B.2 Spins and Electromagnetic Multipole Moments 105
B.3 The Hyperfine Interaction 106
B.3.1 Magnetic Dipole Interaction 106
B.3.2 Electric Quadrupole Interaction 107

C Discussion of Isotope Shift 109
C.1 Isotope Shift 109
C.2 Mass Effect 110
C.3 Field Effect 111

D Settings of the LEBL 115

Bibliography 117

List of Publications 129

Acknowledgment 131

List of Figures

1.1 TRIμP facility concept . . . 3
1.2 Layout of this thesis . . . 4
1.3 Level structure of Ra$^+$ relevant for APV experiment . . . 6

2.1 Interference of weak and electromagnetic interaction . . . 10
2.2 The running of the γ-Z^0 mixing angle . . . 12
2.3 Feynman diagrams depicting atomic parity violation . . . 14

3.1 Level scheme of Ra$^+$ . . . 21
3.2 Level scheme of Ba$^+$ . . . 23
3.3 Level structure of Ra$^+$ showing mixing of states . . . 25

4.1 Operating diagram of AGOR cyclotron . . . 28
4.2 Cross section for ^{204}Pb beam and ^{12}C target vs. beam energy . . . 30
4.3 Cross section for ^{206}Pb beam and ^{12}C target vs. beam energy . . . 30
4.4 Pyrolytic graphite target mounted on a rotating wheel . . . 31
4.5 Schematic diagram of TRIμP separator . . . 32
4.6 Schematic diagram of TRIμP thermal ionizer . . . 33
4.7 Electrostatic extraction from the thermal ionizer . . . 34
4.8 Characteristic α-energy spectrum of Ra$^+$ . . . 36
4.9 Activity for extraction and primary beam on/off measurements . . . 38
4.10 Measured half lives from extraction on/off measurements . . . 39
4.11 Extraction on/off measurements for lighter isotopes . . . 40
4.12 Schematic diagram of TRIμP RFQ . . . 41
4.13 Trapping region of TRIμP RFQ . . . 41
4.14 $6d\ ^2D_{3/2}$ - $7p\ ^2P_{1/2}$ transition in Ba$^+$ . . . 43
4.15 Schematic diagram of low energy beam line . . . 45
4.16 Pulsing sequence of drift tubes . . . 46

4.17 Schematic diagram of linear Paul trap 47
4.18 Alignment of beam line by scanning the voltages 48
4.19 Performance curve of the electrostatic mirror 48
4.20 Mechanical set up of diode lasers in Littrow configuration 51
4.21 Optical layout for trapping and laser spectroscopy 54
4.22 Principle behind frequency calibration 55
4.23 Tellurium absorption signal 56
4.24 Imaging system and optical detection 57

5.1 Level schemes of odd isotopes with hyperfine structure 60
5.2 HFS intervals of 6d $^2D_{3/2}$ and 7p $^2P_{1/2}$ states in ^{213}Ra$^+$ 61
5.3 Hyperfine structure intervals of the 6d $^2D_{3/2}$ states in ^{209,211}Ra$^+$. 62
5.4 Isotope shift of 6d $^2D_{3/2}$ - 7p $^2P_{1/2}$ transition in ^{210,212,214}Ra$^+$ . . . 65
5.5 Isotope shift of 6d $^2D_{3/2}$ - 7p $^2P_{1/2}$ transition in ^{213}Ra$^+$ 66
5.6 Isotope shift of 6d $^2D_{3/2}$ - 7p $^2P_{1/2}$ transition in ^{209,211}Ra$^+$ 66
5.7 Level scheme of ^{213}Ra$^+$ showing a shelving transition 67
5.8 Isotope shift of 6d $^2D_{3/2}$ - 7p $^2P_{3/2}$ transition in ^{212,213,214}Ra$^+$ . . . 68
5.9 King plot of the 1079 nm line in Ra$^+$ 72
5.10 King plot of the 708 nm line in Ra$^+$ 72
5.11 Lifetime of 6d $^2D_{5/2}$ state in ^{212}Ra$^+$ 73
5.12 Lifetime of 6d $^2D_{5/2}$ state in ^{212}Ra$^+$ at different gas pressures . . . 74

6.1 Two level coupling diagram 78
6.2 Illustration of Stark shift on a two level system. 80
6.3 Principle of light shift measurement 82
6.4 Principle of RF Spectroscopy 83
6.5 Light shift in the 6s $^2S_{1/2}$ Zeeman sub-levels in Ba$^+$ 85
6.6 ^{212}Ra$^+$ in a linear Paul trap 86
6.7 An ion trap to confine a single ion 87

7.1 Level schemes of odd isotopes with hyperfine structure 91

8.1 Energieniveaus van oneven isotopen met hyperfijnstructuur 95

A.1 Mechanical model of dynamic stability 98
A.2 Electrode structure for a two dimensional quadrupole trap 99
A.3 Mathieu stability diagrams 101
A.4 Mathieu stability diagram in three dimensional trap 103

List of Tables

2.1 APV experiments from high energy to low energy scales 13

3.1 Atomic properties of barium and radium 20
3.3 Barium isotopes and their atomic properties 22

4.1 Half lives and production rates for $^{212-214}$Ra 37
4.2 Half lives for $^{209-211}$Ra isotopes 37
4.3 A list of the necessary laser systems for Ba$^+$ and Ra$^+$ 50

5.1 HFS constants $A(6d\ ^2D_{3/2})$ and $A(7p\ ^2P_{1/2})$ of ^{213}Ra$^+$ 63
5.2 HFS constants $A(6d\ ^2D_{3/2})$ and $B(6d\ ^2D_{3/2})$ of ^{209,211}Ra$^+$ 64
5.3 Hyperfine structure intervals of the $6d\ ^2D_{3/2}$ state in ^{209,211,213}Ra$^+$ 64
5.4 Isotope shifts of $6d\ ^2D_{3/2}$ - $7p\ ^2P_{1/2}$ transition in $^{209-214}$Ra$^+$ . . . 70
5.5 Isotope shifts of $6d\ ^2D_{3/2}$ - $7p\ ^2P_{3/2}$ transition in $^{212-214}$Ra$^+$ . . . 71

7.1 Results of radium isotope production 90
7.2 Results of hyperfine structure from radium ion spectroscopy . . . 92
7.3 Results of isotopes shift from radium ion spectroscopy 92

8.1 Resultaten van de productie van radiumisotopen 94
8.2 Resultaten van de hyperfijnstructuurmetingen aan radiumionen . 96
8.3 Resultaten van de metingen van isotoopverschuivingen aan radiumionen 96

D.1 Settings of the low energy beam line 115

Chapter 1

Introduction

1.1 The Standard Model and its Limits

The Standard Model (SM) [1–3] is the theoretical framework which provides a consistent description of three of the four known fundamental interactions in nature, namely the electromagnetic, the weak and the strong interactions [4]. The fourth interaction gravity refuses the quantum field theory approach. The SM is undergoing a continuous development since the past four decades [5] and the SM is known to be the most successful theory in physics. Numerous interesting experiments and measurements have been carried out in this period to discover and to prove different properties of particles and their interactions. Despite its success to describe all experimental observations it is not considered as the ultimate description of nature, because of a lack of explanation for some experimental facts. Such open questions include the masses of the fundamental fermions, the number of particle generations, the large energy difference between electro-weak and grand unification (gauge hierarchy problem), the dominance of matter and antimatter in the universe, and the origin of parity violation. The model has many free parameters that can only be determined experimentally. A number of speculative theoretical extensions to the SM have been suggested in order to explain some of the unanswered questions. Such models include Supersymmetry [6], Technicolor [7], Grand Unified Theory [8], and String Theory [9]. The predictions from such models come either in the form of new possible particles or new possible interactions leading to extended radiative corrections [10]. Those theoretical approaches have no status in physics until they are confirmed by experimental findings. Experimental tests of the SM are therefore motivated to identify the existence of new particles and/or new physical processes that would explain the yet not well understood physical facts observed in nature [11–15].

There are two principally different approaches to test the SM extensions. New particles and interactions can be directly searched for in high energy experiments. The number of facilities to carry out a high energy experiment is limited and the research is done on a large scale of international collaborations. Alternatively, there are precision experiments at lower energies using atomic physics techniques where physical quantities are determined which can be compared to calculations of high accuracy within the established theories and deviations indicate incompleteness of the theory. A significant deviation of the measurement from the calculation leads to an indication of new physics. This approach is complementary to high energy experiments and can probe physics at mass scales well above the direct access to the present and near future generation accelerators.

1.2 Outline of the Thesis

The motivation of the TRIμP (Trapped Radioactive Isotopes: μ-laboratories for fundamental Physics) research program at the Kernfysisch Versneller Instituut (KVI) of the University of Groningen is to test fundamental interactions and symmetries in nature. Through precision experiments experimental signatures of the breaking of discrete symmetries are searched for. Of particular interest are the time reversal symmetry (T) and the parity symmetry (P). The TRIμP facility provides short-lived radioactive isotopes which can be studied as atoms or ions in suitable traps [16–20] (Fig.1.1).

This work is concerned with the development of an experimental setup to carry out a state-of-the-art atomic parity violation (APV) measurement on a single trapped ion. APV in this trapped ion will be measured via a determination of light shift of the Zeeman levels of the low lying ground and metastable states. Such a measurement will yield the weak charge of the radium ion nucleus from which the weak mixing angle will be extracted. This measurement will test the SM in a complementary way to other approaches. A sub-percent accuracy is aimed for comparing it to the high energy physics experiments. In particular, the electroweak mixing angle or the Weinberg angle is aimed for with a sub-percent accuracy or a 5 fold improvement over the best existing measurement which was performed on atomic cesium [22–24]. Recently Ra^+ has been identified to be an excellent candidate for this experiment [25, 26]. Due to the unique atomic

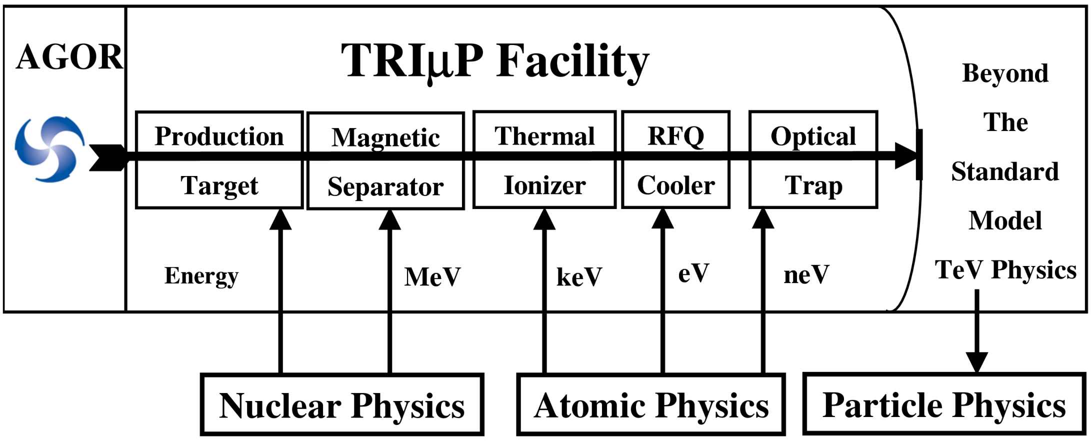

Fig. 1.1: Conceptual view of the TRIμP facility and the TRIμP research program. Radioactive ion beams are produced in nuclear reactions with the beam from the AGOR cyclotron and the production target. A magnetic separator is used to select isotopes of interest. A thermal ionizer and a radio frequency quadrupole cooler convert the high energetic particles to ion or atom beams at thermal energies. Optical traps provide the experimental environment to store and perform high precision measurements with the goal to search for physics beyond the SM [21].

and nuclear structure, sensitivity to the parity violating weak interaction effects in this alkali like system is strongly enhanced. To exploit this enhancement an experiment is being developed within the TRIμP research program at KVI. APV experiments probe the electroweak interaction as described in the SM of particle physics. The agreement with the SM on parity violation could reveal the existence of new physics beyond the SM and guide model building [27,28]. As an example, the current agreement between the cesium measurement and the SM provides a lower mass limit on an additional Z' boson at 1.3 TeV/C^2 [29].

The thesis describes the necessary steps towards a new APV measurement in a new system Ra$^+$ (Fig. 1.2). In the framework of this thesis, a setup for this experiment has been developed based on the requirements of the measurement. Some of the experimental parameters have been investigated by several measurements. The planned parity violation experiment is technically challenging and a long-term project in scope. The first step is the production of radium at the TRIμP facility at KVI. The produced high energetic radium isotopes are thermalized to singly charged ions. The ions are trapped and cooled in a linear Paul trap where precision laser spectroscopy is performed to search for essential

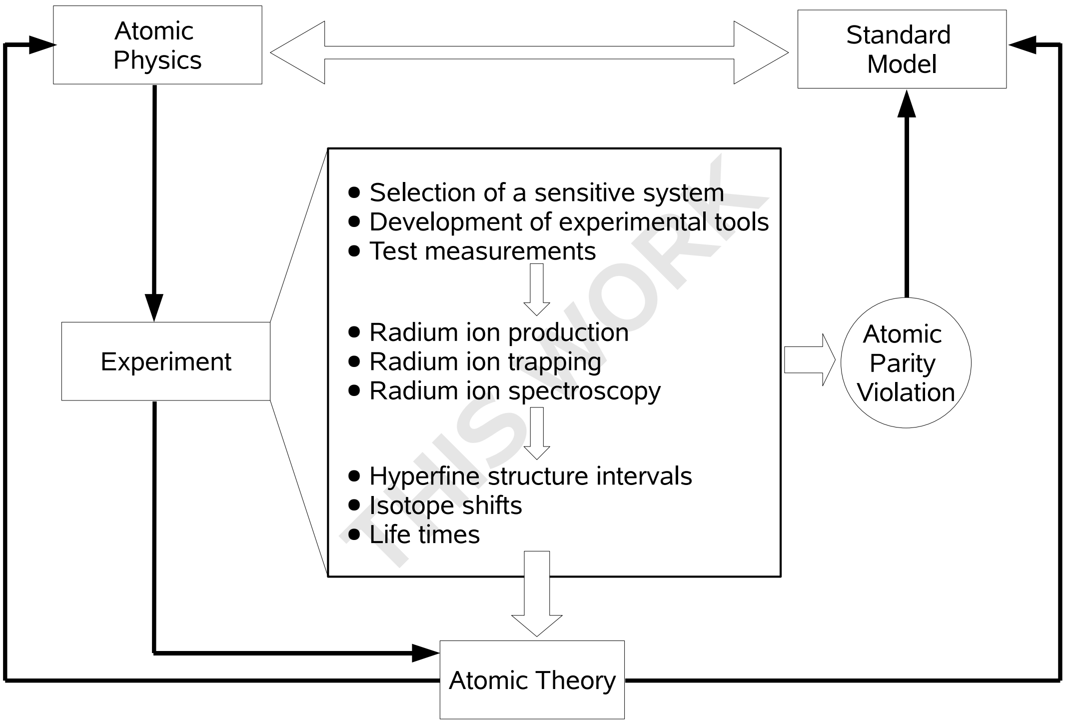

Fig. 1.2: Depiction of the layout of this thesis. Atomic physics techniques are used to precisely measure atomic parity violation enabling a low energy test of the Standard Model. On one hand atomic theory is indispensable to interpret the experimental results and on the other hand the required atomic theory needs experimental input. This work is concerned with the development of necessary experimental tools and leads to important physics results that are required to test the atomic theory.

atomic, nuclear and spectroscopic properties in this system which are scarce in literature. This work provides indispensable building blocks for the parity violation measurement in the radium system. It is at the overlap of many different fields in experimental and theoretical physics.

This thesis is organized as follows.

- We start with a description of violation of parity symmetry in an atomic system. The experimental effort is placed into context with worldwide parity violation research. The principle of measurement of parity violation in general is also discussed.

- We describe the general requirements of an atomic system to be a potential candidate for this experiment. We compare Ra^+ with other candidates (Ba^+, Yb^+, Fr and Cs). The observable for APV is presented.

- The tools that have been developed are introduced. The TRIμP facility is discussed with an emphasis on the operation of different components of the facility for radium production. The experimental results of radium isotope production are presented and discussed. Special attention has been given to ion traps which are dedicated to this experiment. The laser systems are described extensively with emphasis given to frequency calibration.

- The results from the measurements of hyperfine structure, isotope shift and lifetime are presented. Data analysis and interpretation of the results are discussed with emphasis given to isotope shifts.

- We summarise the results of radium isotope production and the results of laser spectroscopy. The importance of the results towards the planned APV experiment is discussed.

- We conclude with an outlook. The principle of measurement of differential light shift by RF spectroscopy using shelving technique is discussed. The current status of the experiment and an overview of short-term plans are presented.

Ra^+ is the heaviest alkaline-earth ion for which a high precision measurement of atomic parity violation can be carried out. At the same time one can expect that the achievable precision depends on a precise atomic description of this system. The sensitivity to parity violating effects in this alkali like system is 50 times higher than in cesium where the best such measurements have been performed till date [22, 23, 29, 30]. The energy levels of Ra^+ which are relevant for this work are shown in Fig. 1.3. It is a particular advantage of Ra^+ that all transitions relevant for an APV measurement are accessible with commercially available cost effective diode laser systems.

The concept for an APV experiment based on a single ion has been worked out for Ba^+ [31–33]. However, the relative strength of the APV signal is 20 times larger for Ra^+ [26] and an experiment to exploit this enhancement is currently developed within the TRIμP research program at KVI. The experiment aims at a 5 fold improved measurement of the weak mixing angle over the sole best APV result in atomic cesium.

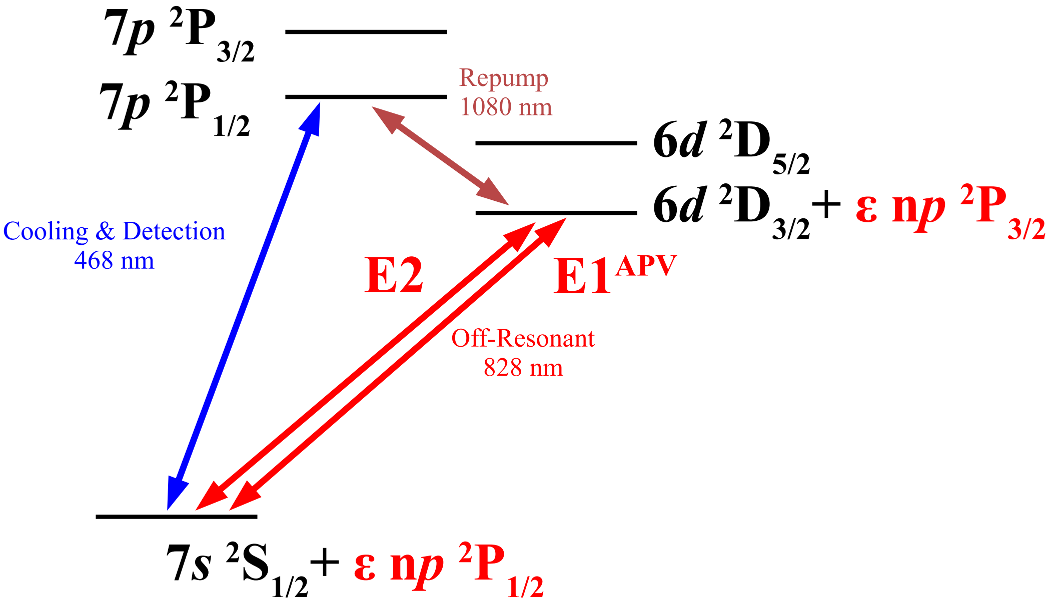

Fig. 1.3: Level diagram of Ra^+ with emphasis given to the admixture of P states with the low lying S and D states.

A parity violation experiment requires a good study of possible systematic effects. This work developed the principle and realization of production of short-lived radium isotopes, the subsequent trapping and laser spectroscopy in a linear Paul trap. The next steps towards trapping and cooling of a single ion is underway.

Chapter 2

Atomic Parity Violation and Standard Model

2.1 Parity Violation

2.1.1 The Discrete Symmetries

There are three discrete symmetries in the description of the SM. They are the parity (P) symmetry, the time reversal (T) symmetry, and the charge conjugation (C) symmetry. The parity symmetry was introduced by Wigner in 1927 to explain the selection rules observed in atomic transitions [34]. Parity is the operation of space reflection, where all spatial coordinates $\vec{r} \equiv (\vec{x}, \vec{y}, \vec{z})$ are reversed through the origin. Mathematically, it is represented by the operator $\hat{P}$ which transforms

$$\begin{gathered} \hat{P}\ \vec{r} = -\vec{r} \\ \hat{P}\ \psi(\vec{r}, t) = \psi(-\vec{r}, t). \end{gathered}$$

In quantum mechanics the parity operator has a quantum number associated with it. Since $\hat{P}^2\psi = \psi$ the parity operator $\hat{P}$ has two eigenvalues: +1 and -1 corresponding to even and odd parity eigenstates respectively.

The time reversal symmetry was also introduced by Wigner in 1932 [35]. The time reversal symmetry transformation is represented by an operator $\hat{T}$ which reverses the time coordinate

$$\begin{gathered} \hat{T}\ t = -t \\ \hat{T}\ \psi(\vec{r}, t) = \psi(\vec{r}, -t). \end{gathered}$$

The time reversal operation relates the initial and final states in quantum mechanics and it has no quantum number associated with it.

The charge conjugation symmetry was introduced by Kramers in 1937 following the formulation of the Dirac equation and the development of quantum field theory [36]. It is often called particle-antiparticle conjugation [37]. The charge conjugation symmetry transformation is represented by the operator $\hat{C}$ which reverses the charge

$$\begin{aligned} \hat{C}\ q &\rightarrow -q \\ \hat{C}\ \psi(q) &\rightarrow \psi(-q). \end{aligned}$$

In 1951, Schwinger formulated the CPT theorem which states that the combined CPT operation is a symmetry of any local Lorentz-invariant quantum field theory [38]. The prediction of the SM and confirmation from all experimental observations indicate that all physical laws are invariant under the combined application of all three discrete symmetries ($\hat{C}\hat{P}\hat{T}$) irrespective of their order. Individually, these symmetries are not preserved by nature. Soon after the formulation of CPT theorem, violation of different discrete symmetries were observed after the suggestion to search for it in the weak interaction by Lee and Yang [39]. We will discuss only the violation of parity symmetry in the scope of this thesis.

2.1.2 History of Parity Violation

A physical law conserves the parity symmetry if its form is retained under a parity transformation operation. Parity is conserved if left and right can not be distinguished by performing a physical experiment. It is quite evident that one can not simply apply an abstract transformation operator to the experimental apparatus to get some sense of parity violation. However, one can effectively do this by reversing the parity of the experiment. In order to search for a signature of parity violation, an experiment is performed to measure some physical process and the measurement is repeated with the parity of the experiment reversed. Any discrepancy observed between the two measurements is the basic signature of parity violation and it would imply a fundamental handedness[1] associated with the physical process.

In order to understand the present status of the physics of parity violation, it is illuminating to look at the path of discoveries. Here we present the milestones in the history of significant developments in the field of parity violation.

- **Until 1950**, almost every physicist had a notion that parity is a fundamental symmetry of the universe.

---

[1] The handedness has also been observed in muon decay.

- **In 1950**, E.M. Purcell and N.F. Ramsey realized that a permanent electric dipole moment (EDM) of a fundamental particle would violate the parity symmetry [40]. This was the beginning of the searches for EDM which have set over the decades strong limits on SM extensions. They also indicated that there was no limit on parity violation for the weak interaction.

- **In 1956**, T.D. Lee and C.N. Yang predicted that the weak force might violate parity symmetry based on their theoretical work on $\tau-\theta$ puzzle [39]. They proposed experiments that could test their prediction. They were later awarded the Nobel Prize for this work. Several experiments were started thereafter.

- **In 1957**, C. Wu et al. performed a significant variation of the experiment proposed by Lee and Yang which led to the first observation of parity violation in nuclear β-decay [41]. Many experiments followed thereafter.

- **In 1959**, Zeldovich speculated that neutral currents might be the cause that leads to parity violating effects in atomic systems and not just in nuclear β-decay [42]. This speculation created an interest among experimentalists, though it was apparent that the effects would be immeasurably small at that time.

- **In 1967**, S.L. Glashow, S. Weinberg, and A. Salam proposed the electroweak theory which unifies electromagnetism with the weak force [1–3]. This unified gauge theory predicts the existence of a massive Z^0 boson which is responsible for the parity violating weak interaction effects.

- **In 1974**, M.A. Bouchiat and C.C. Bouchiat realized that parity violation effects are stronger in heavy atomic systems and the strength of the effects scales with the cube of atomic number (Z^3 law) [43]. This triggered the beginning of a new era of experiments to search for neutral current effects in atomic systems. Since then, there have been several groups pursuing experimental measurements of atomic parity violation in heavy atomic systems [22–24, 30–33, 44–50, 50–53].

2.1.3 Electroweak Unification

The long range electromagnetic interaction in atomic systems is mediated by the exchange of a massless photon (γ). This interaction is parity conserving and is described by the laws of Quantum Electrodynamics (QED). The short range weak interaction is mediated by the exchange of a weak vector boson. This interaction is parity violating. The electroweak theory claims that all electromagnetic phenomena and all weak phenomena are results of the manifestation of one universal electroweak interaction between spin 1/2 quarks (up, down, top, bottom, charm, strange) and leptons (electron, muon, tau, neutrinos) mediated by four spin 1 bosons: two charged ones (W^+ and W^-) and two neutral ones (W^0 and B^0). These four particles are the eigenstates of weak interaction. However, they are not the mass eigenstates. The two charged vector bosons (W^+ and W^-) cannot mix because of their electric charge while the neutral bosons (W^0 and B^0) mix in two orthogonal linear combinations. In one linear combination, the photon remains massless and the coupling strength is given by the charge of the electron. The consistency of the theoretical framework required the existence of a massive second neutral boson Z^0 ($\sim$ 91 GeV) which was predicted by the electroweak theory. The mixing of the photon (γ) and the Z^0 boson (*cf.* Fig. 2.1) is described by a single fundametral parameter, the weak mixing angle or the Weinberg angle (θ_W). The mass eigenstates in terms of the linear combinations of neutral bosons are written as

$$|\gamma\rangle = \sin\theta_W|W^0\rangle + \cos\theta_W|B^0\rangle \tag{2.1}$$

$$|Z^0\rangle = \cos\theta_W|W^0\rangle - \sin\theta_W|B^0\rangle. \tag{2.2}$$

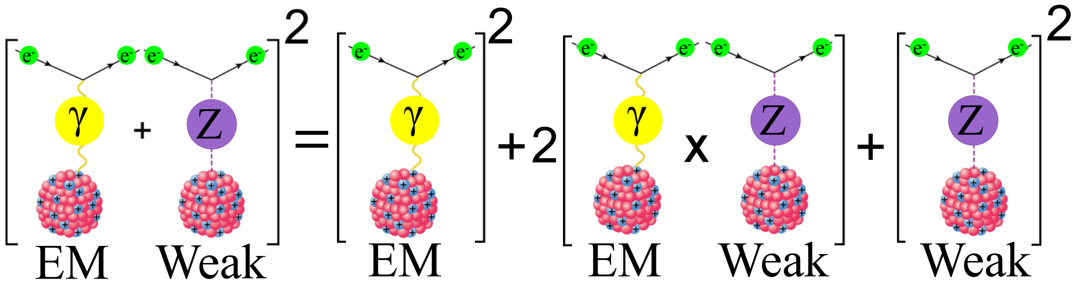

Fig. 2.1: Electrons in an atom interact with the nucleus through the electromagnetic force (EM) via the exchange of massless photons (γ). The weak force (Weak) is mediated by Z^0 bosons. The weak effects by themselves are too small to be seen directly. This figure provides a pictorial representation of the quantum interference between the electromagnetic and weak processes. The sum of the amplitudes squared enables to observe the effect of Z^0 boson exchange. Adapted from [54].

If the mediating particle is a charged vector boson (W^+ or W^-), the interaction is called *charged current interaction*, e.g., nuclear β-decay. If the mediating particle is a neutral vector boson (Z^0), the interaction is called *neutral current interaction*. The existence of Z^0 boson and the neutral current interaction was confirmed by indirect observation of neutral current processes [55, 56] and later by direct observation of the Z^0 resonance [57, 58]. Over the years the accelerator based high energy experiments have confirmed the predictions of the electroweak theory with great precision.

The weak mixing angle θ_W connects two independent coupling constants of the electroweak theory. One is the electric charge (e), the coupling constant of the electromagnetic interaction. The other is g_W, the coupling constant of the weak interaction. These two coupling constants are connected to the Weinberg angle via the relation

$$\sin^2 \theta_W = \frac{e^2}{g_W^2}. \tag{2.3}$$

Since electroweak theory is a quantum field theory, these two coupling constants vary with the energy at which they are measured due to radiative corrections. The prediction of the electroweak theory for the running of Weinberg angle is shown in Fig. 2.2.

It shows that $\sin^2 \theta_W$ first decreases by about $\sim 3\%$ from low energy to the mass of the Z^0 boson. This is caused by the creation and annihilation of quark-antiquark pairs resulting in the vacuum polarization which shields the interacting particles, causing g_W to increase. At very high energy (beyond 100 GeV) the $W^\pm$ pairs start to dominate vacuum polarization resulting in anti-shielding, causing g_W to decrease and $\sin^2 \theta_W$ to increase. This prediction of the SM is confirmed by several experiments and several experiments are underway.

2.1.4 Experiments Worldwide

Here we restrict ourselves to the APV experiments aiming for a precise determination of Weinberg angle. A number of such experiments have been performed at different energy scales, each of which has contributed an experimentally measured value of the Weinberg angle. These experiments along with the planned experiments are listed in Table 2.1.

The e^+e^- experiment performed at LEP, CERN (LEP 1 in Fig. 2.2) yielded a result that defines θ_W at the Z^0 pole. This is the most precise measurement performed at high energy frontier. Interestingly the leptonic (0.23113 ± 0.00021) and the hadronic (0.23222 ± 0.00027) measurements of $\sin^2 \theta_W$ differ by 3.2σ [62]. Two other experiments at this energy scale were performed at SLC (SLAC) and

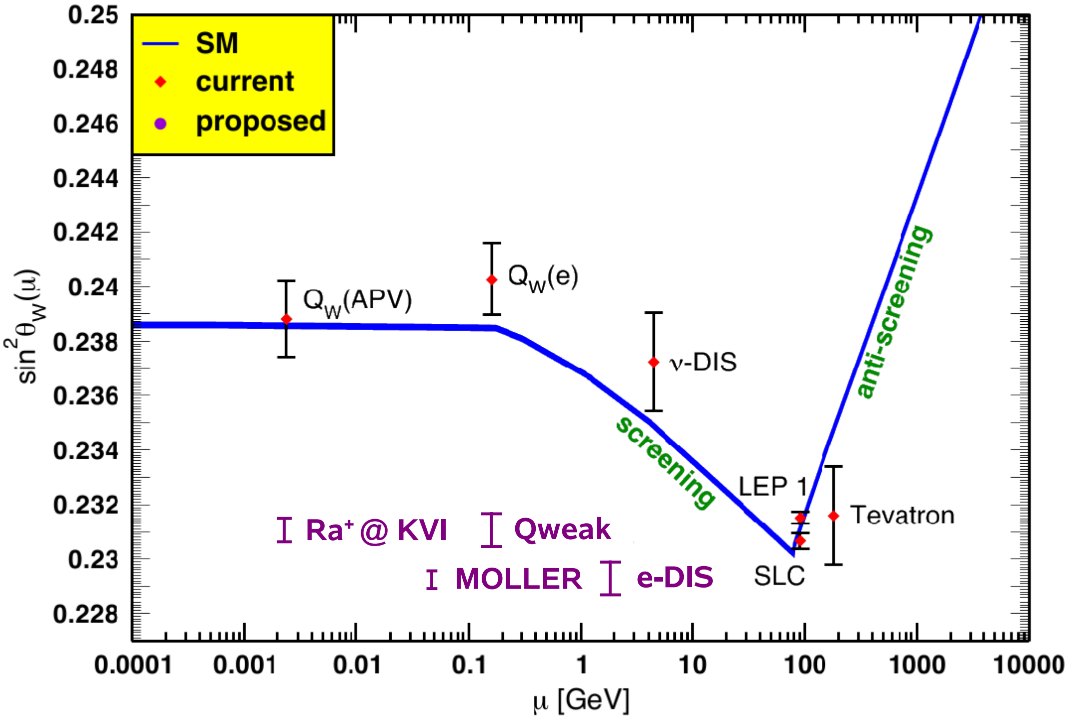

Fig. 2.2: The running of the γ-Z^0 mixing angle from low atomic energies to the high energy scales. The blue trace is the prediction of the SM. The data points in red color are the completed or ongoing experiments. The data points in magenta color are proposed experiments with the anticipated error bars. Adapted from [59].

Tevatron (Fermilab) [63].

The NuTeV experiment at Fermilab (ν-DIS in Fig. 2.2) determined the Weinberg angle by looking at the scattering of the beams of neutrinos and antineutrinos off a proton target. The interaction between the (anti)neutrinos and the quarks can be either a charged or a neutral weak current. By determining the ratio of the charged to neutral current cross sections for either the neutrino or antineutrino beam, a value of the Weinberg angle was extracted. The final report was published in 2002 with a value for $\sin^2\theta_W$ that differed from the SM prediction by 3σ [61].

The E158 experiment at SLAC (Q_W(e) in Fig. 2.2) determined the weak charge of the electron by looking at the amount of parity violation in electron-electron scattering. The measurement was performed by accelerating polarized electrons to $\sim$ 50 GeV and scatter them off other electrons in a liquid hydrogen target. Since the Z boson couples differently to left handed electrons than to

Table 2.1: Recent APV experiments from low energy to high energy scales. Experiments marked with an asterisk have been proposed. The last column indicates the level of precision that has been achieved or anticipated.

Measurement	Laboratory	Observable	Precision
Cs APV	Q_W(APV)@JILA Boulder	Q_W(Cs)	0.35% [22]
ee scattering	E158@SLAC	Q_W(e)	0.5% [60]
ν-DIS	NuTeV@Fermi Lab	-	0.7% [61]
e^+e^- at Z^0 pole	LEP@CERN	-	0.07% [62]
ep scattering*	Qweak@J-Lab	Q_W (p)	0.3%
ee scattering*	Moller@J-Lab	Q_W (e)	0.1%
e-DIS*	J-Lab	Q_W (e)	0.45%
Fr APV*	Legnaro	Q_W(Fr)	-
Ba^+ APV*	Seattle	$Q_W(Ba^+)$	0.5%
Yb^+ APV*	Los Alamos	$Q_W(Yb^+)$	0.1%
Ra^+ APV*	Groningen	$Q_W(Ra^+)$	3%

right handed electrons, the polarized electron beam is scattered differently depending on its polarization. This leads to a parity violating asymmetry. The determination of parity violation leads to the determination of the Weinberg angle. The first data was collected in the summer of 2004 [64] and the final report was published a year later [60].

Several experiments are planned to be performed in the medium energy sector. The Qweak experiment at the Jefferson Lab (J-Lab) aims to measure the weak charge of the proton $Q_W(\mathrm{p})$ by elastic electron-proton scattering. The Moller experiment and e-DIS experiment at J-Lab aim to measure the weak charge of electron $Q_W(\mathrm{e})$.

In the lower energy sector, there exists only one measurement which determined the weak nuclear charge with a sub-percent accuracy [22]. The result of this measurement agrees to better than one standard deviation with the prediction of the SM (*cf.* Fig. 2.2). This level of agreement is a consequence of tremendous theoretical effort that was pursued to achieve the level of accuracy called for by the experimental result [29, 65]. Over the years the theoretical prediction has relaxed towards the experimental value about a decade after the final experimental number. Then it becomes desirable to perform an independent high precision measurement of the weak charge in Cs or in a different system using a completely different experimental concept. Several groups are pursuing this goal. For cesium (Z=55), a new measurement was performed by the ENS-Paris group [30] and plans exist at SUNY, Stony Brook. At INFN, Legnaro an experiment is planned to measure the weak charge for francium (Z=87) in a magneto optical trap (MOT). At Seattle an experiment to measure the weak charge for Ba^+(Z=56) is underway. At Los Alamos an experiment is planned to measure the weak charge for Yb^+ (Z=70). At KVI, we are preparing a competitive APV experiment using a single trapped ionic radium (Z=88).

2.2 Parity Violation Experiments

2.2.1 Parity Violation in Atomic Systems

Parity violation in atomic systems is caused by the interaction of electrons with the quarks in the nucleus through the exchange of Z^0 bosons. This interaction can be depicted using a Feynman diagram (Fig. 2.3). In the left diagram the parity violation of an electron due to a t-channel interaction with a Z^0 boson inside the nucleus is shown. In the right diagram it is shown that the weak interactions can be treated in a contact potential approximation, with G_F being the point contact coupling constant. It is related to the underlying physical weak force coupling constant g_W as $G_F \propto g_W$ [66].

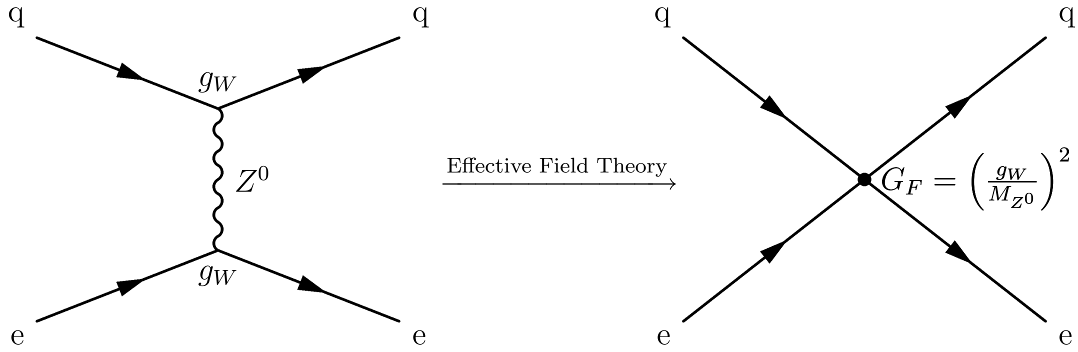

Fig. 2.3: Feynman diagrams depicting atomic parity violation. The left diagram shows the interaction of an electron (e) with a quark (q) with an exchange of Z^0 boson. The right diagram shows the coupling of four fermions in a contact potential approximation using effective field theory.

The dominant contribution to atomic parity violation comes from the exchange of the Z^0 between the electrons and the quarks in the nucleus, where the

Z^0 couples to the spin of the electron and to the weak charge of the quarks. As a result of coherent addition of the weak charges of each quark, the nucleus acquires a weak nuclear charge (Q_W). This weak interaction introduces a non-zero off-diagonal matrix element in the energy eigenstate representation of $\hat{P}$. As a result, the energy eigenstates will not have a well defined parity. A state of well defined parity gets a tiny admixture from opposite parity states and becomes a state of ill defined parity. This mixing is maximum between the states for which the overlap of electron wave functions at the nucleus is maximum. Far away from the nucleus, the exchange of Z^0 bosons between the electrons and the quarks is suppressed because of the large mass of Z^0.

The weak charge Q_W of the nucleus is expressed as

$$\begin{aligned} Q_W &= (2Z+N)Q_w(u) + (Z+2N)Q_w(d) \qquad (2.4) \\ &= [Q_w(u) + 2Q_w(d)]N + [2Q_w(u) + Q_w(d)]Z, \qquad (2.5) \end{aligned}$$

where N is the number of protons and Z is the number of protons inside the nucleus. Using the values of the weak charges of the up (u) and down (d) quarks according to the electroweak theory, the weak nuclear charge takes the form

$$Q_W = -N + (1 - 4\sin^2\theta_W)Z. \qquad (2.6)$$

Experimentally, the value of $\sin^2\theta_W$ has been determined to be $\simeq$ 0.23 [62]. Thus $Q_W \simeq$ - N + 0.08 Z $\sim$ -N, and hence the weak nuclear charge is roughly proportional to the atomic number Z. The extent to which the admixed opposite parity states overlap at the nucleus is roughly proportional to Z^2. Combining these two facts together leads to a conclusion that the amplitude of mixing effect is proportional to Z^3 [43].

The neutral weak interaction between an atomic electron and the nucleus is described by a zero-range effective Hamiltonian which is added as a perturbation to the usual Coulomb Hamiltonian. The parity violating part of the electron-nucleus interaction Hamiltonian H^{APV} can be expressed as

$$H^{APV} = H_1^{NSI} + H_2^{NSD}, \qquad (2.7)$$

where H_1^{NSI} is the nuclear spin independent contribution and H_2^{NSD} is the nuclear spin dependent contribution. H_1^{NSI} is a scalar in the electronic variables. Thus, it is unable to change the angular momentum of the electron. H_1^{NSI} can be expressed as

$$H_1^{NSI} = A_e V_N, \qquad (2.8)$$

where A_e is the axial vector component of the electronic neutral weak current and V_N is the vector component of the nucleonic neutral weak current.

H_2^{NSD} is dependent on the nuclear spin and plays a role only in the odd isotopes. It can change the electron angular momentum. H_2^{NSD} actually consists of two parts,

$$H_2^{NSD} = H_{2a}^{NSD} + H_{2b}^{NSD}. \tag{2.9}$$

The first part (H_{2a}^{NSD}) originates from unbalanced nucleon spin and is equal to $V_e A_N$, where V_e is the vector component of the electronic neutral weak current and A_N is the axial vector component of the nucleonic neutral weak current. The second part (H_{2b}^{NSD}) originates from the electromagnetic coupling of the electrons to the nuclear anapole moment. The combined nuclear spin dependent contribution $H_2^{NSD} = H_{2a}^{NSD} + H_{2b}^{NSD}$ is only a few percent of the nuclear spin independent contribution H_1^{NSI}. The study of isotopes with zero and non-zero nuclear spin can distinguish these contributions.

In the non-relativistic limit, H_1^{NSI} can be written as [67]

$$H_1^{NSI} = Q_W \times \frac{G_F}{2\sqrt{2}} \gamma_5 \rho_N(r), \tag{2.10}$$

where Q_W is the weak nuclear charge, G_F is the weak coupling constant or Fermi constant, γ_5 is the Dirac matrix and $\rho_N(r)$ is the nucleon density function. $\rho_N(r)$ is non-zero only for nuclear dimensions and it is essentially a delta function. It can be either the proton density function or the neutron density function and both of them can be assumed to be the same. Nevertheless the nuclear parameter plays a role in the interpretation of the weak interaction results. Hence the parameters such as charge radii, hyperfine structures and lifetimes have to be determined experimentally.

2.2.2 APV: Low Energy Test of the SM

While the strong and electromagnetic interactions are parity even, the weak interaction is parity odd. Hence a measurable parity violating effect in an atomic system can only be explained by the weak interaction. Measuring parity violation via a low energy precision experiment and finding agreement with the SM to a sub-percent accuracy would exclude new bosons with a mass < 1 TeV, which is already better than the capabilities of current high energy experiments. On the other hand, any deviation would indicate “new physics” beyond the SM.

The interface between an atomic parity violation experiment and the SM is the weak nuclear charge, Q_W. The weak charge Q_W is obtained by combining the results of atomic parity violation experiments and relativistic many-body calculations. Thus, a parity violation experiment in conjunction with required atomic theory can determine an experimental value of the weak nuclear charge Q_W, from which the weak mixing angle θ_W can be extracted and compared with the standard model prediction shown in Fig. 2.2.

2.2.3 Principle of APV Experiments

Due to the Z^0 induced mixing of states, there is a small but non-zero parity violating transition amplitude (A^{PV}) between states of the same parity. The amplitude A^{PV} will change sign if parity of the experiment is effectively reversed, for example, by reversing the directions of electric, magnetic, and laser fields [22,50], while all parity conserving amplitudes will remain unchanged under this reversal. The goal of an APV experiment is to precisely determine this parity violating amplitude A^{PV} which is observed by its interference with either a parity conserving transition amplitude (A^{PC}) or another parity violating transition amplitude that can be induced externally.

The amplitude A^{PC} can be a magnetic dipole (M1) transition amplitude and this is the basis of an optical rotation experiment. The physics underlying the optical rotation experiment is concerned with the rotation of the plane of polarization of light as it passes through a medium of atoms, owing to the intrinsic chirality of atoms arising from the weak interaction. This APV-induced optical rotation violates mirror symmetry. An excellent description of the optical rotation experiments is given in [68]. Optical rotation experiments have been performed on atomic bismuth [69], lead [70], thallium [71] and samarium [72]. APV experiments based on Stark interference aim at measuring the transition rate between two states, for which there is a parity violating transition matrix element [68, 73]. In such experiments the amplitude A^{PV} can be measured by observing its interference with a Stark-induced electric dipole (E1) transition amplitude. Candidates for such an experiment are atomic cesium [22], ytterbium [50], and francium [74]. Alternatively, the amplitude A^{PC} can be chosen as an electric quadrupole (E2) transition amplitude (Fig. 2.1). Candidates for such an experiment are Yb^+, Ba^+, and Ra^+.

Since the parity violating matrix elements are much smaller than the parity conserving matrix elements, the weakly allowed parity conserving transition completely dominates the experiment. In terms of Rabi frequencies the absolute transition rate between the two states is given by,

$$\begin{aligned} R &=\mid \Omega^{\mathrm{PV}} + \Omega^{\mathrm{PC}} \mid^2 && (2.11) \\ &= |\Omega^{\mathrm{PV}}|^2 + 2\mathrm{Re}\left(\Omega^{\dagger\mathrm{PV}}\Omega^{\mathrm{PC}}\right) + |\Omega^{\mathrm{PC}}|^2 && (2.12) \end{aligned}$$

The first term may be neglected as it depends quadratically on the small parity violating transition amplitude. The last term depends quadratically on the large parity conserving transition amplitude which dominates the transition rate. This indicates that a direct approach of measuring the absolute strength of parity violating transitions is bound to fail and hence one needs to take an indirect approach by exploiting the interference term, which is linear in parity violating amplitude. This interference term is a pseudoscalar and hence it will change sign upon a coordinate system reversal. Since the last term dominates the transition rate, it must be distinguished from the interference term. This can be done by using the parity violating signature of the interference term which makes it behave differently from the parity conserving term under coordinate system reversals.

Trapped heavy atoms and ions are good systems for the measurement of atomic parity violation. Because of the electric charge an ion can be preferred over an atom, since it is easier to manipulate an ion than an atom. Alkali atoms or alkaline-earth ions with a single valence electrons are preferred for such an experiment.

Chapter 3

Measuring Parity Violation in a Trapped Ion

3.1 Heavy Alkaline-earth Ions: Ba^+ and Ra^+

Laser spectroscopy has evolved to be a very powerful technique to determine atomic and nuclear properties of an element including but not limited to the information on the electron shell, the lifetime of excited atomic levels, the nuclear spin, the charge distribution, and the electric/magnetic multipole moment of nuclei. A better knowledge of these properties is essential for a better understanding of the atomic and nuclear structures. For example, hyperfine structures and isotope shifts depend on atomic and nuclear properties respectively. The hyperfine structure intervals enable one to understand the atomic wave functions better. Similarly the isotope shifts enable one to understand the shape and size of atomic nuclei.

Towards a competitive APV experiment, all the atomic and nuclear properties need to be determined for the atomic system of interest in order to extract the small contributions from parity violating weak effects to the atomic structure. The singly charged radium ion (Ra^+) has been identified as an ideal system. However, an extensive study of this system through laser spectroscopy is indispensable to determine the missing atomic and nuclear properties. Since radium is scarce, precious, radioactive and is known to have no stable isotope, it is impossible to investigate them on a daily basis. Hence we developed the experiment with singly charged barium ions (Ba^+), which are chemically homologous to Ra^+ (Table 3.1). Though Ba^+ is a well understood system, very limited spectroscopic information about Ra^+ is available in the literature. In this section, we give an overview of

Table 3.1: Atomic properties of the ionic heavy alkaline-earth elements Ba^+ and Ra^+.

Atomic Property	Ba^+	Ra^+
Atomic number	56	88
Melting point (K)	1000	1196
Electronic configuration	$[Xe]6s^1$	$[Rn]7s^1$
Ground state	$6s\ ^2S_{1/2}$	$7s\ ^2S_{1/2}$
Most abundant isotope	^{138}Ba (71.7%)	^{226}Ra (90%)
Nuclear spin	Even: 0, Odd: 1/2, 3/2	Even: 0, Odd: Many
Number of stable isotopes	7	None[a]

---

[a] The longest lived radium isotope with $I \neq 0$ is ^{225}Ra (I=1/2) and the lifetime is 14.9(2) days. The longest lived radium isotope with I=0 is ^{226}Ra and the lifetime is 1600(7) years.

the known properties of the Ra^+ system and we discuss the informations needed for measuring parity violation in this system.

3.1.1 Atomic Properties of Ra^+

The radioactive element radium was discovered by M. Curie in 1898 and subsequently many short-lived isotopes of radium were found. Ra^+ is an alkaline earth ion. Its atomic number is 88 and the electronic configuration is [Rn] $7s^1$. It is a single valence electron system and the ground state LS configuration is $7s\ ^2S_{1/2}$. Radium has an important role in the understanding of the physics of radioactivity. The activity of one gram of ^{226}Ra is defined as the unit of radioactivity (Ci). The important physical properties of radium are listed in Table 3.1.

Four decades after the discovery of radium, E. Rasmussen in 1933 was the first to perform arc emission spectroscopy of radium atoms [77] and radium ions [76] using a discharge lamp and a grating monochromator. A total of 62 transitions were identified in radium ions [76]. The lines were recorded on a photographic film and the level structure was extracted. These measurements together with the measurements for radium atoms [77,78] confirmed the identification of radium as an alkaline-earth element. The level structure of Ra^+ is shown in Fig. 3.1.

After a long gap of about 50 years, laser spectroscopy of Ra^+ was resumed at the ISOLDE facility of CERN. Radioactive radium isotopes with half life

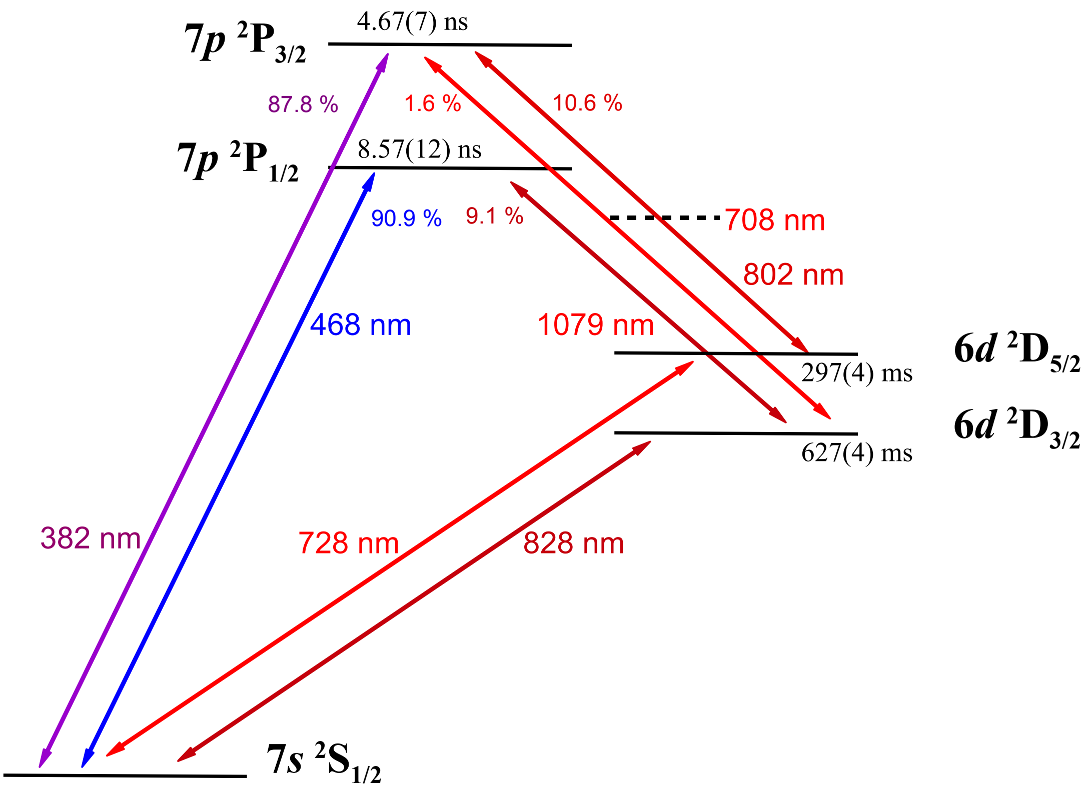

Fig. 3.1: Level diagram of Ra$^+$. Calculated lifetimes and branching ratios are taken from [75]. Wavelengths are taken from [76].

between 23 ms and 1600 y were produced. On-line collinear fast-beam laser spectroscopy was performed on the strong ionic $7s\ ^2S_{1/2}$ - $7p\ ^2P_{1/2}$ transition to measure the hyperfine structures and isotope shifts in a series of radium isotopes in the mass range of $208 \leq A \leq 232$ [79]. These measurements enabled the determination of nuclear spins, magnetic dipole moments, and electric quadrupole moments of those isotopes [79, 80]. Later on, the hyperfine structure and isotope shift measurements were continued for the $7s\ ^2S_{1/2}$ - $7p\ ^2P_{3/2}$ transition [81]. From these measurements the mean square charge radii were extracted [82]. A direct measurement of nuclear magnetic moments of ^{213}Ra and ^{225}Ra was also performed [83].

Due to the unique atomic and nuclear properties, radium isotopes are considered as promising candidates for several high precision experiments. This is the motivation for performing high precision calculations of the necessary atomic wave functions in this system, because precise calculations of many atomic properties such as hyperfine structure, transition rates, excited state lifetimes etc, have a strong dependence on the knowledge of atomic wave functions. The rel-

Table 3.3: Barium isotopes with their nuclear spins, atomic masses, isotopic abundances, and lifetimes [86].

Isotope	Spin	Mass (amu)	Abundance (%)	Lifetime
^{130}Ba	0	129.906282	0.11	Stable
^{132}Ba	0	131.905042	0.10	Stable
^{133}Ba	1/2	132.906008	-	10.5 y
^{134}Ba	0	133.904486	2.42	Stable
^{135}Ba	3/2	134.905665	6.59	Stable
^{136}Ba	0	135.904553	7.85	Stable
^{137}Ba	3/2	136.905812	11.23	Stable
^{138}Ba	0	137.905232	71.70	Stable

ativistic nature of this system makes the calculation challenging. The results of such calculations have serious impact on the interpretation of experimental results and also on the evaluation of sensitivity to symmetry breaking effects. On the other hand, highly precise experimental determination of these quantities provide reliable input for atomic structure calculations.

Several atomic properties such as the transition rates, hyperfine structures, isotope shifts, excited state lifetimes and branching ratios of several states etc. have been calculated by several groups using different theoretical approaches [25, 26, 65, 75, 84, 85]. The calculated results have very little physical significance until they undergo experimental verification. Any possible discrepancy will require physical explanation and further investigation.

3.1.2 Atomic Properties of Ba$^+$

Barium was discovered by H. Davy in 1808. Ba$^+$ is also an alkaline earth ion. Its atomic number is 56 and the electronic configuration is [Xe] $6s^1$. It is a single valence electron system and the ground state LS configuration is $6s\ ^2S_{1/2}$. The level structure of Ba$^+$ is shown in Fig. 3.2.

Ba$^+$ has a similar atomic structure as Ra$^+$. Hence we use Ba$^+$ as a precursor to develop the necessary experimental tools and the laser spectroscopic techniques which we can apply to Ra$^+$. Barium has seven stable isotopes and they are readily available in nature. All the stable barium isotopes with their isotopic abundances are listed in Table 3.3. Ba$^+$ is a well understood system and a large

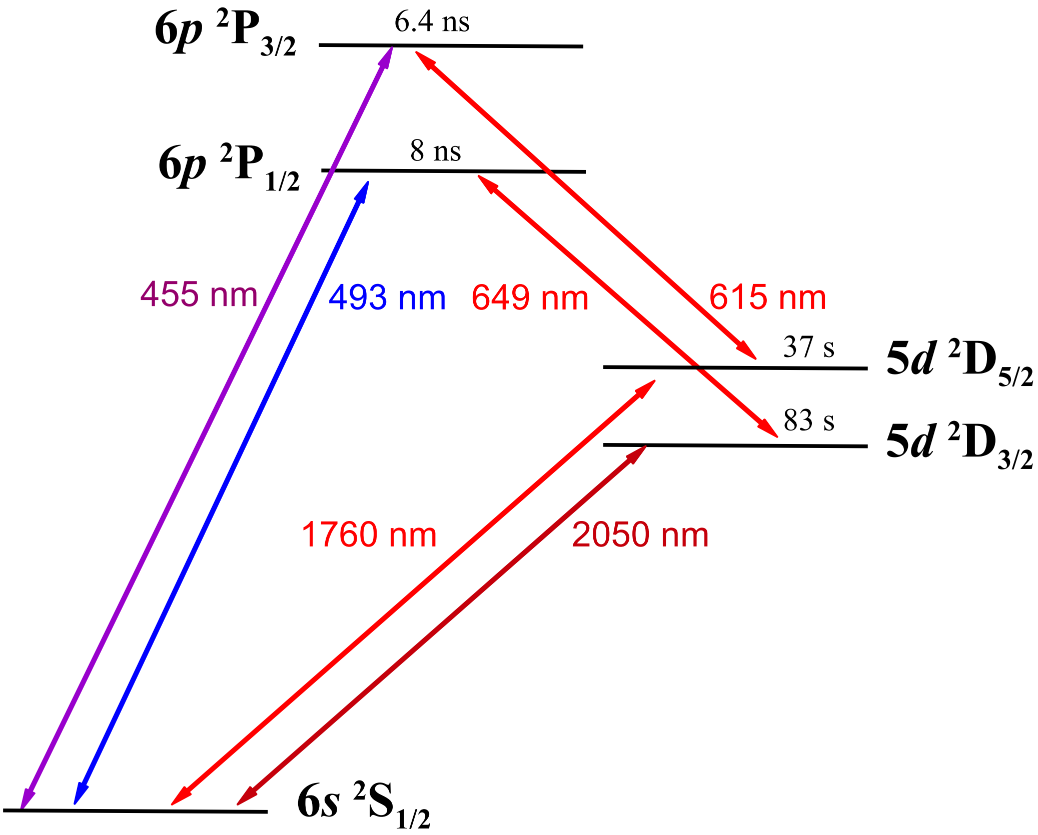

Fig. 3.2: Level diagram of Ba$^+$. Wavelengths and lifetimes are taken from [32, 44–46, 52, 87]

pool of experimental data is readily available in the literature. This enables us to understand the theoretical and experimental aspects on the trapping and cooling of Ra$^+$.

3.2 Ra$^+$: An Ideal Candidate for APV Experiment

A novel experimental method to measure atomic parity violation in a single trapped ion was proposed by E.N. Fortson [31]. Crucial steps have been taken and certain proof-of-principles have been demonstrated towards a single ion parity violation experiment using a single ^{138}Ba ion [44, 52]. This concept can be extended to Ra$^+$.

A high precision APV experiment is not self sufficient for a precise extraction of weak nuclear charge. The interpretation of experimental data requires a precise atomic theory. The existing *ab initio* methods in atomic theory to calculate atomic wave functions require experimental input to assess the accuracy of these methods. A heavy atomic system with a single valence electron is preferred for which the atomic wave function is comparatively easier to calculate and the APV signal would be bigger because of the Z^3 law [43]. The heaviest alkali systems like cesium atom (Z=55) and francium atom (Z=87) or the heaviest earth-alkali systems like Ba^+(Z=56) and Ra^+(Z=88) meet these requirements. Recently Yb^+ (Z=70) has been chosen as a potential candidate for a similar experiment [88]. But Ra^+ is the heaviest among others and hence it is expected to have comparatively larger parity violation. The relevant parity violating $7s\ ^2S_{1/2}$ - $6d\ ^2D_{3/2}$ amplitude is expected to be about a factor of 20 and 50 larger in Ra^+ than that in Ba^+ and Cs respectively [26, 65, 88], resulting in less stringent requirements for the theory while the statistical sensitivity would be larger. About 1 hour of data collection can lead to a statistical resolution of 1 Hz and about 10 days of data collection can lead to a 5 fold improvement of over the cesium result. Moreover, all the relevant transitions which are useful for probing parity violation in Ra^+ are in the visible or near infrared regime and hence they are accessible by commercial semiconductor diode lasers with narrow linewidth, which is certainly advantageous compared to Ba^+ (*cf.* Figs. 3.1 and 3.2). Being a heavy element, Ra^+ can be confined to a comparatively smaller trapping volume than Ba^+, since the Lamb-Dicke parameter is inversely proportional to the square root of mass of the ion. This will lead to the reduction of systematic uncertainties due to stray electric fields. Also the relative statistical uncertainty for Ra^+ is expected to be smaller compared to Ba^+. Thus, Ra^+ seems to be the superior candidate for a competitive parity violation experiment.

3.3 Signature of Parity Violation in Ra^+

A determination of the weak charge requires a robust and strong experimental signature. Here we discuss how atomic parity violation manifests itself in Ra^+. The exchange of Z^0 bosons between the electron and the quarks of an ion results in a mixing of the opposite parity states. The magnitude of mixing is maximum for S and P states.

In case of Ra^+, the $7s\ ^2S_{1/2}$ state gets a tiny admixture from the $np\ ^2P_{1/2}$ states

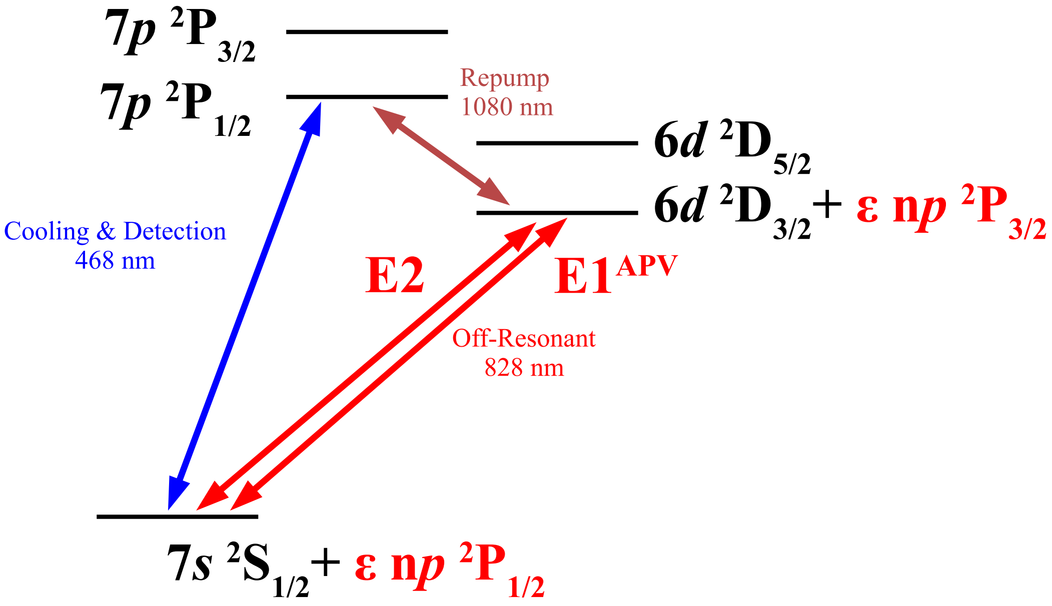

Fig. 3.3: Level diagram of Ra$^+$ with emphasis given to the admixture of P states with the low lying S and D states.

and no longer remains in a state of definite parity,

$$| 7s\ {}^2\tilde{S}_{1/2}\rangle = | 7s\ {}^2S_{1/2}\rangle + \varepsilon \mid np\ {}^2P_{1/2}\rangle \tag{3.1}$$

$$= | 7s\ {}^2S_{1/2}\rangle + \sum_n \mid np\ {}^2P_{1/2}\rangle \frac{\langle np\ {}^2P_{1/2} \mid H_W \mid 7s\ {}^2S_{1/2}\rangle}{E_{7s\ {}^2S_{1/2}} - E_{np\ {}^2P_{1/2}}}, \tag{3.2}$$

and the $6d\ {}^2D_{3/2}$ state also gets a tiny admixture from the $np\ {}^2P_{3/2}$ states,

$$| 6d\ {}^2\tilde{D}_{3/2}\rangle = | 6d\ {}^2D_{3/2}\rangle + \varepsilon \mid np\ {}^2P_{3/2}\rangle \tag{3.3}$$

$$= | 6d\ {}^2D_{3/2}\rangle + \sum_n \mid np\ {}^2P_{3/2}\rangle \frac{\langle np\ {}^2P_{3/2} \mid H_W \mid 6d\ {}^2D_{3/2}\rangle}{E_{6d\ {}^2D_{3/2}} - E_{np\ {}^2P_{3/2}}}, \tag{3.4}$$

where the Weak Hamiltonian H$_W$ is given by,

$$H_W = Q_W \times \frac{G_F}{\sqrt{8}} \gamma_5 \rho_n(r). \tag{3.5}$$

An electric quadrupole transition (E2) between the $7s\ {}^2S_{1/2}$ and the $6d\ {}^2D_{3/2}$ states is allowed by the parity selection rule. But the admixture from P states makes a small dipole transition (E1) possible between these energy eigenstates which is otherwise forbidden by the parity selection rule. The strength of the parity violating E1 amplitude is given by,

$$E1^{APV} = \langle 7s\ ^2\tilde{S}_{1/2} \mid D \mid 6d\ ^2\tilde{D}_{3/2} \rangle \tag{3.6}$$

$$= \sum_n \frac{\langle 7s\ ^2S_{1/2} \mid H_W \mid np\ ^2P_{1/2} \rangle \langle np\ ^2P_{1/2} \mid D \mid 6d\ ^2D_{3/2} \rangle}{E_{7s\ ^2S_{1/2}} - E_{np\ ^2P_{1/2}}} \tag{3.7}$$

$$+ \sum_n \frac{\langle 7s\ ^2S_{1/2} \mid D \mid np\ ^2P_{3/2} \rangle \langle np\ ^2P_{3/2} \mid H_W \mid 6d\ ^2D_{3/2} \rangle}{E_{6d\ ^2D_{3/2}} - E_{np\ ^2P_{3/2}}}. \tag{3.8}$$

Substitution of the weak Hamiltonian from Eq. 3.5 gives,

$$E1^{APV} = Q_W \times \frac{G_F}{\sqrt{8}} \sum_n \frac{\langle 7s\ ^2S_{1/2} \mid \gamma_5 \rho_n(r) \mid np\ ^2P_{1/2} \rangle \langle np\ ^2P_{1/2} \mid D \mid 6d\ ^2D_{3/2} \rangle}{E_{7s\ ^2S_{1/2}} - E_{np\ ^2P_{1/2}}} \tag{3.9}$$

$$+ Q_W \times \frac{G_F}{\sqrt{8}} \sum_n \frac{\langle 7s\ ^2S_{1/2} \mid D \mid np\ ^2P_{3/2} \rangle \langle np\ ^2P_{3/2} \mid \gamma_5 \rho_n(r) \mid 6d\ ^2D_{3/2} \rangle}{E_{6d\ ^2D_{3/2}} - E_{np\ ^2P_{3/2}}} \tag{3.10}$$

$$= Q_W \times k. \tag{3.11}$$

While $E1^{APV}$ can be experimentally measured, k arises from theoretical calculations using atomic theory. A detailed treatment on the calculation can be found in [89]. Since $E1^{APV}$ is extremely small, it must be measured using an indirect approach. The interference between the parity conserving E2 amplitude and the parity violating E1 amplitude leads to a measurable signal which can be observed as a small shift of the two ground state Zeeman sub-levels. This shift is a vector like AC Stark shift or differential light shift. From the differential light shift the parity violating E1 amplitude can be distinguished from the electromagnetic contribution, and the weak charge Q_W for the ion can be inferred.

In conlusion, Ra$^+$ is a sensitive system for probing parity violation. The sensitivity to parity violating weak interaction effects in this system is 50 times larger than that in cesium where the best such experiment was performed till date. Ra$^+$ is preferred over all other possible candidates based on the theoretical and experimental requirements for extracting the weak charge from a parity violation experiment. Spectroscopic information on hyperfine structures, isotope shifts and lifetimes in this system can yield the E1 and E2 matrix elements which are necessary for a parity violation measurement. Such information is scarce in literature. Hence an extensive study of this system through laser spectroscopy is indispensable.

Chapter 4

Experimental Methods and Tools

The development of a new type of experiment requires the building of state-of-the-art methods and tools which exploits the progress in many different fields of experimental physics. Here we present the development of the setup to produce, trap, and spectroscopically study Ra^+, guiding the path towards atomic parity violation experiments on a single trapped ion. The principle of operation and the underlying physics are discussed for each experimental tool that was developed or shared with other TRIμP experiments [16, 17].

4.1 Radium Isotope Production

Radium is radioactive in nature and most of the radium isotopes have a lifetime shorter than a couple of weeks. Short-lived radium isotopes with different nuclear spins are required to systematically investigate important physical properties such as isotopes shifts, hyperfine structure intervals and lifetimes. In this section we discuss the principle, the required experimental tools and the results of radium production.

The radium isotopes are produced in nuclear reactions at typical center of mass collision energies of 7-9 MeV/u. The high energetic reaction products are guided and selected in a magnetic separator. At the end of the separator the high energetic isotopes are converted into a low energy ion beam and are transported electrostatically to the experiments. This section provides the details of this part of the setup.

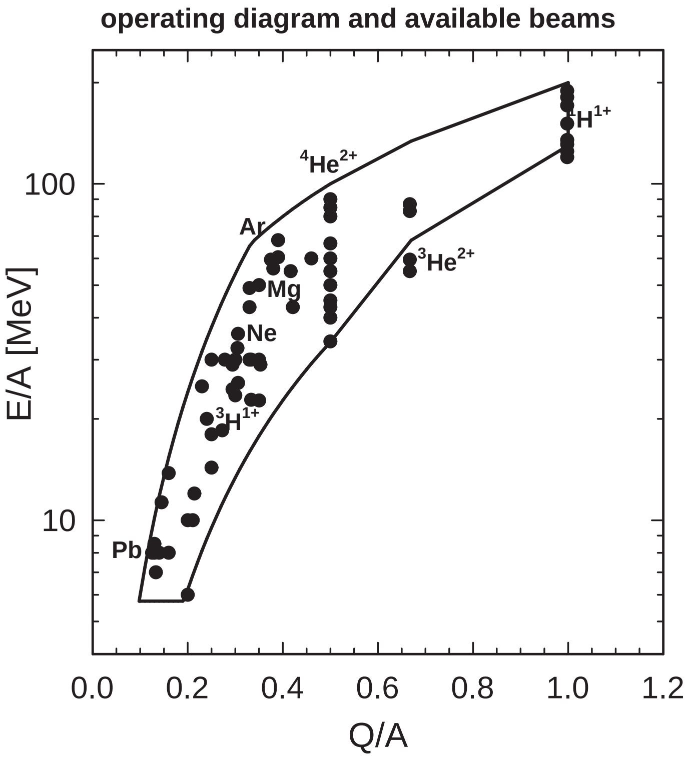

Fig. 4.1: Operating diagram of AGOR cyclotron [90]. It shows the range of beam energies as a function of charge-to-mass ratio of the beam particles.

4.1.1 The AGOR Cyclotron and Ra Production Target Station

The superconducting cyclotron AGOR (Accelerator Groningen ORsay) which was commissioned in 1996 [90] provides primary light and heavy ion beams to produce radioactive particles for the TRIμP research program. The acceptance range of charge-to-mass ratios for the cyclotron is shown in the operating diagram (Fig. 4.1).

An Electron Cyclotron Resonance (ECR) source provides initial ions from gaseous and metallic material. For the heavy ions, the charge-to-mass ratio determines the maximum achievable energy and it can accelerate protons up to 190 MeV/u. Presently the AGOR cyclotron delivers 1 kW of beam power for ions of interest for the TRIμP research program.

The radium isotopes are produced via fusion-evaporation reaction in inverse kinematics mode [91]. The lead and carbon nuclei are fused to create a compound nucleus which eventually evaporates some neutrons (n) to yield a residual radium nucleus. The nuclear reaction underlying the production mechanism is written as

$$^{206}Pb +^{12}C \rightarrow^{(218-X)} Ra + Xn. \tag{4.1}$$

This technique is called inverse kinematics because the high energetic projectile (Pb) is heavier than the target (C) and hence the residual nucleus has approximately the primary beam velocity and direction matching the acceptance of the TRIμP double magnetic separator.

The optimum production cross section of radium isotopes in the mass region A $\leq$ 215 is yielded with $^{206/204}$Pb beam of 8-10.3 MeV/u from the AGOR cyclotron. The high energy lead beam is bombarded on a diamond-like-carbon (DLC) target of 4 mg/cm^2 thickness, obtained from TRIUMF (Canada) or on a pyrolytic graphite target, obtained from MINTEQ International Inc (USA). The choice of the energy of primary beam depends on the cross section of $^{206/204}$Pb beam and ^{12}C target for optimum production of the radium isotope of interest. The calculated cross sections from the PACE code [92] for the nuclear reaction of $^{206/204}$Pb and ^{12}C as a function of primary beam energy are shown in Fig. 4.2 and 4.3. For our experiments, the optimal charge state of the ^{206}Pb beam for the most stable operation and efficient production is 27+. For ^{204}Pb beam the optimal charge state is 28+.

The primary beam from the AGOR cyclotron consists of about 3 × 10^{10} particles/s at about 100 W beam power. At any given energy (Fig. 4.2 and 4.3) this flux of particles is sufficient for the optimum production yield. The target shows deterioration after about 200 hours of use at such beam intensity. Higher beam intensities, when used for higher production yields, even results in the destruction of the target. To enhance the life of the production target, a rotating wheel was built on which the carbon foils are mounted. The target wheel is rotated at a maximum frequency of 15 Hz. A primary beam intensity of about 2 × 10^{11} particles/s has been used for more than 1000 hours with this rotating target. A picture of the target wheel is shown in Fig. 4.4.

4.1.2 Double Magnetic Separator

The radium isotopes are separated from the primary lead beam and other reaction products, mostly from fission, in the TRIμP double magnetic separator [19,93,94]. It consists of two dipole sections. Each section has magnetic quadrupoles (Q) and magnetic dipoles (D) in the configuration QQDDQQ. A schematic layout of the separator is shown in Fig. 4.5.

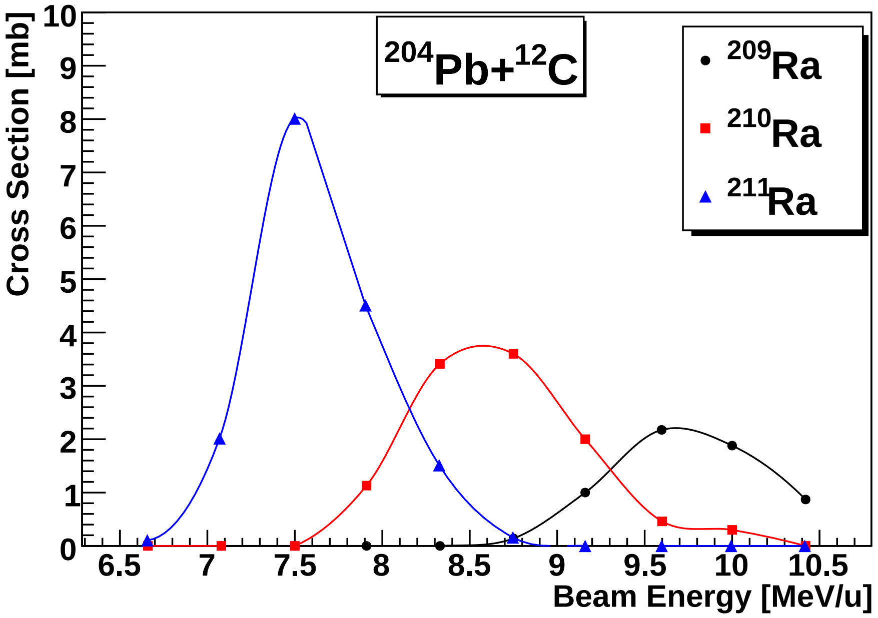

Fig. 4.2: Calculated cross section for ^{204}Pb beam and ^{12}C target. For the production of a specific isotope, energy of primary beam is chosen at which the yield would be maximum. The solid line in each case represents a trend line only and not a fit.

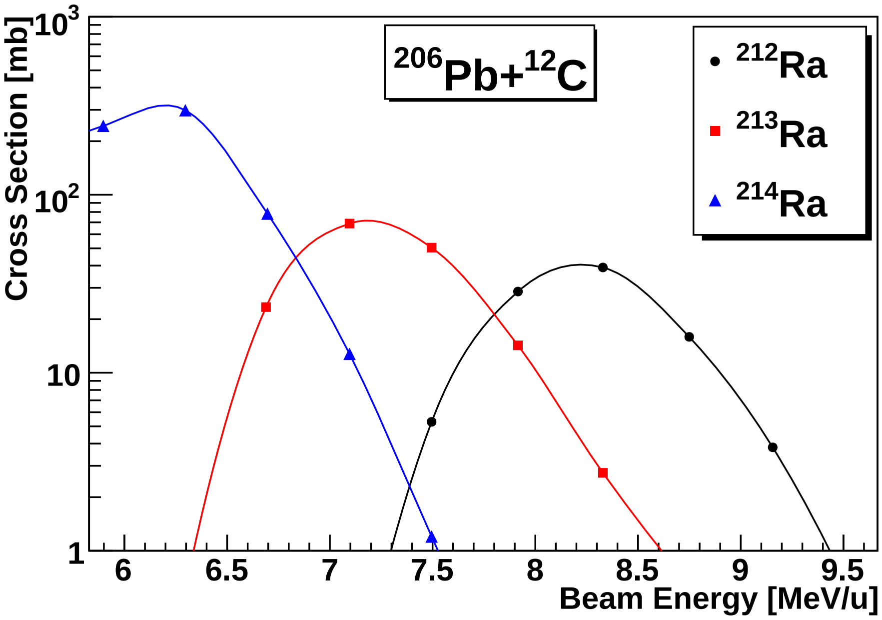

Fig. 4.3: Calculated cross section for ^{206}Pb beam and ^{12}C target. For the production of a specific isotope, energy of primary beam is chosen at which the yield would be maximum. The solid line in each case represents a trend line only and not a fit.

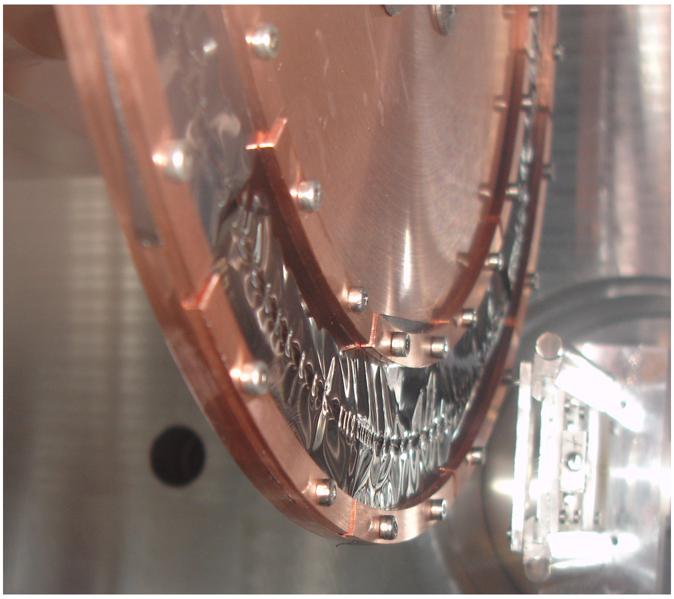

Fig. 4.4: Pyrolytic graphite target mounted on a rotating wheel. A trace of the primary beam can be seen on the target. It arises from local heating. The bottom right hand side shows a target ladder with auxiliary targets.

The magnetic quadrupoles focus the beam and the magnetic dipoles provide bending of the beam. The first section creates a dispersion of particles with different momentum-to-charge ratio according to their magnetic rigidity which is defined as

$$B\rho = \frac{P}{q} \simeq v\frac{A}{Z}. \tag{4.2}$$

This allows the selection of particles with different magnetic rigidities at the Intermediate Focal Plane (IFP) by a slit system which stop particles outside of the desired rigidities. The second section is used to further separateand refocus the secondary beam at the Final Focal Plane (FFP).

The radium isotopes are not fully stripped of their electrons after they leave the target. The average charge state is 58+ with a typical width of 8 charge state [19]. Thus the ions do not have the same rigidity and we can only select the most intense charge states. The magnet settings of the separator for optimum production yield are calculated using the LISE++ code [95].

Production of radium isotopes is confirmed at the FFP of the separator by using a 80 μm thick aluminum catcher foil, mounted in front of a silicon detector. The detector and the catcher foil are kept at an angle of 45° which stop the primary beam and allow to detect the α particles from the decay of radium isotopes.

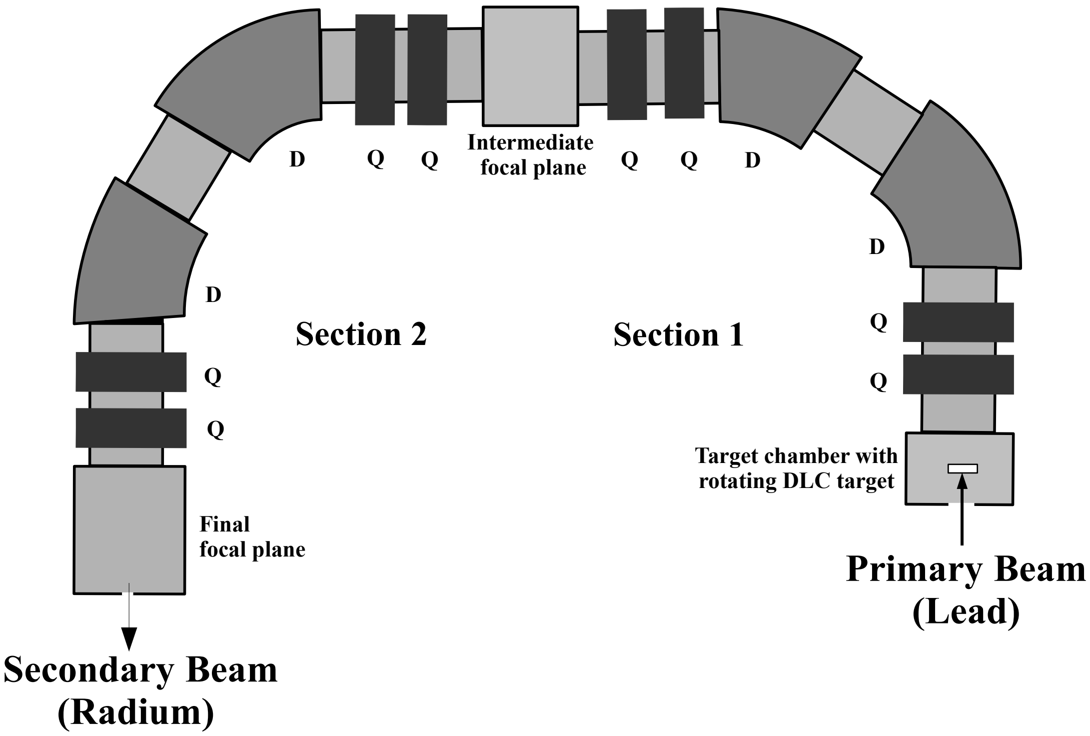

Fig. 4.5: Schematic diagram of the separator (not to scale) [91]. Q and D are abbreviations for quadrupole and dipole respectively.

4.1.3 Thermal Ionizer

The energy of the secondary beam is too high (a few MeV/u) for our experiments and they are decelerated to thermal velocity energies by stopping and extraction from material. The basic principle of operation of the thermal ionizer can be explained in five consecutive steps: stopping, diffusion, effusion, ionization, and extraction [19, 96]. The TRIμP thermal ionizer consists of a stack of 0.75 μm thick tungsten foils placed in a tungsten cavity. The schematic diagram of the TRIμP thermal ionizer is shown in Fig. 4.6. The secondary particles at the exit of separator are completely stopped by the tungsten foils inside a tungsten cavity. The maximal thickness of the foils is chosen to stop the full energy distribution of secondary particles at the exit of separator. For the experiments reported here, a stack of 3×0.75 μm foils has been used. The particles move to the surface of the foils by diffusion. Since the diffusion time to the surface depends on (thickness)^2, thin foils are needed. The thickness is as small as the rolling manufacturing process allows. The diffusion process is enhanced by heating the foils of the cavity to a very high temperature, about 2500 K. The cavity is heated by electron bombardment from surrounding tungsten filaments.

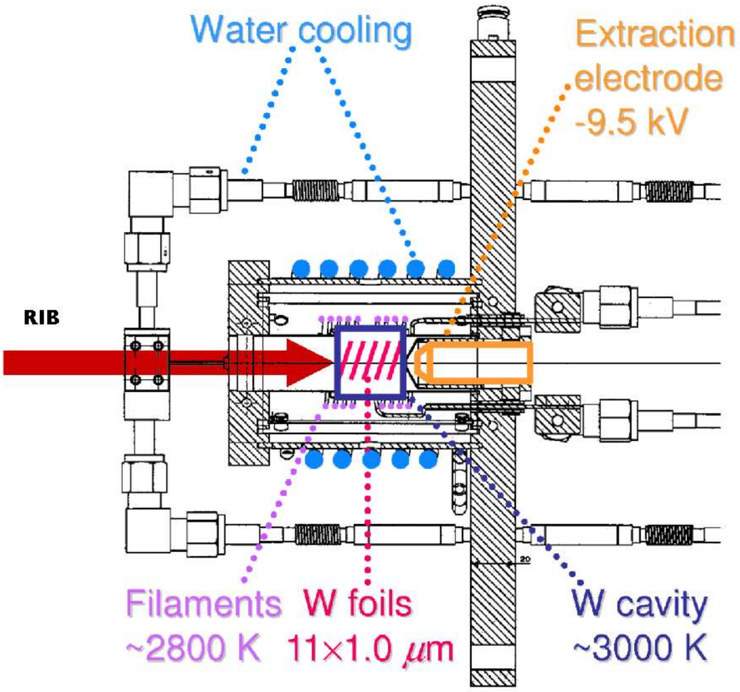

Fig. 4.6: Schematic diagram of the thermal ionizer (not to scale). It thermalizes the radioactive ion beams (RIB) for TRIμP experiments. Adapted from [19].

At the surface of the foils the particles escape by effusion. They are ionized by multiple collisions with the stopping foils and with the cavity walls. During this process the charge state of the particles changes multiple times, i.e., a fraction of the particles is neutral. The charged particles are dragged out of the tungsten cavity by electrostatic extraction, using an electric field gradient formed by a DC potential on the extraction electrode, as shown in Fig. 4.7.

The extracted particles are singly charged radium ions. Neutral radium isotopes inside the TI remain unextracted, but will diffuse out at a relatively lower rate. Charge states higher than +1 are completely negligible, because of the difference in the work function of tungsten and the necessary ionization energy to create higher charge states. Typical extraction efficiencies are about 8% [91] for radium and about 50% for sodium [19]. An extensive treatment of the principle, design, characterization of thermal ionizer can be found in [19].

An alternative approach was followed by other groups. They stop the reaction products in noble gases, typically helium. A fraction of the isotopes remain in the singly charged state and they can be extracted from the dense gas environment by electric fields [97–99]. A drawback is the large ionization of the stopping gas

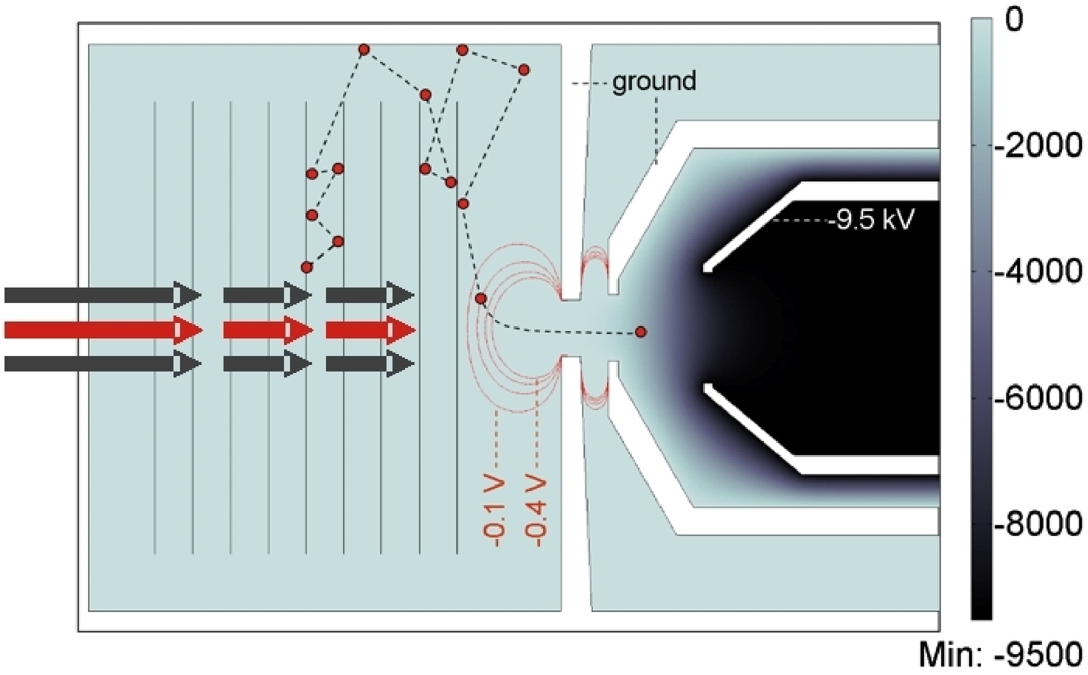

Fig. 4.7: Calculation of electric potentials inside the TI cavity created by setting the TI extraction electrode to -9.5 kV. Equipotential lines are shown for -0.1, -0.2, -0.3, and -0.4 V. A schematic trajectory of an ion is shown in the plot. Adapted from [19].

at high incoming beam intensities which leads to a decrease in efficiency in the range of operation for the TRIμP facility.

The foils of the thermal ionizer contain traces of elements, such as cesium, barium, sodium etc. Such alkali and alkaline-earth ions are an unavoidable part of the output of thermal ionizer. This feature of the thermal ionizer is actually advantageous for us. As discussed in chapter 3, Ba^+ is a chemical homologue of Ra^+. We always carry out different diagnostic experiments with Ba^+, including but not limited to the alignment of beam line, optimization of the setting of ion optics, trapping, and spectroscopy. In that context, the thermal ionizer serves as an uninterrupted source of barium ions.

4.1.4 Wien Filter

Since the output of the thermal ionizer is not isotope selective, all other ions are considered as contaminants for experiments with a specific atomic ion. To eliminate these contaminants, a Wien filter is employed. A Wien filter selects charged particles according to the charge-to-mass ratio by orthogonal electric and magnetic fields. Singly charged particles extracted from the thermal ionizer are injected into the Wien filter system with their velocity (v) orthogonal to both the electric field (E) and the magnetic field (B). Hence the particles will experience a Lorentz force, $F = e(E + vB)$. Since there are particles of different isotopes with different velocity classes, isotope selection is made by choosing a specific velocity class which experience a zero transverse force, for which $v = E/B$. Such particles will travel undeflected though the Wien filter. Particles experiencing a non-zero force will be deflected from their original trajectory and will be lost. Ions of mass m and kinetic energy T can pass the filter undeflected, for an electric field of

$$E = \sqrt{\frac{2T}{m}}B. \tag{4.3}$$

The Wien filter has a static magnetic field ($\sim$ 200 mT) and a tunable electric field. The length of the electrodes is 92 cm and the the length of the magnetic field is 80 cm. The resolution of Wien filter is better than two mass units in the region of ^{21}Na [19]. The electric field for sodium and radium are 570 V and 180 V respectively.

4.1.5 Results of Radium Production Experiments

^{212,213,214}Ra isotopes are produced using a primary ^{206}Pb beam at an energy of 8.5 MeV/u. For the production of ^{209,210,211}Ra isotope a ^{204}Pb beam at an energy of 10.3 MeV/u is employed. The radium isotopes are separated from the primary beam and other reaction products online in the double magnetic separator. At the final focal plane of the separator, the radium isotopes are stopped and re-ionized to Ra$^+$ in a thermal ionizer with a transmission efficiency of up to 8%. The singly charged radium isotopes are extracted from the thermal ionizer by applying a negative electrostatic potential of several kV on the extraction electrodes (Fig. 4.7).

The production of radium is quantitatively characterized measuring the radioactive decay. This is achieved by stopping the extracted ion beam from the thermal ionizer on a 1.8 μm thick aluminum foil in front of a silicon detector. α particles emitted from the stopped radium isotopes and their daughter nuclei are observed. Isotopes are identified by the characteristic energy of the α-particles. The characteristic energy spectrum of the α particles is shown in Fig. 4.8. The silicon detector is calibrated using an α source which consists of three different

α emitters with a well known energy (^{239}Pu with E_α=5.244 MeV, ^{241}Am with E_α=5.637 MeV, ^{244}Cm with E_α=5.901 MeV) [100].

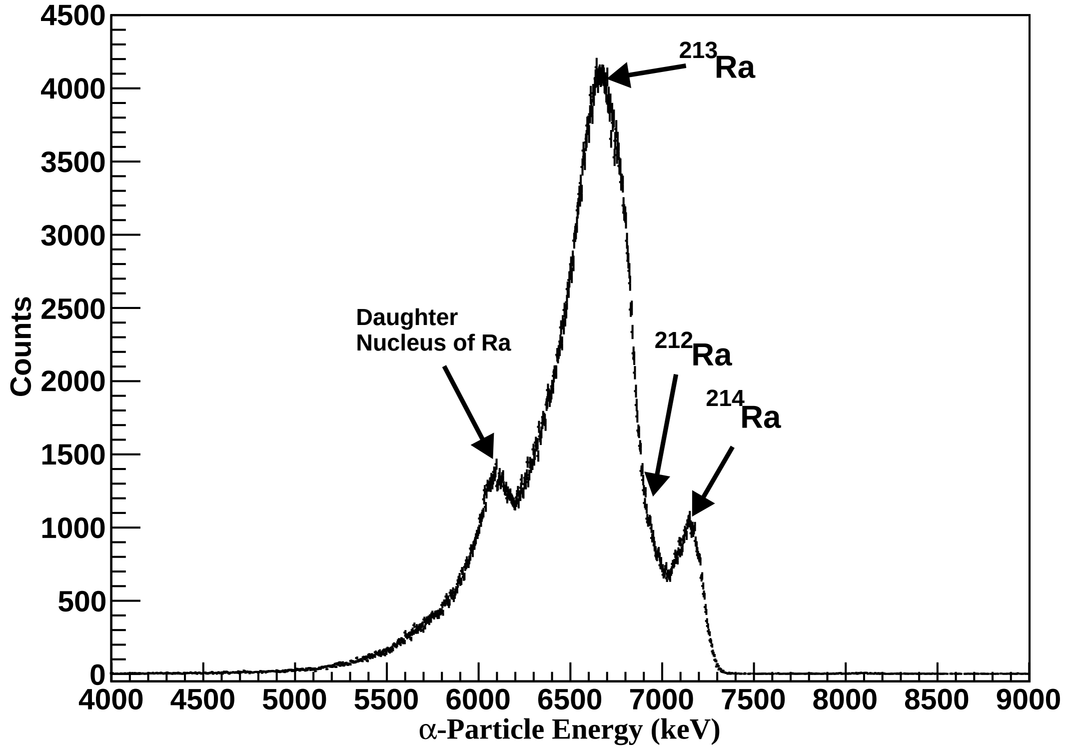

Fig. 4.8: Characteristic α-particle energy spectrum of radium observed after the TI. The ions are deposited on a 1.8μm aluminum foil in front of a calibrated silicon detector [91].

The production rate is estimated and the half lives of the produced isotopes are extracted by studying the output of thermal ionizer in two different modes [91]. In one mode the primary beam from the cyclotron is continuously on, while the extraction of ion beam from the thermal ionizer is cycled with 500 s extraction on and 500 s extraction off. Hence the build-up and decay of the activity on the aluminum foil depend only on the half-lives of the extracted isotopes. In the other mode, extraction of ions form the thermal ionizer is continuously on, while the primary beam from the cyclotron is chopped in a cycle with 500 s beam on and 500 s beam off. Hence the half lives of the produced isotopes at the site of measurement are influenced by the time the particles spend inside the thermal ionizer. Therefore, in case of the beam on/off mode the output is expected to be delayed as compared to the extraction on/off mode. The chopping time for the primary beam and the cycling time for the extraction of thermal ionizer

Table 4.1: Half lives and production rates for $^{212-214}$Ra [91].

Isotope	Half lives	Production rate
^{212}Ra	12.5(1.0) s	800 ions/s
^{213}Ra	162.0(1.7) s	2600 ions/s
^{214}Ra	2.42(14) s	1000 ions/s

Table 4.2: Half lives for $^{209-211}$Ra isotopes.

Isotope	Half lives
^{209}Ra	4.6(1.5) s
^{210}Ra	3.66(18) s
^{211}Ra	12.61(5) s

are chosen to be 500 s in order to exceed the half lives of the radium isotopes. The beam on/off and extraction on/off measurements are carried out at different temperatures of the thermal ionizer foils. At low temperatures the output of the thermal ionizer for beam on/off mode is found to be delayed compared to the extraction on/off mode. The results are shown in Fig. 4.9. The results show that high temperatures are needed to achieve a release time of the radium isotopes from the thermal ionizer which is shorter than the timescale given by the lifetime of the isotope.

The characteristic half lives of the radium isotopes and their production rate are extracted by fitting the activity curve obtained from the extraction on/off measurements by gating on the appropriate parts of the spectrum shown in Fig. 4.8 and correcting for computer deadtime. The extraction on/off measurements give a better reflection of half lives since the extraction on/off measurement is independent of the delay time in case of beam on/off measurements which is associated with the residence time inside the thermal ionizer [91, 101]. The extraction on/off measurements are shown in Fig. 4.10. The extracted half lives and the production rates are listed in Table 4.1.

The production of lighter radium isotopes ^{209,210,211}Ra has also been verified using the same technique as described for ^{212,213,214}Ra. A typical activity curve obtained by extraction on/off measurement is shown in Fig. 4.11. The half lives of the lighter isotopes and their long-lived daughters are listed in Table 4.2. The production yield of ^{209}Ra is about a factor of 10 less compared to the production yield of ^{213}Ra because of the cross section.

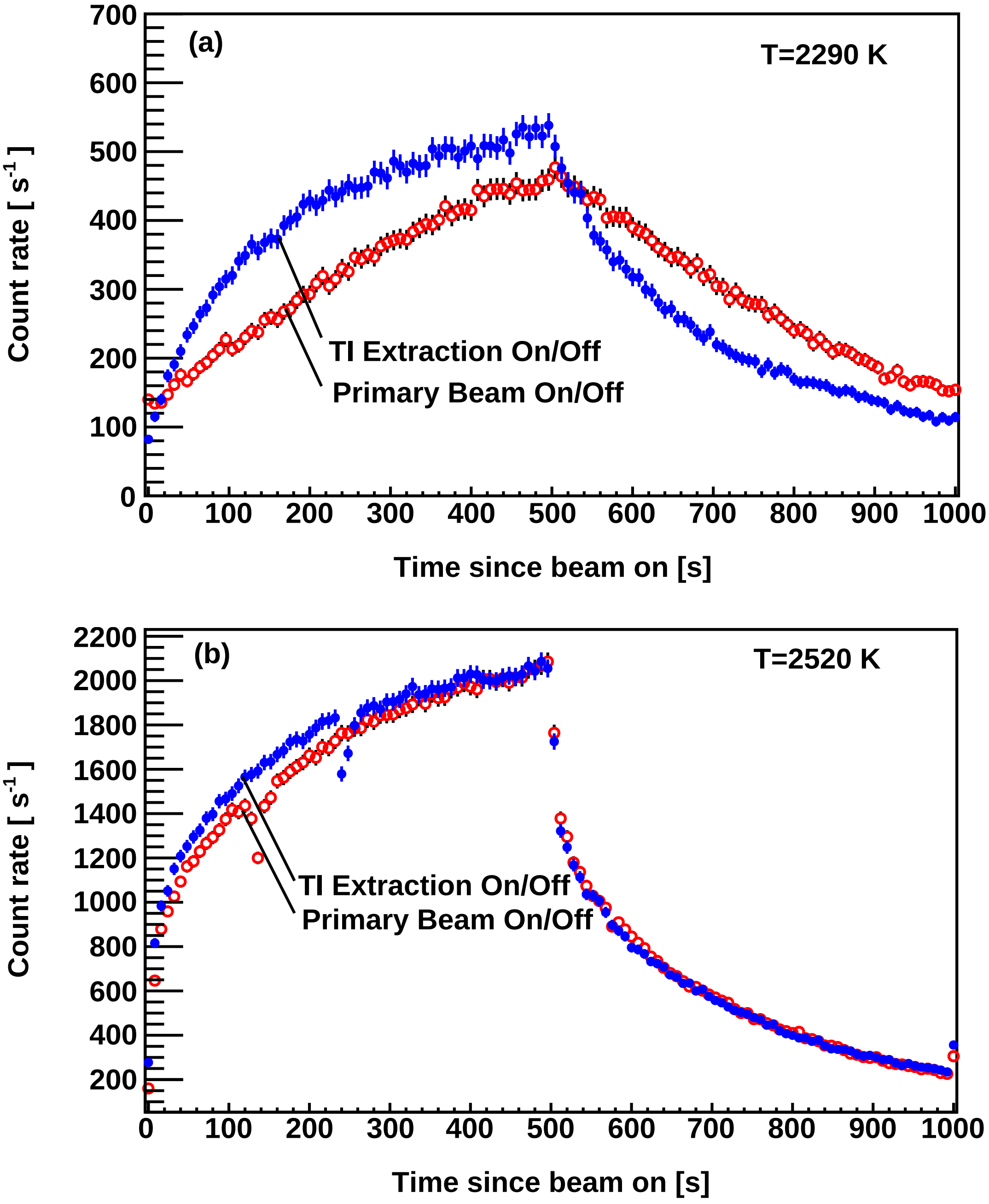

Fig. 4.9: Activity curves obtained by extraction on/off (blue markers) and primary beam on/off (red markers) measurements at (a) T = 2290 K and (b) T = 2520 K [91]. A delay time related to the residence time inside the thermal ionizer can be seen in (a).

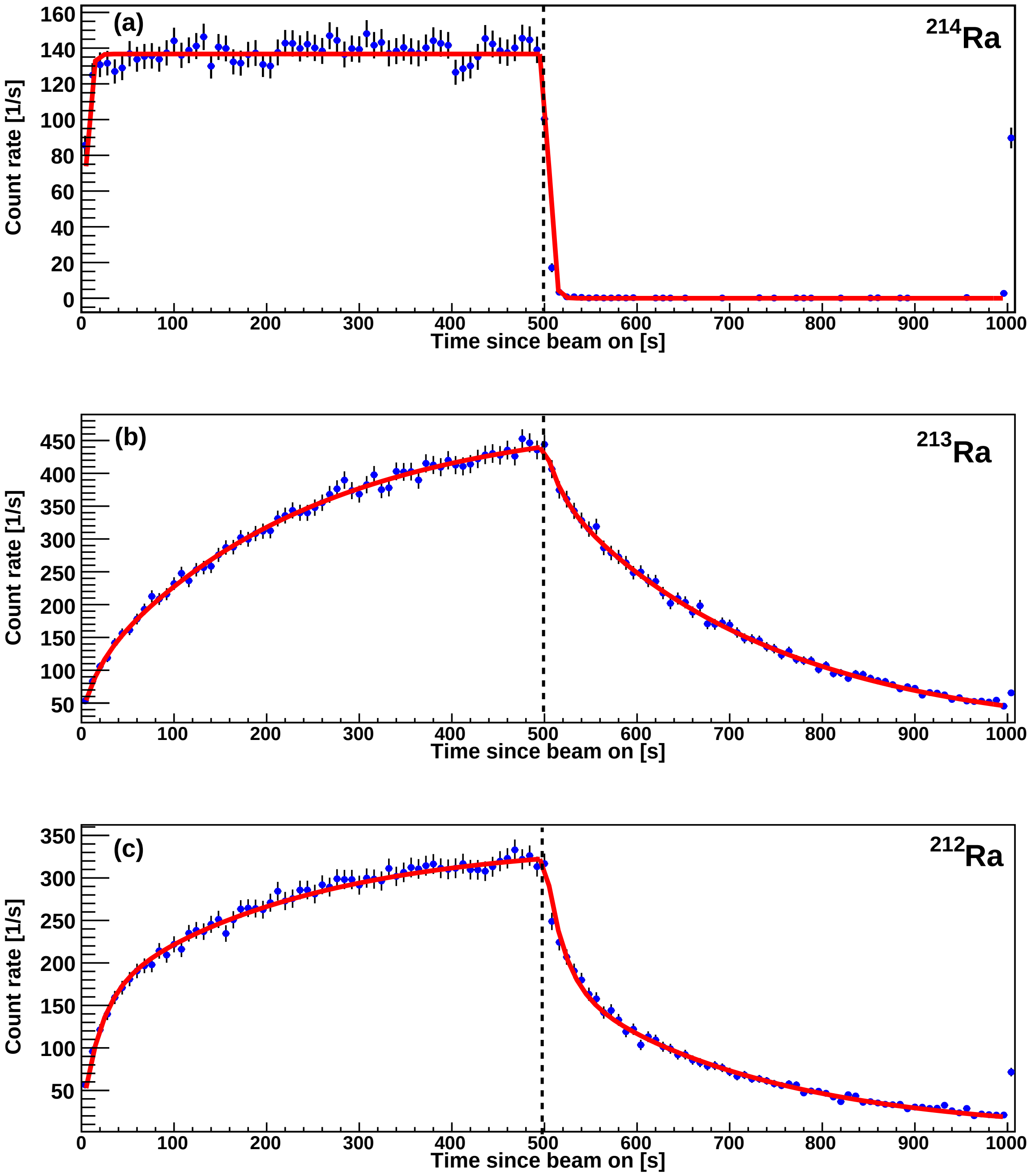

Fig. 4.10: Measured activity for (a) ^{214}Ra$^+$ (b) ^{213}Ra$^+$ (c) ^{212}Ra$^+$at T = 2430 K [91]. An exponential fit is applied to each data set. The fit results are shown by solid red line. The dashed line in each case indicates the time when the extraction from TI was switched off.

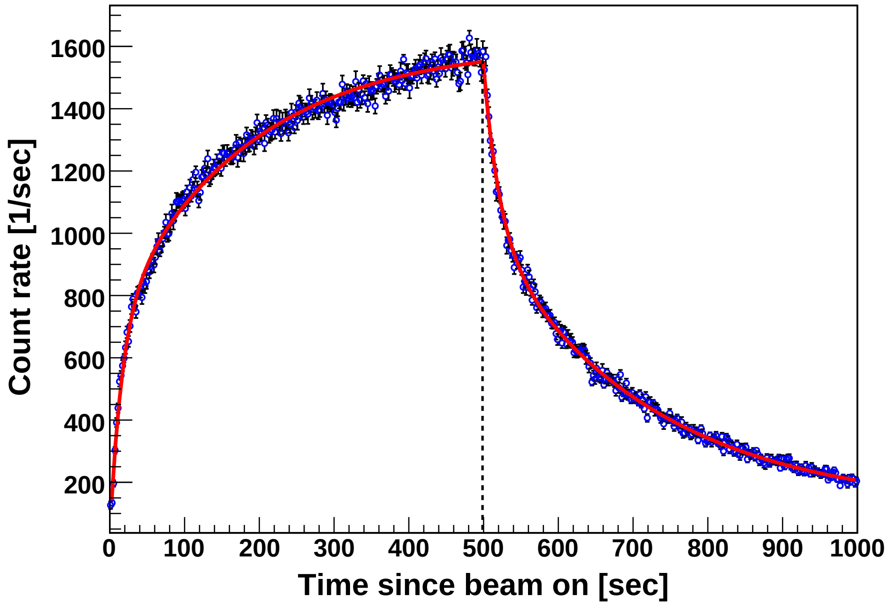

Fig. 4.11: Measured activity for a mixture of three radium isotopes $^{209-211}\mathrm{Ra}^{+}$. A fit of four exponential functions is applied to the data, one exponential function for each of the three radium isotopes of interest and one exponential function for the daughter isotope of ^{209}Ra. The fit result is shown by the solid line. However this fit is not unique and other daughters can be present. Using the optical signals discussed later an estimate of production rates can be made (Table 7.1). The dashed line indicates the time when the extraction from the TI was switched off.

4.2 Radium Ion Trapping and Spectroscopy

4.2.1 Trapping in a Radio Frequency Quadrupole

The segmented Radio Frequency Quadrupole (RFQ) is an extended version of a linear Paul trap [102]. In Fig. 4.12 the schematic diagram of the TRIμP RFQ system is shown, which was originally built to improve radioactive beam emittance by cooling the ions with buffer gas, guiding them in a radial quadrupole field and with the ability to store the ions and extract them in bunches [19]. It consists of two mechanically identical sections. Each section has an entrance electrode with an aperture, the four RF/DC electrodes with segmented structures, and an exit electrode with an aperture. The apertures are needed for differential pumping which provides a controlled difference in pressure between the two sections. The first section (cooler) provides transverse cooling of the ions. Cooling is achieved

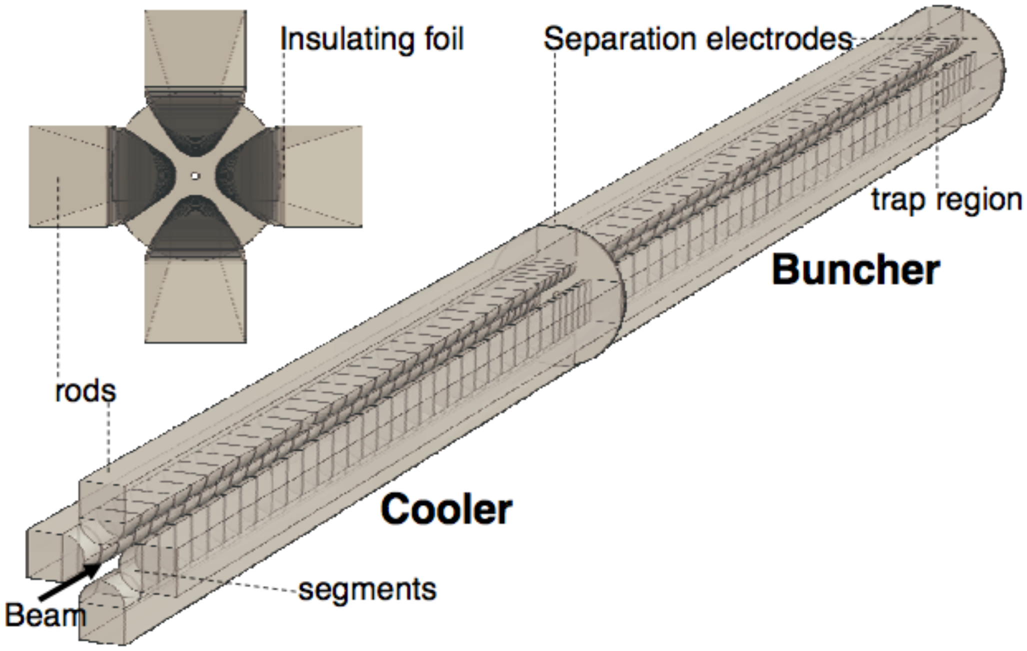

Fig. 4.12: Schematic diagram of the RFQ (not to scale) [19]. It has two identical sections. Each section has an entrance electrode with aperture, 4 electrodes each with 30 segments, and an exit electrode with aperture.

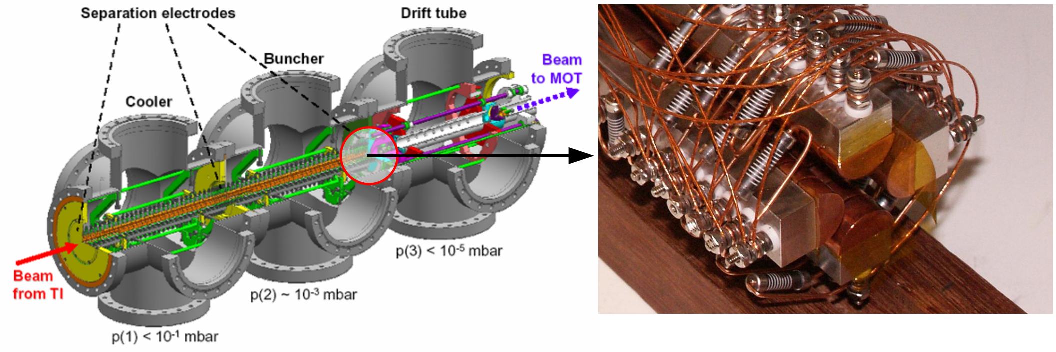

Fig. 4.13: Schematic diagram of the RFQ. The trapping region is optional and it has been enlarged here for better visibility. Ion trapping and laser spectroscopy is realized in this part. The last part is a drift tube which enables extraction of the trapped ions.

by interactions of the ions with a buffer gas at about 1-2 × 10^{-2} mbar pressure which is optimal for transverse cooling. A buffer gas with high ionization potential is chosen (e.g., He, Ne, or N_2) to prevent charge-exchange processes. With an RF voltage between opposite rods, DC voltage between the segmented electrodes, and a small potential difference between the two sections of RFQ, the ions are guided along the central axis up to the end of the second section (buncher). The buncher works with a buffer gas at about 1-2 × 10^{-3} mbar pressure or even lower. It can also be operated in trapping mode. The voltages of the last four electrodes are chosen such that a potential well is created to store the ions. The trapping region in the buncher section of RFQ is shown in Fig. 4.13. Discussion of the physics of ion trapping can be found in Appendix A.

The Ra^+ beam from the thermal ionizer is decelerated to 2.8 keV using an electrostatic deceleration lens. The decelerated ion beam is injected into a gas filled radio frequency quadrupole operated at a radio frequency of 500 kHz with an RF amplitude of 190 V applied between the neighboring rods from which the RF voltage is capacitively coupled to the opposite half-moon shaped electrodes. The half-moon shaped electrodes are 10 mm in length and have a tip distance of 5 mm. The ions are cooled in the cooler stage with nitrogen (N_2) or neon (Ne) as a buffer gas at a pressure of about 1-2 × 10^{-2} mbar. The buffer gas atoms (Ne) or molecules (N_2) dissipate the large energy of the ions from the thermal ionizer. The ions are guided to the buncher section which works at a lower gas pressure of about 5-9 × 10^{-4} mbar. The ions are trapped at the end of RFQ with an effective potential depth of 13 V and an axial potential depth of 10 V. This configuration of axial potentials is found to be optimal for most efficient trapping in a large trapping volume. The buffer gas enables to compress the trapped ion cloud and also enhances the storage time. About 10^4 ions can be stored in the trap. The storage time of the trapped ions is of the order of 100 s at a residual gas pressure of 10^{-8} mbar. In presence of buffer gas the level lifetimes are found to be influenced due to optical quenching and hyper(fine) structure mixing [103].

4.2.2 Spectroscopy of Trapped Radium in RFQ

We first demonstrate our ability to trap Ba^+ and perform spectroscopy in the RFQ which is indispensable for working towards Ra^+. Using the thermal ionizer as a barium ion source and operating the RFQ in trapping mode, Ba^+ ions are trapped as a cloud. Laser spectroscopy of trapped Ba^+ is performed with two lasers (Fig. 3.2). Frequency doubled light of wavelength 493 nm originating

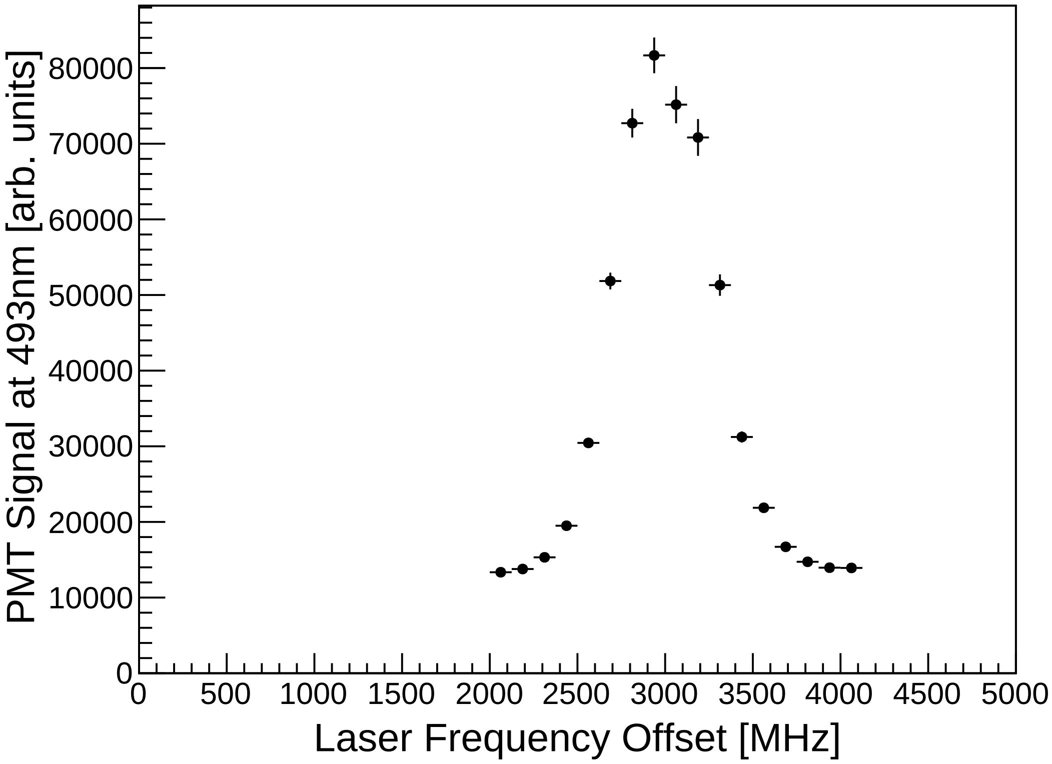

Fig. 4.14: $5d\ ^2D_{3/2}$ - $6p\ ^2P_{1/2}$ transition in Ba^+. Two lasers, one at 493 nm and the other at 650 nm, drive the pump and repump transitions, respectively.

from the second harmonic generation of light of wavelength 987 nm is used to pump the ground $6s\ ^2S_{1/2}$ state, thereby populating the excited $6p\ ^2P_{1/2}$ state. The frequency of this light is tuned to be on resonance to continuously pump the ground state. From the $6p\ ^2P_{1/2}$ state the ions decay to the metastable $5d\ ^2D_{3/2}$ state with a branching ratio of about 1 in 5. Light of wavelength 650 nm is employed to repump the ions from the metastable state. The frequency of this laser is scanned. A spectrum of the $5d\ ^2D_{3/2}$ - $6p\ ^2P_{1/2}$ transition in Ba^+ is shown in Fig. 4.14.

4.2.3 Trapping and Spectroscopy in a Linear Paul Trap

Trapping and spectroscopy of Ra^+ in the RFQ described in sections 4.2.1 and 4.2.2 enables us to search for relevant transitions and crucial spectroscopic information that is scarce in the literature. Moreover optical measurements of physical properties such as hyperfine structures, isotope shifts and lifetimes are performed on the trapped radium ions in the RFQ. It is worthwhile to mention here that the final goal of the experiment is to perform a precision measurement of atomic parity violation in a single trapped radium ion. This requires trapping of radium ions in linear Paul trap that is free of any background buffer gas. Since RFQ is not an appropriate system to achieve this goal we follow a different approach where the radium ion beam from the TI is injected into a pulsed drift tube (instead of RFQ) from which the beam is further transported to a linear Paul trap via a low energy beam line (LEBL) consisting of steering plates, Einzel lenses, an electrical mirror, and another drift tube. A schematic view of the LEBL is shown in Fig. 4.15. In the linear Paul trap at the end of LEBL, trapping of ions is investigated without any buffer gas.

Description of LEBL

The LEBL allows to connect the TI and the ion and atom traps via a pulsed drift tube. The drift tube, due to its pulsing capability, can replace the RFQ. The pulsed drift tube enables transportation of an accelerated ion beam of several keV. The drift tube is operated at a potential corresponding to the beam energy. It can be switched on and off by a fast high voltage switch (Behlke HTS-81-03-GSM Options DLC-ISO-HFS) which is equipped with water cooling and therefore allows to achieve a maximum toggle frequency of 100 kHz over about a week of operation. During the on period the ions can travel into the drift tube and during the off period the ions can travel out of the drift tube without experiencing the fringe field at the entrance and exit of the tube. The ions that are not in phase with the on/off time sequence of the drift tube are lost. In the optimal situation the on period of the drift tube allows to fill the tube completely. The duty cycle of the drift tube (D) is defined as the ratio of on period (t) to the full period of the pulse (τ) at the optimal situation

$$D = \frac{t}{\tau} \tag{4.4}$$

$$\tau = \frac{2l}{\sqrt{2T/M}}, \tag{4.5}$$

where l is the length of the drift tube, T is the kinetic energy of the accelerated ion, and M is the mass of the ion.

The LEBL in our experiment consists of two pulsed drift tubes, two pairs of bending plates, two Einzel lenses, an electrostatic mirror, and a linear Paul trap at the end of beam line. A schematic view of the low energy beam line is shown in

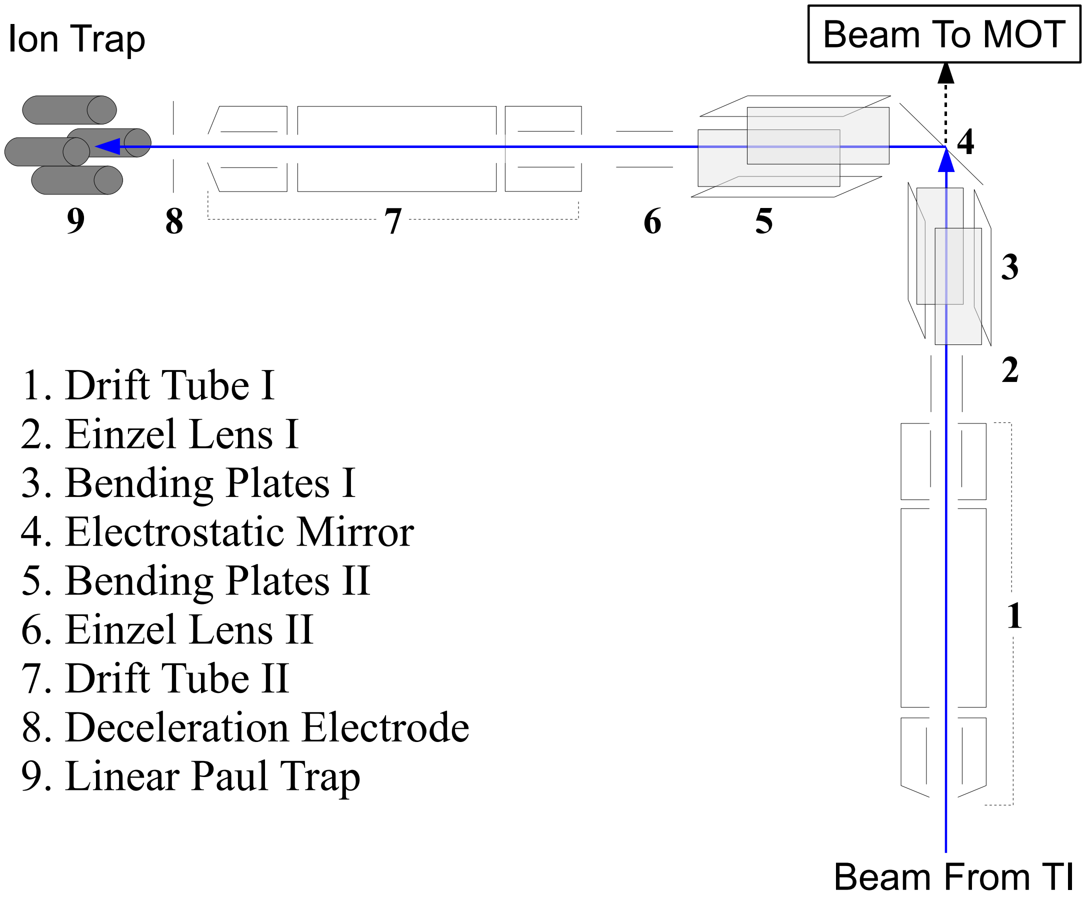

Fig. 4.15: Schematic view of low energy beam line (not to scale). Experimental parts numbered from 1 to 3 were developed in the past for magneto optical trapping of ^{21}Na. Experimental parts numbered from 4 to 9 have been developed for the trapping and spectroscopy of Ra$^+$.

Fig. 4.15. The first drift tube after the TI is pulsed between −2.8 kV and 0 V at a frequency of 22 kHz. For this tube a duty cycle of 45% is achieved for Ra$^+$ at 2.8 keV energy with the length of the drift tube l=100 cm and with $1/\tau$=22 kHz. The second drift tube before the ion trap is pulsed between +2.8 keV and -100 V at a frequency of 22 kHz. The loading and unloading timing sequence of this second drift tube is a critical parameter which is carefully adjusted using a synthesizer and a gate-delay generator module. The phase difference between the pulsing of the two drift tubes requires careful adjustment according to the time of flight of the ions from the first drift drift tube to the second drift tube. For the second drift tube the on period is 22.4 μs and the full period of the pulse is

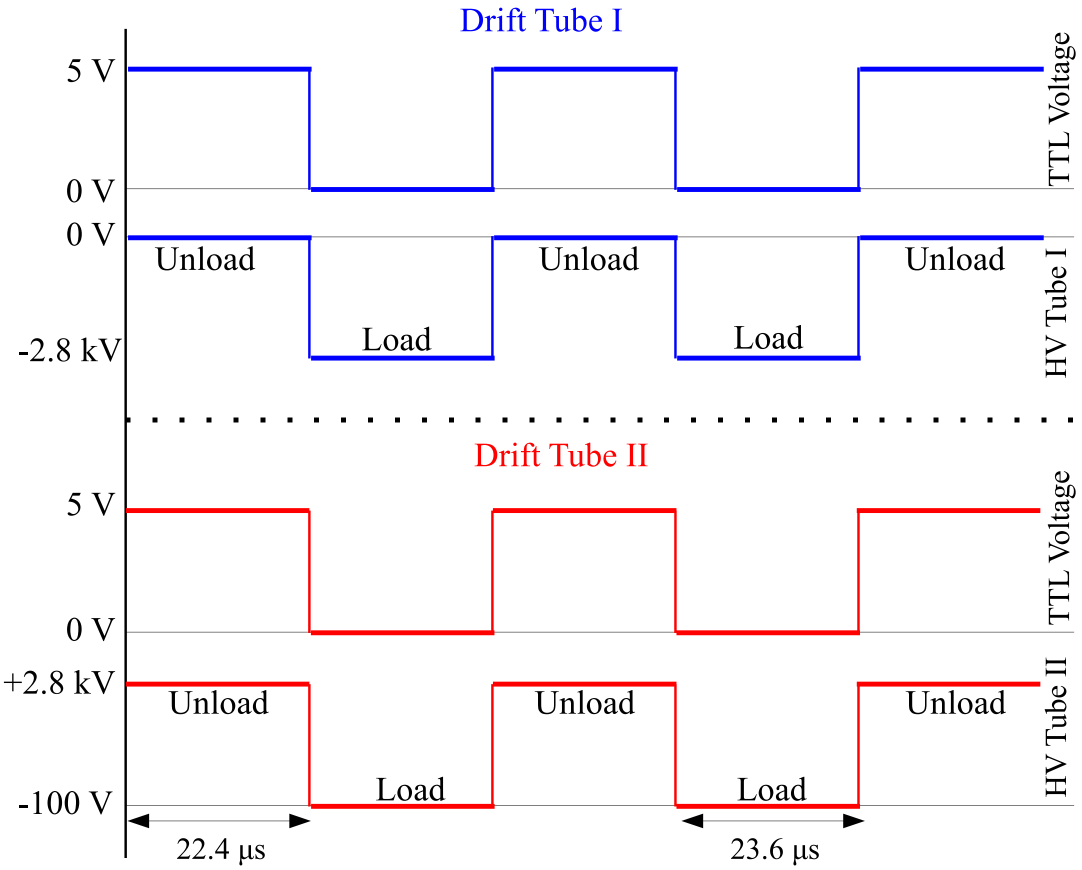

Fig. 4.16: Pulsing sequence of drift tubes. The phase between the timing of two drift tubes requires careful adjustment according to the time of flight of ions between the two tubes. The on and off period of the drift tube are 23.6 μs and 22.4 μs respectively.

46 μs. The timing sequence is shown in Fig. 4.16.

The bending plates enable vertical and horizontal steering of beams. The Einzel lenses enable focusing and defocusing the beam as necessary. An electrostatic mirror is mounted on an adjustable translational stage. It bends the beam trajectory by 90° for transporting them to the linear Paul trap. Without this mirror, the beam can be transported to a magneto optical trap (MOT) of ^{21}Na. At several positions of the beam line detectors like micro channel plates (MCP) and silicon detectors are mounted on movable translational stages. Such detectors enable beam diagnostics such as alignment, spot size of the ion beam, and transport efficiency. For example, a silicon detector before and after the electrostatic mirror determines the efficiency of the electrostatic mirror to be about

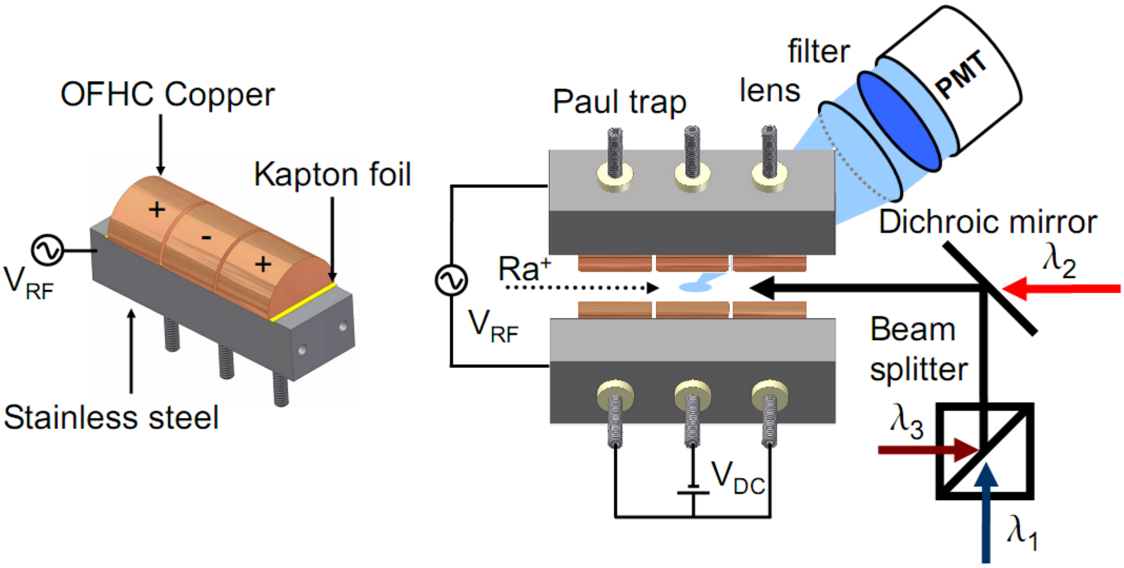

Fig. 4.17: Schematic diagram of linear Paul trap with an overview of the optical setup necessary for optical detection and spectroscopy. The electrodes with their segmented structure is shown. The RF voltage is applied to the stainless steel rod from which it is capacitively coupled to the half moon shaped copper electrodes. The wavelengths are λ_1= 468 nm, λ_2= 1079 nm, and λ_3= 708 nm.

50%. A linear Paul trap is placed at the end of the beam line.

A schematic drawing of the Paul trap is shown in Fig. 4.17. The geometry of the trap electrodes is similar to that in the RFQ. The trap consists of 4 diagonally opposite rods made of stainless steels. Each rod contains 3 segmented half moon shaped copper electrodes. DC voltages are directly applied to the copper electrodes. The radio frequency voltages are applied to the stainless steel rods. From these rods the RF voltage is capacitively coupled to the copper electrodes. A thin insulating material between the rods and the electrodes is necessary to prevent electrical breakthroughs as well as to provide higher capacitance. Kapton, a polyamide foil, is used as an insulating material. Polyamide materials are preferred for such purposes because of their stable electrical properties. Their dielectric strength stays in the order of a few kV/mm and their electrical properties are preserved at higher temperatures ($\sim$ 300° C). Hence this material is also suitable for vacuum baking.

The alignment of this newly commissioned low energy beam line is critical for trapping ions in the ion trap at the end of the beam line. This can be achieved

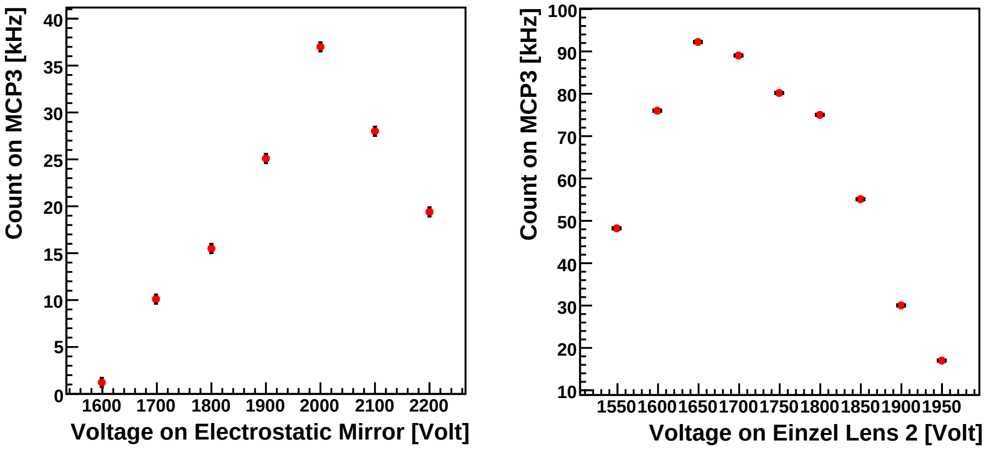

Fig. 4.18: The left figure shows a scan of the voltage applied to the electrostatic mirror. The right figure shows a scan of the voltage applied to the Einzel lens II. MCP 3 is located after the linear Paul trap (Fig. 4.15). For both the figures an error of ±5 V and ±0.5 kHz have been taken for the horizontal and vertical axes respectively.

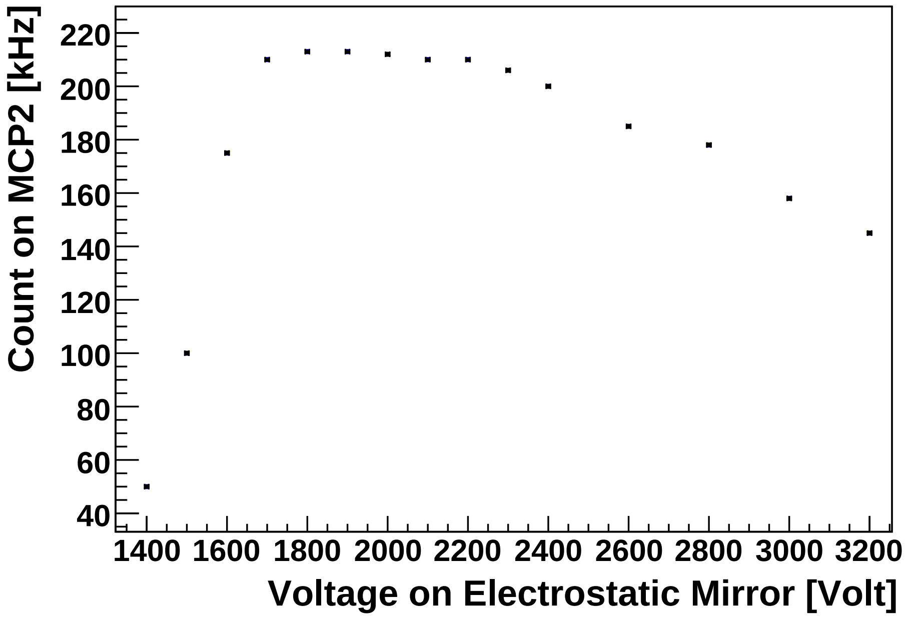

Fig. 4.19: A scan of the voltage applied to the electrostatic mirror. The maximum efficiency of 50% has been achieved by applying any voltage between 1700 volts and 2200 volts. MCP 2 is located between the Einzel lens II and drift tube II (Fig. 4.15).

by optimization of the signal from a micro channel plate (MCP) mounted after the trap and operated in counting mode. The voltages are applied using NIM HV modules and the MCP signal is processed with a discriminator. Some examples of the scans are shown in Figs. 4.18 and 4.19. The mirror is not sensitive between 1700 volts to 2200 volts when its performance is tested immediately after the ions are bent around the corner. This is shown in Fig. 4.19. But the sensitivity around 2000 V as shown in Fig. 4.18 is due to the fact that the ions travel through many lenses and apertures before the trap.

4.3 Lasers

Lasers at visible, near infrared and far infrared wavelengths are required to drive the atomic transitions in Ra^+ (Fig. 3.1). All the transitions can be accessed with cost effective semiconductor laser diodes. The diode lasers are available in commercially standardized packages of 5.6 mm and 9 mm diameter. Such diode laser systems are user friendly for spectroscopy experiments due to smaller size and operational simplicity [104, 105]. The laser systems, their frequency stabilization, their intensities and spot sizes, the calibration of their frequencies, and the optical layout for spectroscopy are described in this section. A list of all the laser systems necessary for our experiments with the relevant atomic transitions in Ba^+ and Ra^+ is given in Table 4.3.

4.3.1 Lasers for Ra^+

The lasers for Ra^+ are frequency stabilized in an external cavity diode laser (ECDL) configuration or Littrow configuration [104,105] by providing frequency selective optical feedback. Laser diodes can operate in a single longitudinal or transverse mode. They are extremely sensitive to feedback of light which is within its gain profile. This fact is exploited in ECDL where a grating provides frequency selective optical feedback. A schematic drawing of the mechanical set up of the Littrow configuration is shown in Fig. 4.20.

The external cavity consists of a diffraction grating that couples part of the light into the laser through the end orifice of the diode. The grating angle is set to reflect light for a particular wavelength in the direction of the incoming light. This is the concept of Littrow configuration. The diffraction angle for a grating in Littrow configuration satisfies the grating equation $2d\sin\theta = n\lambda$, where d is the groove spacing which is equal to (groove density)$^{-1}$, θ is the angle

Table 4.3: Laser systems for driving different optical transitions in Ba$^+$ and Ra$^+$. The corresponding atomic level schemes are shown in Fig. 3.1 and 3.2. Wavelength with an asterisk indicate that the laser system will be made operational in near future.

Atomic System	Wavelength (nm)	Transition	Diode Laser & Manufacturer	Power (mW)
Ra$^+$	λ_1=468	$7s\ ^2S_{1/2}$ - $7p\ ^2P_{1/2}$	NDHA210APAE1 Nichia	20
Ra$^+$	λ_2=1079	$6d\ ^2D_{3/2}$ - $7p\ ^2P_{1/2}$	LD-1080-0075-1 Toptica	40
Ra$^+$	λ_3=708	$6d\ ^2D_{3/2}$ - $7p\ ^2P_{3/2}$	HL7001MG Opnext	40
Ra$^+$	λ=802*	$6d\ ^2D_{5/2}$ - $7p\ ^2P_{3/2}$	QLD-810-100S QPhotonics	100
Ra$^+$	λ=828*	$7s\ ^2S_{1/2}$ - $6d\ ^2D_{3/2}$	ELD83NPT50 Roithner Laser Technik	60
Ra$^+$	λ=381*	$7s\ ^2S_{1/2}$ - $7p\ ^2P_{3/2}$	NDHU110APAE3 Nichia	20
Ra$^+$	λ=728*	$7s\ ^2S_{1/2}$ - $6d\ ^2D_{5/2}$	-	-
Ba$^+$	λ_1=493 Freq. Doubled	$6d\ ^2D_{3/2}$ - $7p\ ^2P_{3/2}$	L980P300J @ 987 nm Thorlabs	300
Ba$^+$	λ_2=649	$6d\ ^2D_{3/2}$ - $7p\ ^2P_{3/2}$	DL3147-060 Thorlabs	5

of incidence, n is the order of diffraction, and λ is the wavelength of the incident light. The only wavelengths that satisfy this grating equation are reflected back from the grating. The laser diode is forced to resonate at the wavelength that is fed back from the grating and hence it oscillates at a frequency that is coupled into it. By changing the angle θ, the emission frequency of the laser diode can be altered. The 0^{th} order diffraction is coupled out of the external resonator and the -1^{st} order diffraction is coupled into the laser diode. The criteria based on which a grating is chosen are that the angle between incident beam and first order diffraction angle should be close to 45°, and the intensity that is coupled back should lie between 20-30%. The efficiency of a grating depends on the total number of illuminated grooves and the polarization of the incident light.

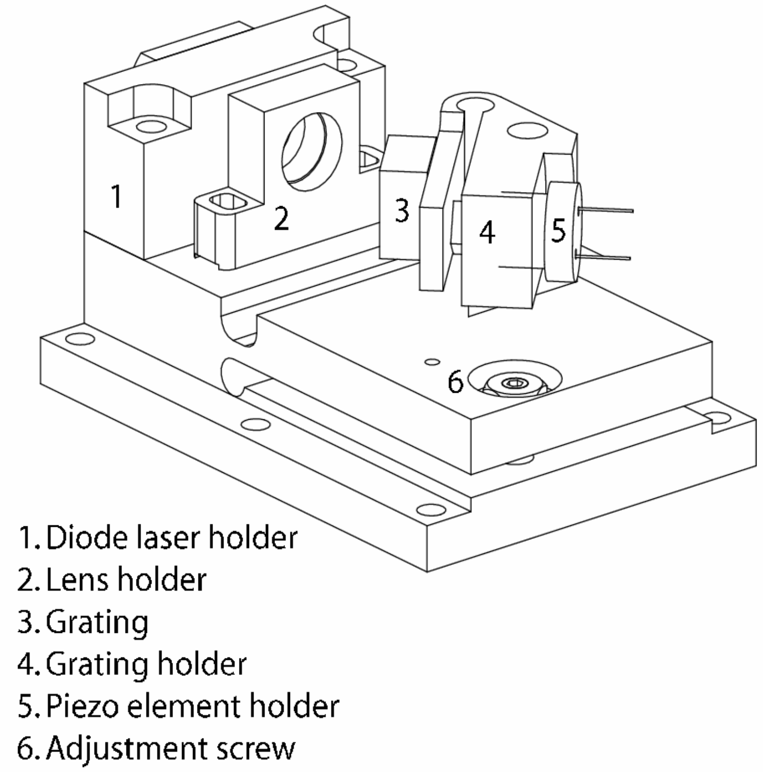

Fig. 4.20: Schematic drawing of the mechanical set up of the external cavity diode laser in Littrow configuration. More details can be found in [18].

ECDL configuration for the lasers of our experiment is achieved using home built mounting systems (Fig. 4.20). The setup consists of a holder for the diode laser, a holder for the collimation optics and an adjustable mount for the grating. A temperature sensor (AD590) measures the temperature of the diode and a TEC element under the laser diode acts as a heat sink. The diode laser is placed inside its mount in such a way that the linear polarization is aligned vertically and hence the narrow expansion of the beam lies in the vertical direction. The polarization is orientated parallel to the grating lines. Afterwards the divergence of the diode is corrected with an aspheric lens which is adjusted so that the output beam is collimated. To align the grating the laser diode current is kept just below the lasing threshold. The grating is placed on the holder and then by shining the laser light on the grating different orders of diffraction are observed. It is fine tuned with the help of two screws, one changes in the vertical plane and the other changes in the horizontal plane. When the -1^{st} order diffraction beam is coupled back to the laser diode the brightness of the emission suddenly increases as a result of the initiation of the lasing action. The threshold of the lasing action is decreased due to the optical feedback that is provided through the -1^{st} order diffraction. Optical feedback is optimized carefully with the internal photodiode equipped with the laser diode. The whole setup is covered with a plastic box to shield the laser diode from temperature drifts and this increases its stability.

The frequency of the lasers in ECDL configuration can be changed by altering the operating current. The frequency can also be changed by altering the external cavity. This can be achieved by changing the temperature of the laser and/or by moving the PZT (piezo electric transducer) mounted grating by varying the voltage applied to the PZT. This alters the angle of incidence (θ) and hence the emission frequency of the laser changes. The PZT element has an extension coefficient of 30(10) nm/V which is a measure of the rate of change of expansion per unit voltage applied. The frequency stabilized laser systems in our experiment have a long-term stability of about several hours. By altering the PZT-mounted grating element together with the operating current, the frequency of the lasers can be scanned over 10 GHz without any mode hop. The 468 nm laser diode is set up with a holographic grating (3600 lines/mm from Edmund Optics) with the angle of incidence at 58°. The 1079 nm laser diode is also set up with a holographic grating (1200 lines/mm from Edmund Optics) with the angle of incidence at 76°.

The cooling laser at wavelength λ_1 drives the $7s\ ^2S_{1/2}$ - $7p\ ^2P_{1/2}$ transition, thereby bringing the ions from ground $7s\ ^2S_{1/2}$ state to excited $7p\ ^2P_{1/2}$ state. From the $7p\ ^2P_{1/2}$ state the ions decay to the metastable $6d\ ^2D_{3/2}$ state with about 10% branching ratio. The repump laser at wavelength λ_2 transfers the ions back to the $7p\ ^2P_{1/2}$ state. These two lasers are employed to demonstrate trapping and optical detection of Ra^+. We are in possession with all lasers for the remaining atomic transitions in Ra^+. They will be set up and made operational in near future.

4.3.2 Lasers for Ba$^+$

Two diode lasers are employed to drive the pump and repump transitions in Ba^+. One drives the cooling and fluorescence transition at 493 nm and excites the ions from the ground $6s\ ^2S_{1/2}$ state to the excited $6p\ ^2P_{1/2}$ state from which they decay to the metastable $5d\ ^2D_{3/2}$ state. To repump the ions back to the $6p\ ^2P_{1/2}$ state a second laser at wavelength of 650 nm is needed. The repump transition is driven with a commercially available diode laser at wavelength 649 nm. The 649 nm laser diode is set up in Littrow configuration with a ruled grating (1800 lines/mm from Edmund Optics) for the angle of incidence at 35°. As there is no laser diode available that directly delivers light at wavelength 493 nm, a high power IR laser diode emitting light at a wavelength of 980 nm is tuned to 987 nm and is frequency doubled. The 980 nm laser diode is also setup in Littrow configuration with a ruled grating (1200 lines/mm from Thorlabs) for the angle of incident at 36°. Light at 987 nm is also available from a Ti:Sapphire laser system (Coherent MBR-110) which is shared with another TRIμP experiment [17]. The Ti:Sapphire laser is arranged in a bow-tie cavity and is specified with a linewidth of 500 kHz. It operates in a wavelength region from 700-1000 nm. At the operating wavelength 987 nm it delivers 300 mW with a pump power of about 8 W. For frequency doubling of the 987 nm light a linear (two mirror) cavity is employed where a potassium niobate ($KNbO_3$) crystal heated to about 75°C causes second harmonic generation and delivers light at 493 nm [106]. The doubling cavity consists of two mirrors which are highly reflective for infrared (99.9% at 965 nm) and highly transmissive for blue. The spacing between the two mirrors is 10 cm. The free spectral range (FSR) and the finesse of the cavity are 1.740(2) GHz and 67(3) respectively.

4.3.3 Overlap of Beams and Measurement of Spot Size

The diameter of the trapped ion cloud is about 1 mm. Hence the spot sizes of the laser beams should be about 1 mm which ensures interaction of photons with the entire ion cloud. Moreover the laser beams should be overlapped at the site of ion cloud to ensure simultaneous interaction of both beams with the same velocity class of ions in the cloud. To satisfy these requirements light from two laser diodes at 468 nm wavelength is overlapped and transported to the ion trap using a single mode optical fiber (460HP). Similarly light from a laser diode at 1079 nm wavelength is transported to the ion trap using a separate single mode optical fiber (1060XP). The laser beams are overlapped using a dichroic mirror just before the trap. The beams are then aligned axially through the trap to minimize stray light. Spot sizes of the laser beams at the site of ion cloud are measured using scanning slit optical beam profilers (BP109-UV and BP109-IR from Thorlabs). At the trap center, typical spot sizes are $\sim$ 1 mm. Light from the lasers for Ba^+ is also transported together with the light at 468 nm in the same fiber. Typical laser intensities at the trap center are 200 μW/mm^2 (λ_1) and 600 μW/mm^2 (λ_2).

4.4 Spectroscopy

Laser spectroscopy is performed by driving optical transitions at wavelengths λ_1 = 468 nm and λ_2 = 1079 nm. The transitions are detected through fluorescence at wavelength λ_1 using a photomultiplier tube. The fluorescence light from the ion cloud is collected with an imaging lens of focal length 30 mm placed inside the vacuum and a low-pass filter with 80% transmission for wavelengths shorter than 500 nm. A schematic diagram for laser spectroscopy is shown in Fig. 4.21.

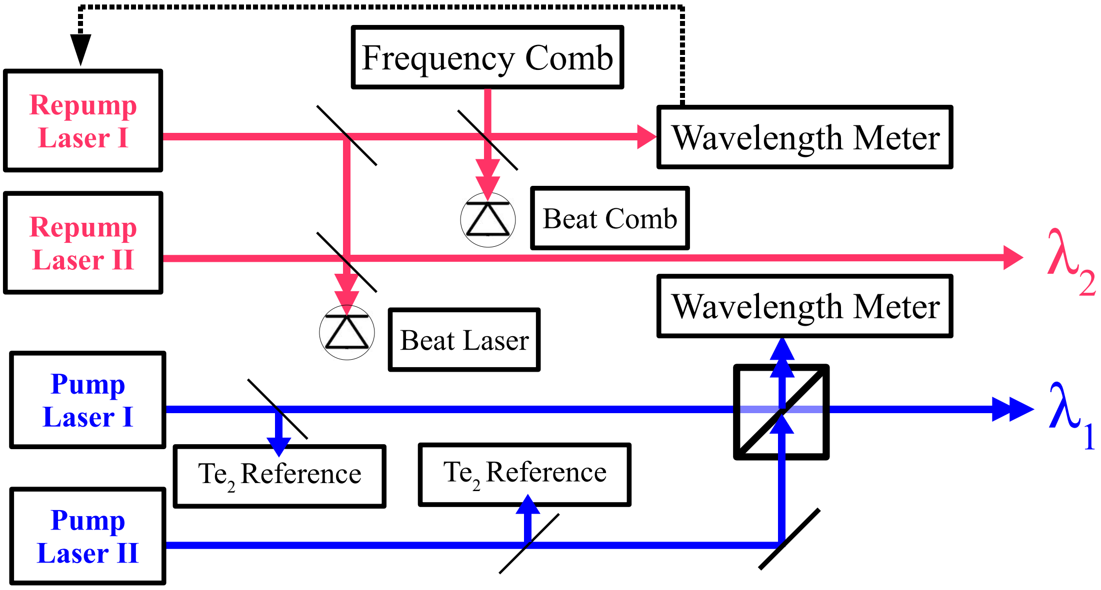

Fig. 4.21: Optical layout for trapping and laser spectroscopy. Repump laser I is continuously locked to the wavelength meter. This is also cross-referenced to the frequency comb and serves as a reference laser. Repump laser II is used for spectroscopy. Both the pump lasers are used for spectroscopy and they are monitored with a tellurium (Te_2) molecular reference.

4.4.1 Absolute and Relative Frequency Calibration

A precise determination of atomic and nuclear properties like hyperfine structure splittings and isotope shifts requires an accurate calibration of the frequency axis. In order to determine the absolute frequency of an atomic transition it needs to be compared to a line of known frequency. A conventional way to do this is to compare the atomic transition to be calibrated with a known molecular

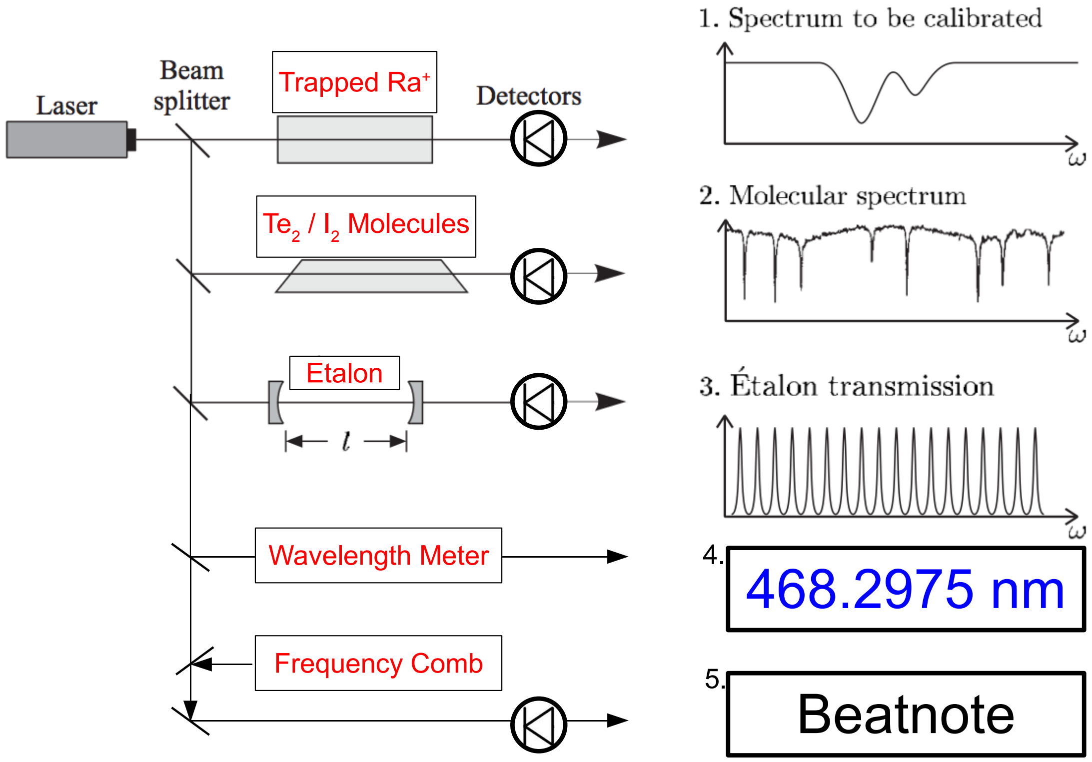

Fig. 4.22: Principle behind frequency calibration. Part of the laser light needed for spectroscopy is used for frequency calibration with Te_2 and I_2 reference lines, etalon, wavelength meter and a frequency comb. Adapted from [107].

transition. Since molecules have many more lines compared to atoms there is a high probability of finding a molecular line of known frequency close to the frequency of interest. Tellurium (Te_2) and iodine (I_2) molecular lines are often used as frequency references. Recently, the optical frequency comb has been evolved to be a tool of interest for absolute frequency calibration. A Fabry-Perot etalon can also be employed for relative calibration. The principle to calibrate the frequency axes for our measurements is shown in Fig. 4.22.

The wavelengths of the lasers are monitored by two commercial wavelength meters (WS6 VIS and WS6 IR from High Finesse-Ångstrom) with an absolute frequency uncertainty of 50 MHz. This is achieved by calibrating them against the molecular iodine I_2 reference line R116(2-9)a15 [108] at $\nu_{I_2} = 419{,}686{,}834(3)$ MHz employing saturated absorption spectroscopy [109].

The laser at wavelength 468 nm is stabilized to a fraction of the Doppler broadened linewidth of about 500 MHz (FWHM). It is monitored with a tellurium absorption line 178 [110] at frequency 640.14652 THz through linear absorption of light in a tellurium glass cell at 500 K. A typical tellurium absorption signal is shown in Fig. 4.23.

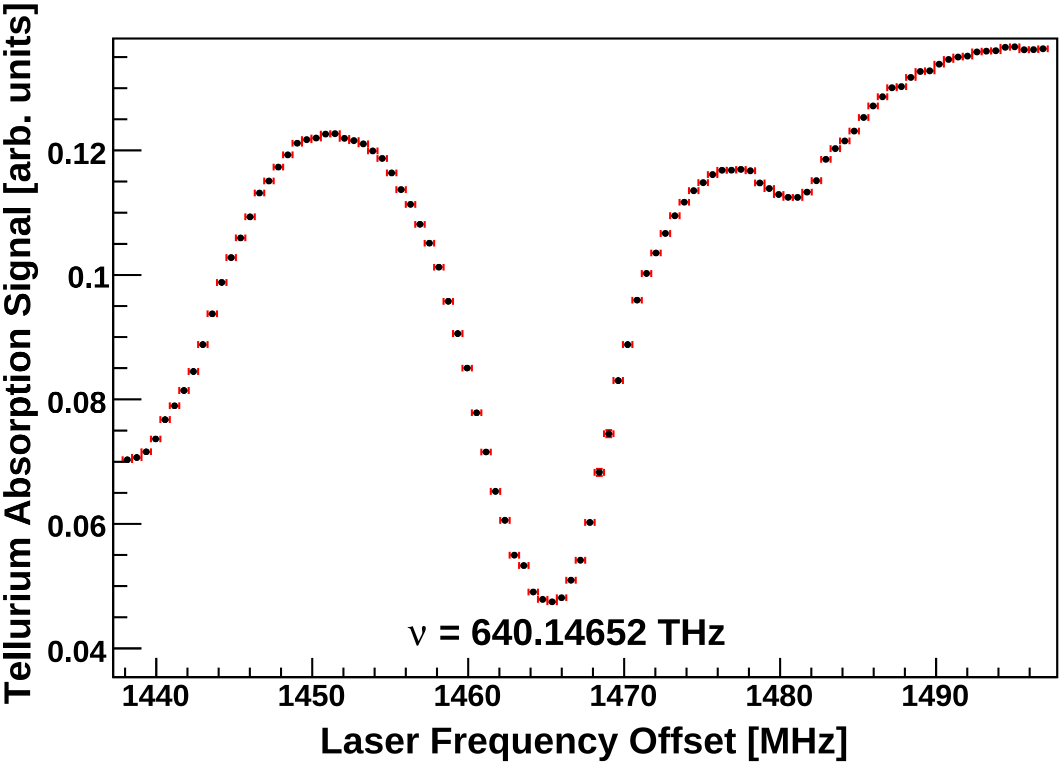

Fig. 4.23: Tellurium molecular absorption line 178 [110] at frequency 640.14652 THz through linear absorption of light in a tellurium glass cell at 500 K. This line provides absolute frequency calibration of light at 468 nm. The $7s\ ^2S_{1/2}$ - $7p\ ^2P_{1/2}$ transition in $^{212}\mathrm{Ra}^+$ is 20 MHz below this line.

The frequency of the laser at 1079 nm is determined with the help of an optical frequency comb. The latter is achieved by employing an auxiliary laser at wavelength λ_2, which is referenced against the frequency comb by a beatnote $f_{\mathrm{BeatComb}} = \nu_{\mathrm{aux}} - \nu_{n^{\mathrm{th}}}$, where ν_{aux} is the frequency of auxiliary laser and $\nu_{n^{\mathrm{th}}}$ is the frequency of the n^{th} comb line. The signal-to-noise ratio of the beatnote is typically 40 dB with 1 MHz bandwidth. The frequency ν_{Laser} of the laser which drives the $6d\ ^2D_{3/2}$ - $7p\ ^2P_{1/2}$ transition is determined by the beatnote frequency $f_{\mathrm{BeatLaser}} = \nu_{\mathrm{Laser}} - \nu_{\mathrm{aux}}$ with the auxiliary laser, yielding

$$\nu_{\mathrm{Laser}} = n \times f_{\mathrm{REP}} + f_{\mathrm{CEO}} + f_{\mathrm{BeatComb}} + f_{\mathrm{BeatLaser}}. \tag{4.6}$$

Here, n is the mode number, f_{REP} = 250,041,000 Hz is the repetition rate and

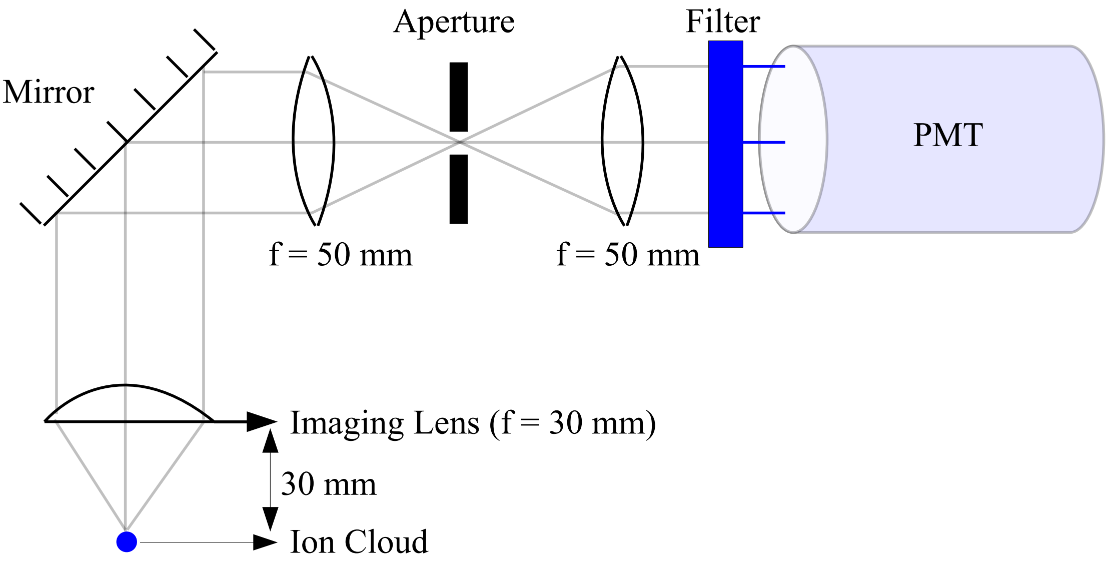

Fig. 4.24: Schematic drawing of optical arrangement for imaging the fluorescence onto the photocathode of a photomultiplier tube. The fluorescence is transported to the photomultiplier tube with a mirror and a pin-hole system with an aperture. The aperture enables to discard unwanted scattered photons.

f_{CEO}=20,000,000 Hz is the carrier-envelope-offset frequency of the comb. The accuracy of the frequency comb is derived from a GPS stabilized Rb clock to be better than 10^{-11} which is not limiting the precision of the results obtained in this work. The sign of $f_{\mathrm{BeatLaser}}$ is either positive or negative depending on the detuning of the scanning laser with respect to the auxiliary laser. The coarse determination of the frequency with the calibrated wavelength meter yields a mode number $n = 1111032$. The uncertainty is only a fraction (0.2) of one mode spacing due to the calibration accuracy of the wavelength meter. This results in the frequency of the n^{th} comb line $\nu_{n^{\mathrm{th}}} =$ 277,803,572.31(3) MHz, where the uncertainty arises from the Rb clock.

4.4.2 Imaging System and Optical Detection

The fluorescence light at wavelength λ_1 from the trapped ions is detected using a photomultiplier tube (R7449 from Hamamatsu Corp.). A narrow band interference filter FB470-10 or short-pass filter FES0500 (both from Thorlabs Inc.) can be used in front of the photomultiplier tube to filter the fluorescence at wavelength λ_1, for which FB470-10 has a transmission of 50% and FES0500 has a transmission of 80%. The short pass filter FES0500 can also filter fluorescence from Ba^+ transition (493 nm) in addition to the fluorescence from Ra^+ transition (468 nm). Hence we choose a FES0500 filter which enables us to perform both diagnostics and actual measurements without disturbing the imaging and detection system. A schematic drawing of imaging and optical detection system is shown in Fig. 4.24. The imaging system consists of a plano-convex lens of focal length f=30 mm, mounted inside the vacuum. It is at a distance of 30(5) mm from the trap center and collects fluorescence from the trapped ions with a solid angle Ω=0.4 sr.

4.5 Computer Control and Data Acquisition

Experimental data are taken with a data acquisition system based on the software package ROOT [111] into which the measurement hardware is network integrated. ROOT serves as an interface for experimental control. A program script running in ROOT is used to start and stop acquisition runs and also to provide a sequence of shutting laser beams after beginning a data run for normalization. Different experimental parameters are controlled remotely from the data acquisition computer. Such parameters include the currents in the dipole and the quadrupole magnets of the separator, the voltages of the low energy beam line, the voltages of the ion trap, the status of the laser shutters, the laser frequencies etc.

Chapter 5

Spectroscopy of Short-Lived Radium Isotopes in an Ion Trap

Precision laser spectroscopy of trapped radium ions in a linear Paul trap provides a new quality to the spectroscopic data which are relevant for the development of an experiment to measure the parity violating weak interaction effects in this system. Here we present and discuss the measurements of hyperfine structures, isotopes shifts, and lifetime, using trapped radium ions in a linear Paul trap. The measurements provide the following results.

- Hyperfine structure intervals of the $6d\ ^2D_{3/2}$ state in $^{209,211,213}\mathrm{Ra}^+$.
- Isotope shifts of the $6d\ ^2D_{3/2}$ - $7p\ ^2P_{1/2}$ transition (1079 nm) in $^{209-214}\mathrm{Ra}^+$.
- Isotope shifts of the $6d\ ^2D_{3/2}$ - $7p\ ^2P_{3/2}$ transition (708 nm) in $^{212-214}\mathrm{Ra}^+$.
- Lifetime of the $6d\ ^2D_{5/2}$ state in $^{212}\mathrm{Ra}^+$.

The results provide a benchmark for the required atomic theory, the precision of which is indispensable for the interpretation of results from the planned measurement of parity violation in Ra^+.

5.1 Hyperfine Structure Interval of $6d\ ^2D_{3/2}$ State

A description of hyperfine structure is given in Appendix B. Elaborate details can be found in atomic physics textbooks [107,112,113]. We have measured the hyperfine structure interval of the $6d\ ^2D_{3/2}$ state in three isotopes with $I\neq 0$. The isotopes we have studied are $^{213}\mathrm{Ra}^+$ (I=1/2) and $^{209,211}\mathrm{Ra}^+$ (I=5/2). The relevant level schemes are shown in Fig. 5.1.

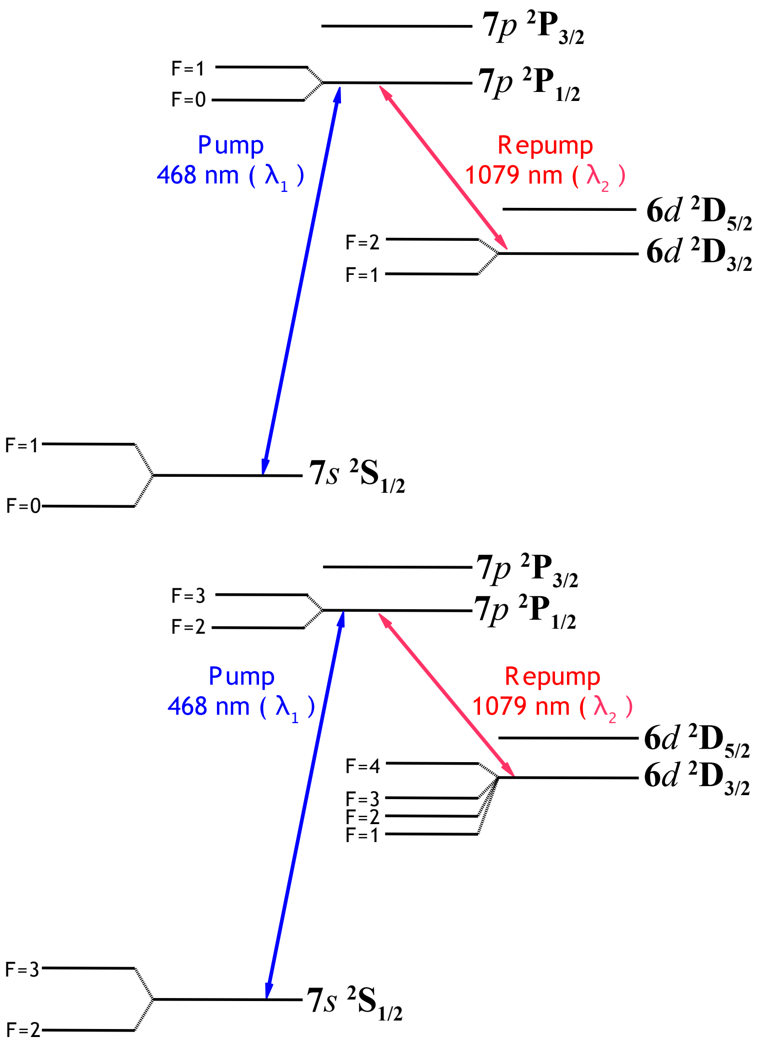

Fig. 5.1: Level schemes of odd isotopes with hyperfine structures. Upper and lower figures correspond to ^{213}Ra$^+$ (I=1/2) and ^{209,211}Ra$^+$ (I=5/2) respectively.

To measure the hyperfine structure interval of the $6d\ ^2D_{3/2}$ state in ^{213}Ra$^+$, frequencies of the light from two pump lasers at wavelengths λ_1 are tuned to continuously pump each hyperfine level (F=0 and F=1) of the ground $7s\ ^2S_{1/2}$ state, thereby exciting the ions to both hyperfine levels (F=0 and F=1) of the excited $7p\ ^2P_{1/2}$ state. The hyperfine structure interval of the $7s\ ^2S_{1/2}$ state in ^{213}Ra$^+$ has been determined to be 22920(6) MHz [79]. Hence two lasers are employed to pump the ground state hyperfine levels. From the excited $7p\ ^2P_{1/2}$ hyperfine levels, the ions decay to the metastable $6d\ ^2D_{3/2}$ hyperfine levels (F=1 and F=2). Light from a repump laser at wavelength λ_2 is scanned over the $6d\ ^2D_{3/2}$(F=1, 2) - $7p\ ^2P_{1/2}$(F=0, 1) resonances. Many such scans are averaged to obtain a good signal-to-noise ratio. Data are collected for a few hours to accumulate enough statistics. The observed resonances are shown in Fig. 5.2.

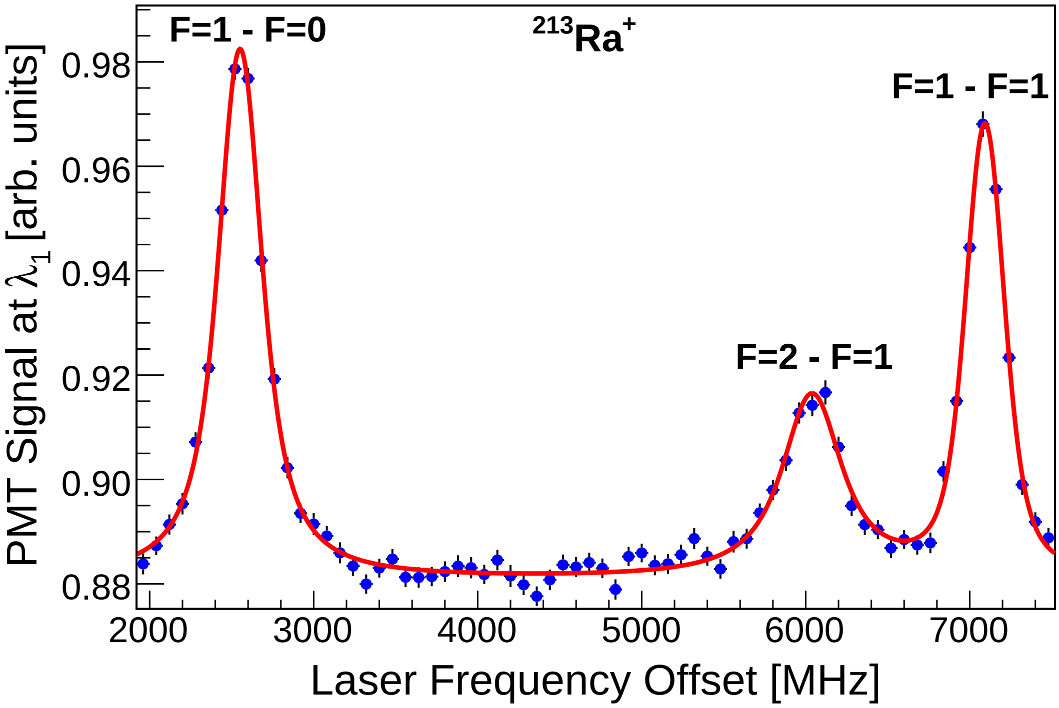

Fig. 5.2: Hyperfine structure intervals of $6d\ ^2D_{3/2}$ and $7p\ ^2P_{1/2}$ states in ^{213}Ra$^+$. The solid line represents a fit of three Voigt profiles to the data. The Gaussian widths of the transitions are 181(20) MHz (FWHM).

For this measurement nitrogen (N_2) is used as a buffer gas at 3×10^{-3} mbar. This results in hyperfine mixing of the $6d\ ^2D_{3/2}$ hyperfine levels. This effect prevents any possible shelving of ions to the metastable $6d\ ^2D_{3/2}$ F=1 or F=2 state while the $6d\ ^2D_{3/2}$ F=2 or F=1 state is depopulated by the resonant light at wavelength λ_2. The frequency is calibrated with an infrared wavelength meter. The measured hyperfine structure interval of 4542(7) MHz for the $7p\ ^2P_{1/2}$ state is within 2 standard deviations off the value 4525(5) MHz as measured at ISOLDE [79]. The hyperfine structure interval for the $6d\ ^2D_{3/2}$ state is measured as 1055(10) MHz. The hyperfine structure constants A for the $6d\ ^2D_{3/2}$ and $7p\ ^2P_{1/2}$ states are listed in Table 5.1. The theoretical values [26,84] quoted in Table 5.1 are calculated for ^{213}Ra$^+$ by scaling with $I/I' \times \mu_I'/\mu_I$. The relevant nuclear magnetic moments (μ_I) and the electric quadrupole moments are taken from [81, 83].

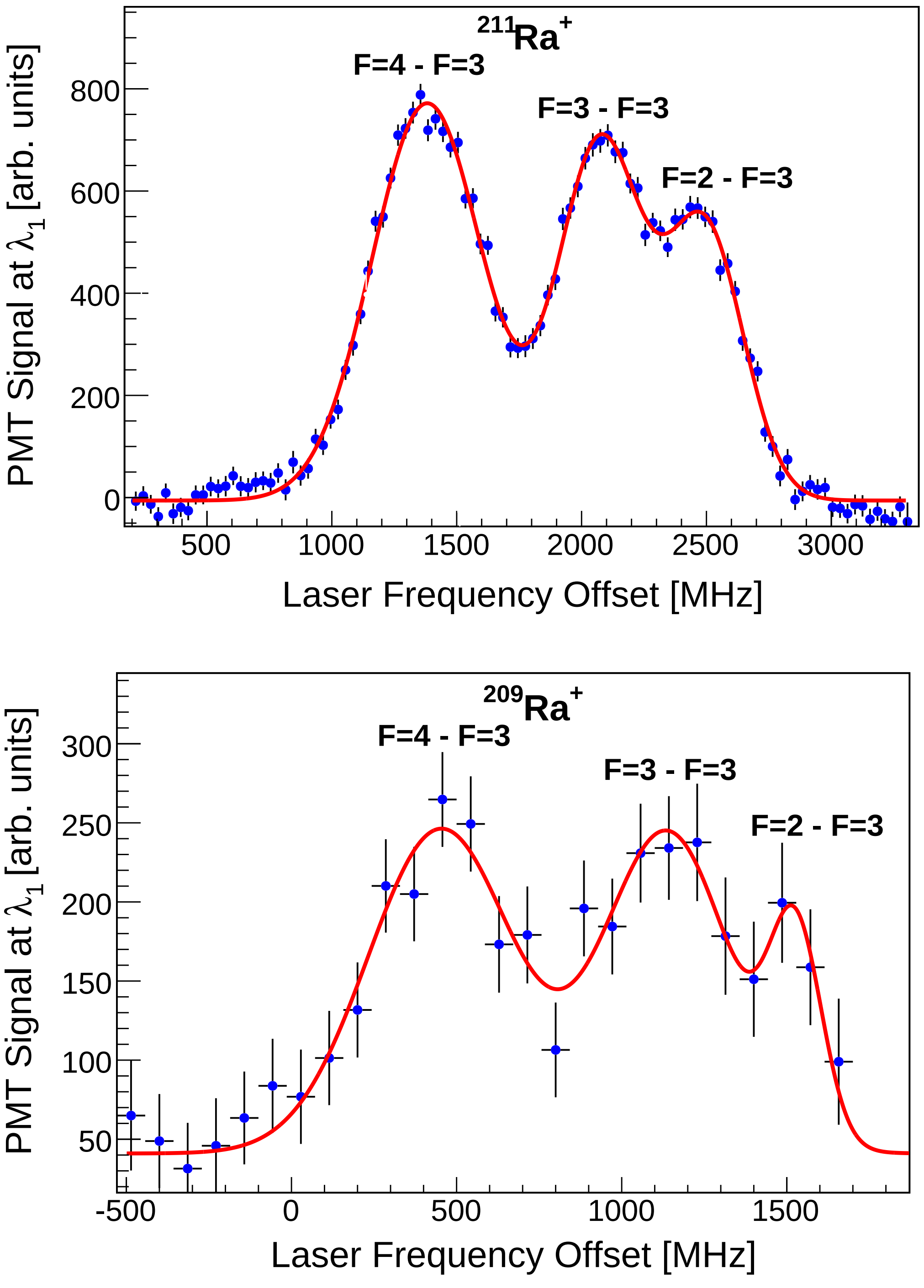

Fig. 5.3: Hyperfine structure intervals of the $6d\ ^2D_{3/2}$ states in ^{209,211}Ra$^+$. $6d\ ^2D_{3/2}$(F=2,3,4) - $7p\ ^2P_{1/2}$(F=3) transitions are shown. The solid line in each case represents a fit of three Gaussian functions to the data. The top and bottom figures correspond to ^{211}Ra$^+$ and ^{209}Ra$^+$ respectively.

To measure the hyperfine structure intervals of the $6d\ ^2D_{3/2}$ states in ^{209,211}Ra$^+$, frequencies of the light from two pump lasers at wavelengths λ_1 are tuned to continuously pump both hyperfine levels (F=2 and F=3) of the ground $7s\ ^2S_{1/2}$ state for the isotope under investigation. The hyperfine structure interval of the $7s\ ^2S_{1/2}$ state in ^{211}Ra$^+$ has been determined to be 19874.4(3.0) MHz [79]. Though there is no reported value for ^{209}Ra$^+$, it is expected to be comparable to that of ^{211}Ra$^+$ due to the fact that the two isotopes have comparable mass and identical nuclear spin. The two pump lasers excite the ions to the hyperfine level F=3 of the excited $7p\ ^2P_{1/2}$ state from which the ions decay to the three out of the four metastable $6d\ ^2D_{3/2}$ hyperfine levels (F=2, 3, 4). This pumping scheme ensures that ions do not decay to the $6d\ ^2D_{3/2}$(F=1) state. Light from a repump laser at wavelength λ_2 is scanned over the $6d\ ^2D_{3/2}$(F=2, 3, 4) - $7p\ ^2P_{1/2}$(F=3) resonances of the isotope under investigation. Many such scans are averaged to obtain a good signal-to-noise ratio. Data were collected for a few hours to accumulate enough statistics and to resolve the lines. The observed resonances are shown in Fig. 5.3. In case of ^{209}Ra$^+$, the signal-to-noise ratio is very low. This is a consequence of very low production yield and shorter lifetime of this particle as discussed in section 4.1.5.

For these measurements neon (Ne) is used as a buffer gas. To ensure collision induced hyperfine mixing of the $6d\ ^2D_{3/2}$ hyperfine levels, a higher buffer gas pressure (1×10^{-2} mbar) is used, which is different from the measurements in ^{213}Ra$^+$. This effect prevents any possible shelving of ions to the metastable $6d\ ^2D_{3/2}$ hyperfine levels while the $6d\ ^2D_{3/2}$ state is depopulated by the resonant light at wavelength λ_2. The frequency is calibrated with a reference laser which is referenced to an optical frequency comb. The hyperfine structure constants A and B for the $6d\ ^2D_{3/2}$ state are listed in Table 5.2. The theoretical values [75]

Table 5.1: Hyperfine structure constants $A(6d\ ^2D_{3/2})$ and $A(7p\ ^2P_{1/2})$ for ^{213}Ra$^+$. The most recent theoretical values are scaled for ^{213}Ra$^+$ using $I/I' \times \mu_I'/\mu_I$ with the experimentally measured magnetic moments [83].

	$A(6d\ ^2D_{3/2})$ MHz	$A(7p\ ^2P_{1/2})$ MHz
This work	528(5)	4542(7)
ISOLDE [79]	-	4525(5)
Theory [26]	543	4555
Theory [84]	541	4565

Table 5.2: Hyperfine structure constants $A(6d\ ^2D_{3/2})$ and $B(6d\ ^2D_{3/2})$ for ^{209,211}Ra$^+$.

Isotope	$A(6d\ ^2D_{3/2})$ MHz	$B(6d\ ^2D_{3/2})$ MHz
^{211}Ra$^+$	151(2)	103(6)
	150*	147*
^{209}Ra$^+$	148(10)	104(38)
	148*	122*

*The most recent theoretical values [75] are scaled for ^{209,211}Ra$^+$ using the experimentally measured magnetic and quadrupole moments [81, 83].

quoted in Table 5.2 are calculated for ^{209,211}Ra$^+$ by scaling with $I/I' \times \mu_I'/\mu_I$ for the hyperfine constant A and with $I/I' \times Q_I'/Q_I$ for the hyperfine constant B. The relevant nuclear magnetic moments (μ_I) and the electric quadrupole moments (Q_I) are taken from [81, 83].

To summarize, we have measured the hyperfine structure intervals of the $6d\ ^2D_{3/2}$ states in three isotopes with $I\neq0$. They are listed in Table 5.3. The $6d\ ^2D_{3/2}$ state is of particular importance for the $7s\ ^2S_{1/2}$ - $6d\ ^2D_{3/2}$ transition relevant for the planned APV measurement in Ra$^+$. The measured hyperfine structure intervals and the corresponding hyperfine constants A and B as listed in Table 5.1 and 5.2 are an important probe of the atomic wavefunction in Ra$^+$.

Table 5.3: Hyperfine structure intervals between the hyperfine levels F and F-1 for the $6d\ ^2D_{3/2}$ state in ^{209,211,213}Ra$^+$.

	211Ra$^+$(I=5/2)	209Ra$^+$(I=5/2)	213Ra$^+$(I=1/2)
F	ΔE MHz	ΔE MHz	ΔE MHz
4	686(9)	673(28)	-
3	407(7)	396(49)	-
2	-	-	1055(10)

5.2 Isotope Shifts

A description of isotope shifts is given in Appendix C. Elaborate details can be found in atomic physics textbooks [107, 112, 113]. We have measured isotope

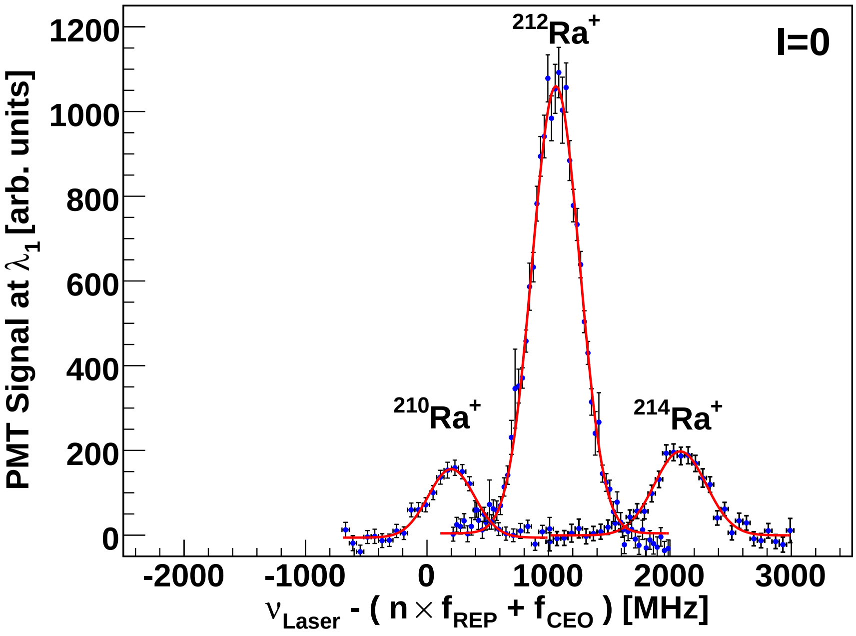

Fig. 5.4: Isotope shift of $6d\ ^2D_{3/2}$ - $7p\ ^2P_{1/2}$ transition in ^{210,212,214}Ra$^+$. The solid line represents in each case a fit of a Gaussian function to the data.

shifts of the $6d\ ^2D_{3/2}$ - $7p\ ^2P_{1/2}$ tansition in six isotopes and shifts of the $6d\ ^2D_{3/2}$ - $7p\ ^2P_{3/2}$ tansition in three isotopes.

5.2.1 Isotope Shifts of $6d\ ^2D_{3/2}$ - $7p\ ^2P_{1/2}$ Transition

Isotope shifts have been measured for the $6d\ ^2D_{3/2}$ - $7p\ ^2P_{1/2}$ transition in $^{209-214}$Ra$^+$. Determination of isotope shifts for a transition in a range of isotopes requires knowledge of the frequencies of the transition for all the concerned isotopes relative to a common frequency reference. For the results reported here, a frequency comb serves as the reference to which relative differences in the frequencies are determined.

For the isotopes with I=0 (^{210,212,214}Ra$^+$) the frequencies of the $6d\ ^2D_{3/2}$ - $7p\ ^2P_{1/2}$ transition are determined with light from one laser at wavelength λ_1 which continuously pumps the ground $7s\ ^2S_{1/2}$ state to the excited $7p\ ^2P_{1/2}$ state from which the ions decay to the $6d\ ^2D_{3/2}$ state with about 10% branching ratio. Light from another laser at wavelength λ_2 is scanned over the resonance of $6d\ ^2D_{3/2}$ - $7p\ ^2P_{1/2}$ transition. The observed resonances are shown in Fig. 5.4.

The principle of measurement as described for the measurement of hyper-

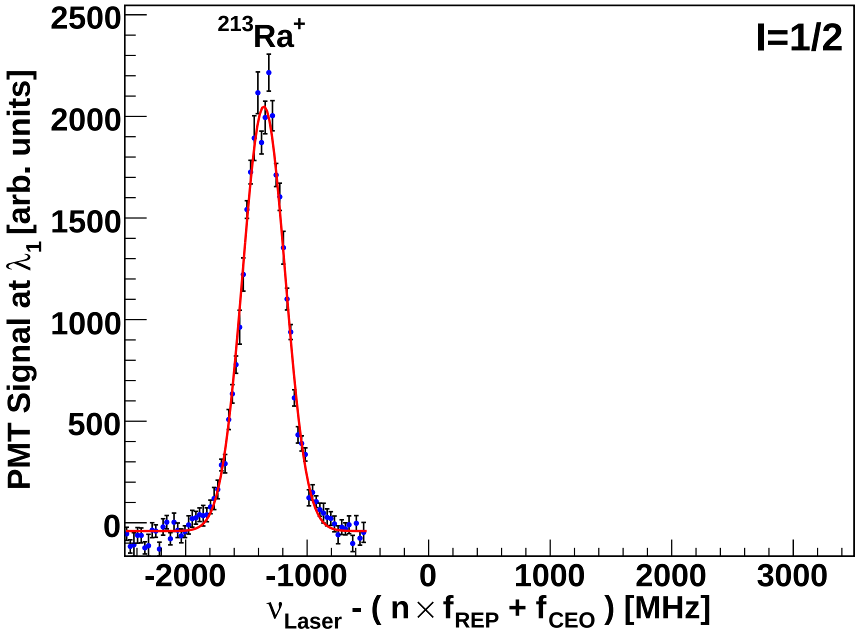

Fig. 5.5: Isotope shift of $6d\ ^2D_{3/2}$ - $7p\ ^2P_{1/2}$ transition in ^{213}Ra$^+$. $6d\ ^2D_{3/2}$(F=0)-$7p\ ^2P_{1/2}$(F=1) transition is shown. The solid line represents a fit of a Gaussian function to the data.

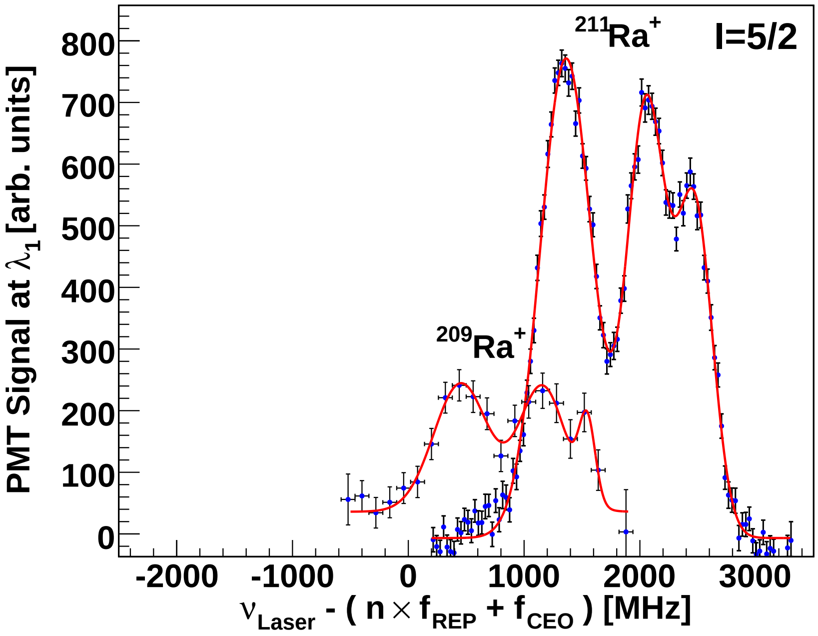

Fig. 5.6: Isotope shift of $6d\ ^2D_{3/2}$ - $7p\ ^2P_{1/2}$ transition in ^{209,211}Ra$^+$. $6d\ ^2D_{3/2}$(F=2, 3, 4) - $7p\ ^2P_{1/2}$(F=3) transitions are shown, where the peaks at the lowest frequency in each case correspond to the $6d\ ^2D_{3/2}$(F=4) - $7p\ ^2P_{1/2}$(F=3) transition. The solid line represents in each case a fit of three Gaussian functions to the data.

fine structure applies for the isotopes with $I \neq 0$ (^{209,211,213}Ra$^+$). The measured transitions are shown in Figs. 5.5 and 5.6.

For the measurement of isotopes shifts only neon is used in order to minimize the influence of buffer gas on the resonance line shapes. As shown in Figs. 5.4-5.6 all the measured transitions have been calibrated to a common frequency axis where the offset frequency of the laser has been given relative to the n=1111032 comb line which has an absolute frequency of 277,803,572.31(3) MHz. The principle of absolute calibration for the 6d $^2D_{3/2}$ - 7p $^2P_{1/2}$ transition has been given section 4.4.1.

5.2.2 Isotope Shifts of 6d $^2D_{3/2}$ - 7p $^2P_{3/2}$ Transition

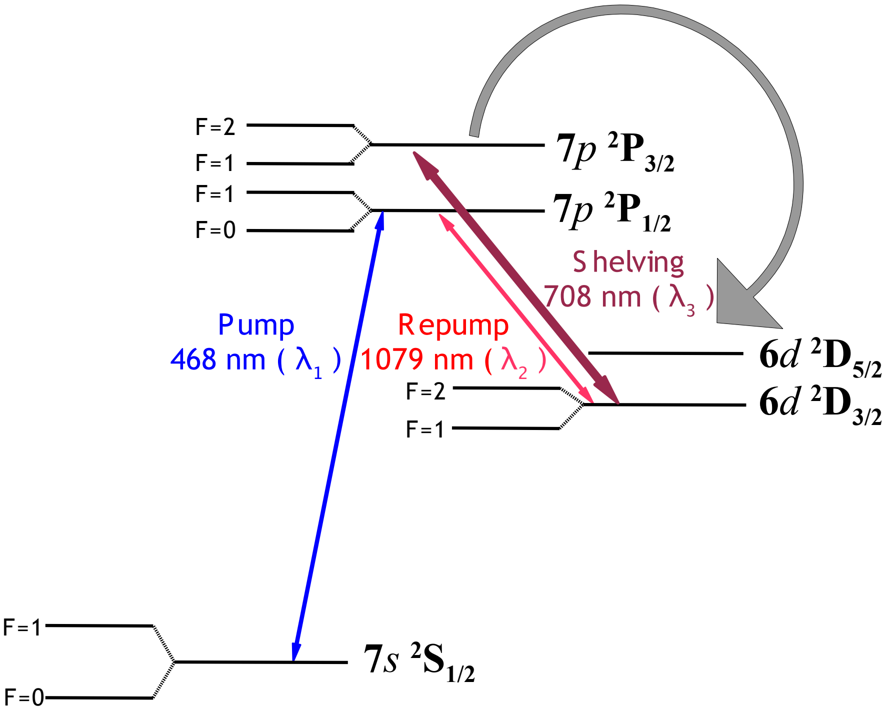

Fig. 5.7: Level scheme of ^{213}Ra$^+$ showing the 6d $^2D_{3/2}$ - 7p $^2P_{3/2}$ shelving transition.

Isotope shifts have been measured for the 6d $^2D_{3/2}$ - 7p $^2P_{3/2}$ transition in ^{212,213,214}Ra$^+$. For this measurement a third laser at wavelength λ_3=708 nm is employed in addition to the pump and repump lasers as described in the previous measurements. The relevant level scheme is shown in Fig. 5.7.

To determine the isotope shifts of the 6d $^2D_{3/2}$ - 7p $^2P_{3/2}$ transition, the lasers

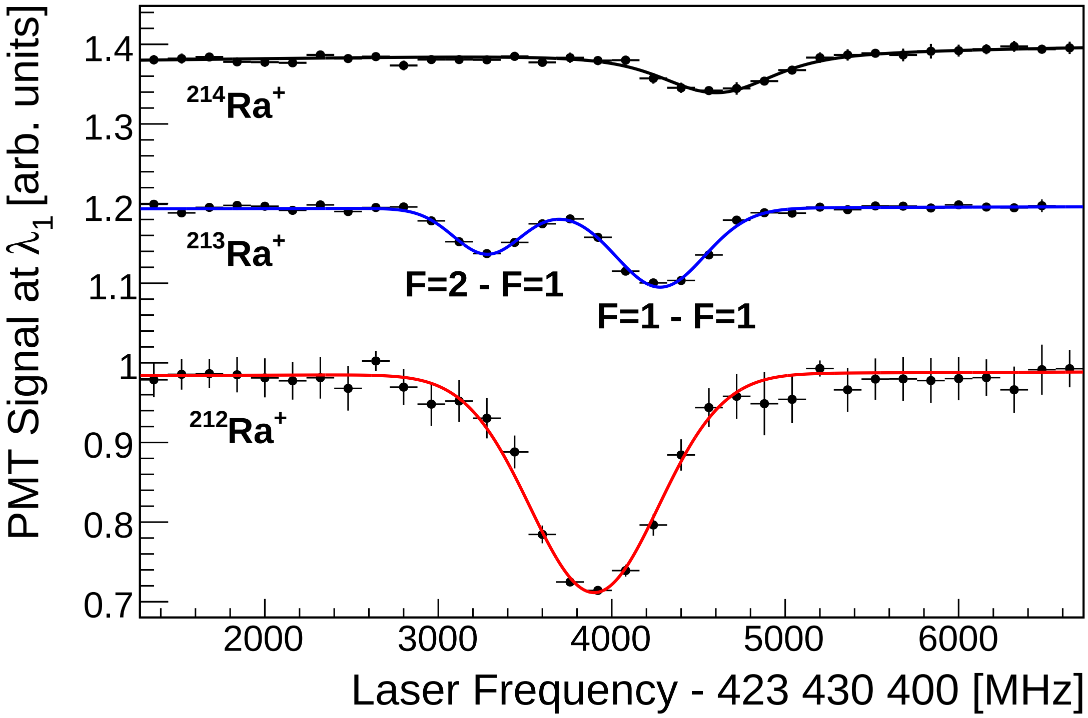

Fig. 5.8: Isotope shifts of $6d\ ^2D_{3/2}$ - $7p\ ^2P_{3/2}$ transition in ^{212,213,214}Ra$^+$. The solid lines represent in each case a fit of a Voigt profile to the data. The different Gaussian widths are due to different buffer gas pressures at which the measurements are carried out.

operating at wavelengths λ_1 and λ_2 are tuned to frequencies corresponding to the resonances for the $7s\ ^2S_{1/2}$ - $7p\ ^2P_{1/2}$ transition and $6d\ ^2D_{3/2}$ - $7p\ ^2P_{1/2}$ transition respectively, for the isotope under investigation. This creates a fluorescence cycle. The frequency of the laser light at λ_3 is scanned over the $6d\ ^2D_{3/2}$ - $7p\ ^2P_{3/2}$ resonance. Near resonance the ions are pumped from the $6d\ ^2D_{3/2}$ state to the $7p\ ^2P_{3/2}$ state, from which about 10% of the ions decay to the $6d\ ^2D_{5/2}$ state. This is a metastable state where the ions are shelved and they no longer remain in the fluorescence cycle. This creates a dip in the fluorescence signal. This is also known as dark resonance.

By pumping on the $7s\ ^2S_{1/2}$(F=1) - $7p\ ^2P_{1/2}$(F=0) transition and repumping on the $6d\ ^2D_{3/2}$(F=1) - $7p\ ^2P_{1/2}$(F=0) transition, the fluorescence cycle is established for ^{213}Ra$^+$. This leaves the $6d\ ^2D_{3/2}$(F=2) state largely depopulated. The $6d\ ^2D_{3/2}$(F=1) - $7p\ ^2P_{3/2}$(F=1) resonance is deformed by the close lying $6d\ ^2D_{3/2}$(F=2) - $7p\ ^2P_{3/2}$(F=2) resonance. The $6d\ ^2D_{3/2}$(F=2) - $7p\ ^2P_{3/2}$(F=1) resonance has been used to determine the isotope shift of $^{213}\mathrm{Ra}^{+}$.

The transitions observed are shown in Fig. 5.8. These measurements have been performed at different gas pressures 3×10^{-3}, 2×10^{-3}, 2×10^{-2} mbar with neon as the buffer gas.

5.2.3 Data Analysis and Results

The isotope shifts of a spectral line are usually parameterized as [114],

$$\delta\nu_{MM'} = (K_{\mathrm{NMS}} + K_{\mathrm{SMS}})\frac{M - M'}{MM'} + F_{\mathrm{FS}}\delta\langle r^2\rangle_{MM'} \tag{5.1}$$

where $\delta\nu_{MM'} = \nu_M - \nu_{M'}$. M and M$'$ are the masses of the reference isotope and the isotope of interest respectively, both in atomic mass units. K_{NMS} and K_{SMS} are the normal and specific mass shift components and F_{FS} is the field shift component. $\delta\langle r^2\rangle_{MM'}$ is the difference in mean square nuclear charge radii, which is common to all transitions for a pair of nuclei. Both the specific mass shift and the field shift are characteristic to a particular transition. Here they are defined as the shift of the lower level, minus the shift of the upper level. The normal mass shift can be calculated from the expression $K_{\mathrm{NMS}} = \nu m_e$, where ν is the transition frequency and m_e is the mass of electron in atomic mass units.

A King plot analysis [115] is used to separate the specific mass shift and the field shift components. Here the transformed isotope shifts ($\Delta\nu^{\mathrm{King}}_{MM'}$) are taken, which are obtained by subtracting the normal mass shift component from the experimentally measured isotope shifts and multiplying both sides of Eq. (5.1) by $MM'/(M - M')$. Eq. (5.1) is rewritten as

$$\Delta\nu^{\mathrm{King}}_{MM'} = K_{\mathrm{SMS}} + F_{\mathrm{FS}}\ \delta\langle r^2\rangle_{MM'}\frac{MM'}{M - M'} \tag{5.2a}$$

$$= \delta\nu_{MM'}\frac{MM'}{M - M'} - K_{\mathrm{NMS}}. \tag{5.2b}$$

In a comparison between two different optical transitions i and j, the transformed isotope shifts can be written as

$$\Delta\nu^{j,\mathrm{King}}_{MM'} = \frac{F^j_{FS}}{F^i_{FS}}\Delta\nu^{i,\mathrm{King}}_{MM'} + K^j_{SMS} - \frac{F^j_{FS}}{F^i_{FS}}K^i_{SMS}. \tag{5.3}$$

This is essentially a linear relation of the transformed isotope shifts of one transition ($\Delta\nu^{j,\mathrm{King}}_{MM'}$) against the corresponding shifts of the other transition ($\Delta\nu^{i,\mathrm{King}}_{MM'}$). The slope yields the ratio of field shifts and the difference in specific mass shifts appears as the crossing with the abscissa.

Table 5.4: Isotope shifts of $6d\ ^2D_{3/2}$ - $7p\ ^2P_{1/2}$ transition in $^{209-214}$Ra$^+$ with the relevant hyperfine constants. The comparatively large error bar on the isotope shift of ^{209}Ra$^+$ is a consequence of low signal-to-noise ratio due to lower yield and shorter life time of the isotope. $\delta\nu_{214,M'}$ is the shift of the $6d\ ^2D_{3/2}$ - $7p\ ^2P_{1/2}$ transition with respect to ^{214}Ra$^+$.

Mass Number	$A(6d\ ^2D_{3/2})$ MHz	$B(6d\ ^2D_{3/2})$ MHz	$A(7p\ ^2P_{1/2})$ MHz	$\delta\nu_{214,M'}$ MHz
214	-	-	-	0
213	528(5)	-	4525(5) [79]	707(14)
212	-	-	-	1025(12)
211	151(2)	103(6)	1299.7(0.8) [79]	1755(14)
210	-	-	-	1884(16)
209	148(10)	104(38)	1276(20)[a]	2645(56)

---

[a] Calculated using Eq. 5.4.

^{214}Ra$^+$ has been chosen as the reference isotope in order to be consistent with previous work [79]. The difference in transition frequencies for the even isotopes yields directly the isotope shift. For ^{209,211,213}Ra$^+$($I\neq0$) the isotope shifts are given between the centers of gravity of the $6d\ ^2D_{3/2}$ and $7p\ ^2P_{1/2}$ states. This requires the magnetic dipole A and the electric quadrupole B hyperfine constants for those states (Table 5.4). For the $6d\ ^2D_{3/2}$ state, the hyperfine constants have been derived from measured hyperfine intervals. The hyperfine constants A for the $7p\ ^2P_{1/2}$ state are taken from [79]. For the case of ^{209}Ra$^+$ no value has been reported. It is derived with the nuclear magnetic moments μ [83] using

$$\frac{A(7p\,^2P_{1/2},^{209}\mathrm{Ra}^+)}{A(7p\,^2P_{1/2},^{213}\mathrm{Ra}^+)} = \frac{I(^{213}\mathrm{Ra}^+)}{I(^{209}\mathrm{Ra}^+)} \times \frac{\mu(^{209}\mathrm{Ra}^+)}{\mu(^{213}\mathrm{Ra}^+)}. \tag{5.4}$$

The measured isotope shifts for all the even and odd isotopes ($^{209-214}$Ra$^+$) and the relevant hyperfine constants for the $6d\ ^2D_{3/2}$ and $7p\ ^2P_{1/2}$ states in case of isotopes with $I\neq0$ are given in Table 5.4.

A King plot of the transformed isotope shifts of the measured $6d\ ^2D_{3/2}$ - $7p\ ^2P_{1/2}$ transition against the corresponding shifts of the $7s\,^1\mathrm{S}_0$ - $7s7p\,^1\mathrm{P}_1$ transition in neutral radium [79] is shown in Fig. 5.9. The values for the atomic masses of the isotopes are taken from [116]. The normal mass shift coefficient of the $6d\ ^2D_{3/2}$ - $7p\ ^2P_{1/2}$ transition in ionic radium is $K_{\mathrm{NMS}} = 152.4$ GHz amu. For the $7s\,^1\mathrm{S}_0$ - $7s7p\,^1\mathrm{P}_1$ transition in neutral radium, the normal mass shift coeffi-

Table 5.5: Isotope shifts of $6d\ ^2D_{3/2}$ - $7p\ ^2P_{3/2}$ transition in $^{212-214}$Ra$^+$. All values are in MHz. $\delta\nu_{214,M'}$ is the isotope shift of the $6d\ ^2D_{3/2}$ - $7p\ ^2P_{3/2}$ transition with respect to ^{214}Ra$^+$.

Mass Number	$\delta\nu_{214,M'}$ MHz
214	0
213	453(34)
212	701(50)

cient is $K_{\mathrm{NMS}} = 340.8$ GHz amu. Plotting the transformed isotope shifts against each other shows that the data satisfies a linear relation within the measurement uncertainties (Fig. 5.9). The slope determines the ratio of field shift coefficients, $F_{FS}^{1079\text{ nm}}/F_{FS}^{482\text{ nm}} = -0.342(15)$. The abscissa determines the difference of the specific mass shift to be $-1.9(1.1)$ THz amu.

The frequency of the measured $6d\ ^2D_{3/2}$ - $7p\ ^2P_{3/2}$ resonances are calibrated against the P(146)(2-8) single pass absorption resonance in molecular iodine (I_2) at ν_{Iodine}=423,433,720 MHz [108]. The frequencies of the $6d\ ^2D_{3/2}$ - $7p\ ^2P_{3/2}$ transitions relative to the molecular iodine reference line, ν_{Ra^+} - ν_{Iodine}, are found to be +568(42) MHz, -64(13) MHz, and +1269(23) MHz for ^{212}Ra$^+$, ^{213}Ra$^+$, and ^{214}Ra$^+$ respectively. The linearity of the scan of the laser has been verified with a cavity of finesse 1200 and free spectral range (FSR) 10 GHz. The measured isotope shifts are listed in Table 5.5.

The isotope shifts of the $6d\ ^2D_{3/2}$ - $7p\ ^2P_{3/2}$ transition are measured with reference to ^{214}Ra$^+$. For ^{213}Ra$^+$, the determination of isotope shift requires knowledge of the hyperfine constant A for the $7p\ ^2P_{3/2}$ state which is not reported. Hence it is extracted using the measured values for the $6d\ ^2D_{3/2}$ state and the values reported in [79,81,83]. A King plot of the $6d\ ^2D_{3/2}$ - $7p\ ^2P_{3/2}$ transition (708 nm) against the $6d\ ^2D_{3/2}$ - $7p\ ^2P_{1/2}$ transition (1079 nm) in Ra$^+$ is shown in Fig. 5.10.

To summarize, we have measured the isotope shifts of $6d\ ^2D_{3/2}$ - $7p\ ^2P_{1/2}$ transition in $^{209-214}$Ra$^+$ and the shifts of $6d\ ^2D_{3/2}$ - $7p\ ^2P_{3/2}$ transition in $^{212-214}$Ra$^+$. The isotope shifts of the transitions from the metastable $6d\ ^2D_{3/2}$ state are of particular importance beacause they are sensitive to the short range part of the atomic wavefunctions. The measured isotope shifts are listed in Table 5.4 and 5.5 respectively. They are an important probe of the atomic wavefunctions and the nuclear shape and size.

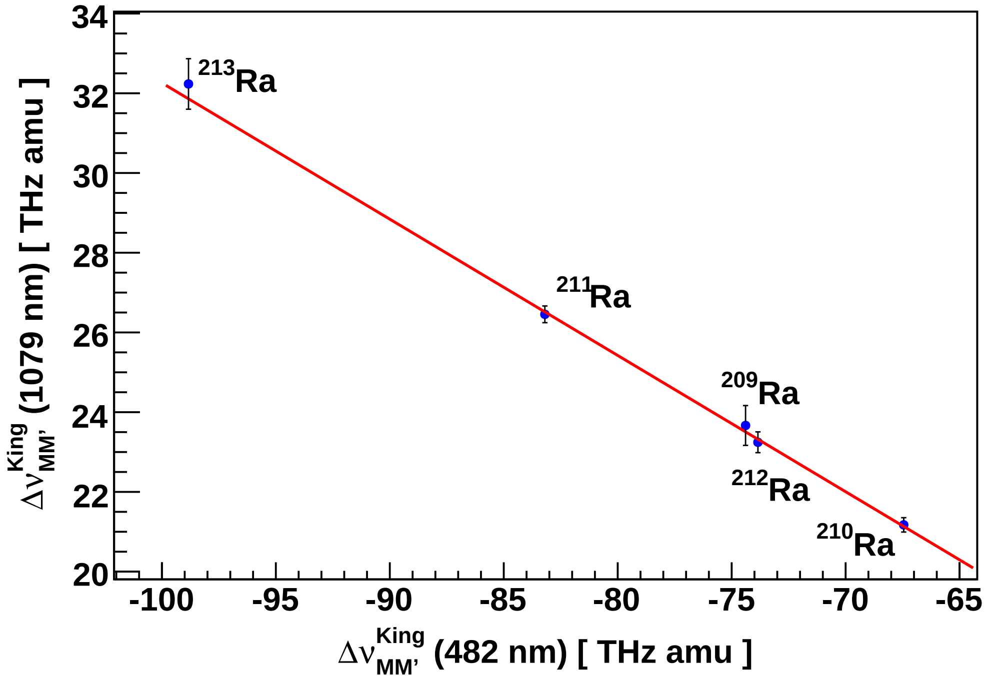

Fig. 5.9: King plot of the isotope shift of $6d\,^2D_{3/2}$ - $7p\,^2P_{1/2}$ transition at λ=1079 nm in Ra$^+$ against the corresponding shift of $7s\,^1\mathrm{S}_0$ - $7s7p\,^1\mathrm{P}_1$ transition at λ=482 nm in the Ra atom. The uncertainties at 482 nm are too small to be visible against the marker size.

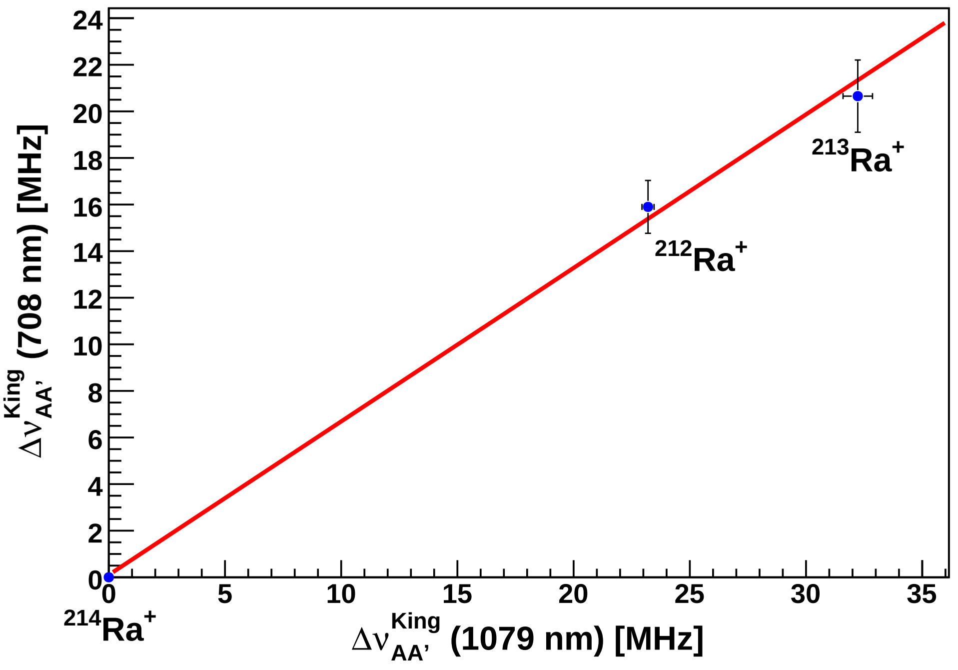

Fig. 5.10: A King plot of the isotope shift of $6d\,^2D_{3/2}$ - $7p\,^2P_{3/2}$ transition at λ=708 nm in Ra$^+$ against the corresponding shifts in λ=1079 nm line in Ra$^+$.

5.3 Lifetime of Metastable $6d\ ^2D_{5/2}$ State

The demonstrated shelving of ions from the fluorescence cycle to the $6d\ ^2D_{5/2}$ state by accessing the $6d\ ^2D_{3/2}$ - $7p\ ^2P_{3/2}$ transition as described in section 5.2.2 also enables a measurement of the lifetime of this metastable state [117]. This has been studied only in $^{212}\mathrm{Ra}^+$. The lasers at λ_1, λ_2, and λ_3 are tuned to be on resonance for the relevant transitions. The laser at λ_3 is pulsed with a mechanical chopper wheel with 170 ms on-periods and 670 ms off-periods. When the laser at λ_3 is on, the $6d\ ^2D_{5/2}$ state is populated via the $7p\ ^2P_{3/2}$ state. When the laser at λ_3 is off, the $6d\ ^2D_{5/2}$ state gets depopulated and the ions reenter the fluorescence cycle with a time constant equal to the lifetime of the $6d\ ^2D_{5/2}$ state.

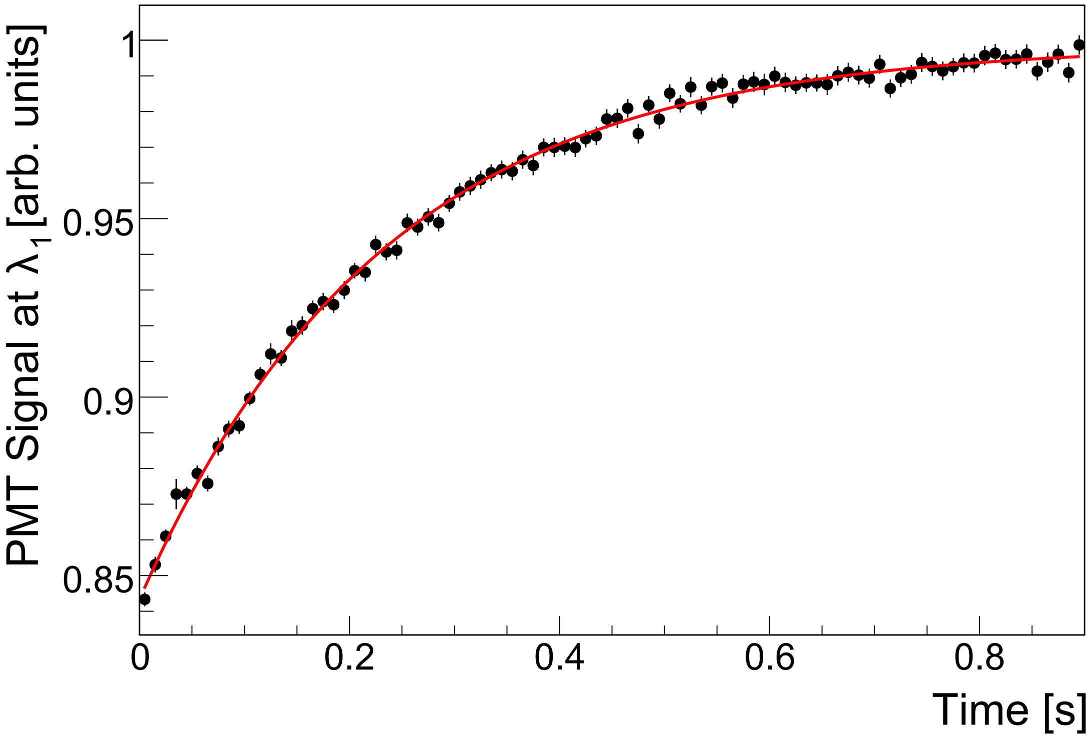

Fig. 5.11: Lifetime of $6d\ ^2D_{5/2}$ state in $^{212}\mathrm{Ra}^+$ at neon buffer gas pressure 4×10^{-5} mbar. The solid line represents a fit of an exponential function to the data.

This is shown in Fig. 5.11. However, the neon buffer gas causes a reduction of the lifetime of the metastable state by quenching it to the ground state. To estimate this effect of the buffer gas, the measurement has been carried out at different gas pressures ranging from 10^{-2} to 10^{-5} mbar and the lifetime is extrapolated to zero pressure. This is shown in Fig. 5.12. The buffer gas is found to have a

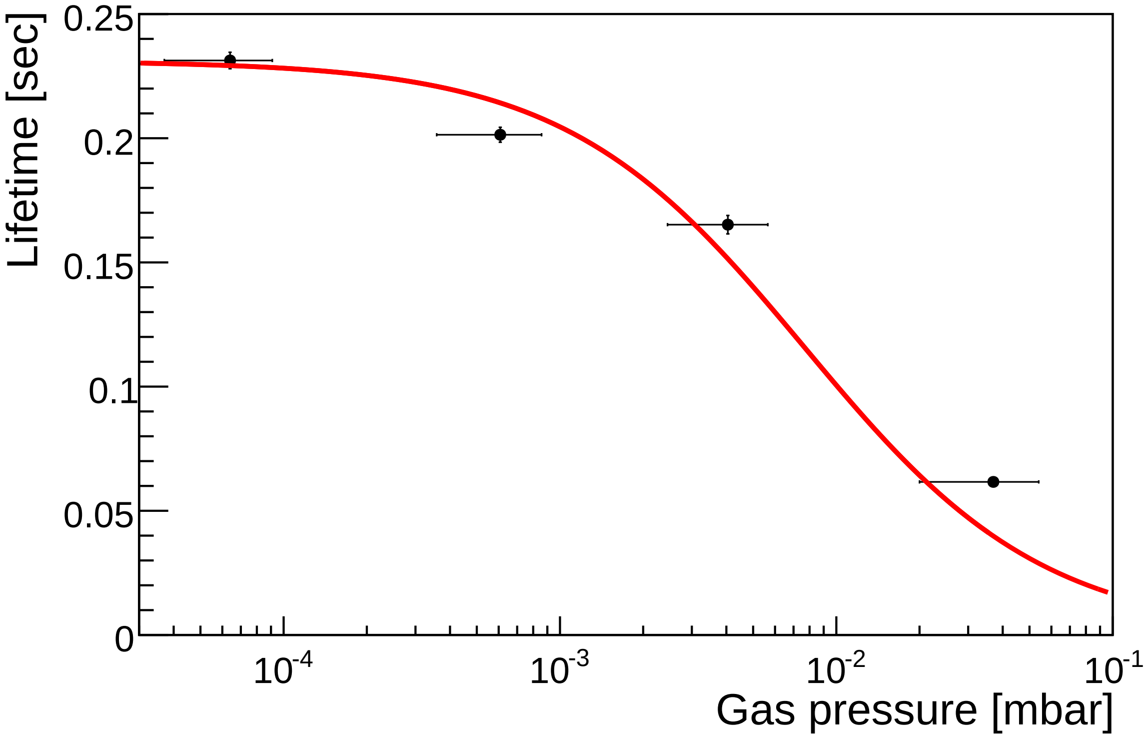

Fig. 5.12: Lifetime of $6d\ {}^2D_{5/2}$ state in ${}^{212}\mathrm{Ra}^+$ measured at different gas pressures.

strong influence on the radiative lifetime.

Since no detailed theory is currently available to explain the extrapolation to zero pressures, extrapolated radiative life time of 232(4) ms is treated as a lower bound. This number corresponds to the lifetime measured at the lowest pressure of about 4×10^{-5} mbar. The theoretical predictions of the radiative lifetime of the metastable $6d\ {}^2D_{5/2}$ state in ${}^{212}\mathrm{Ra}^+$ are 297(4) ms [75] and 303(4) ms [84]. Our experimental result confirms that the $6d\ {}^2D_{5/2}$ state is long-lived. This is an essential property in view of the long coherence times needed in a single ion APV experiment. The measured lifetimes are important probes of the E2 matrix element which is essential for the APV experiment.

5.4 Conclusion

Towards a planned measurement of parity violation in a single trapped ion an experimental set up has been developed within the TRIμP research program which enables the production and thermalization of radium isotopes. Precision spectroscopy of trapped radium ions in a linear Paul trap yields results on hyperfine

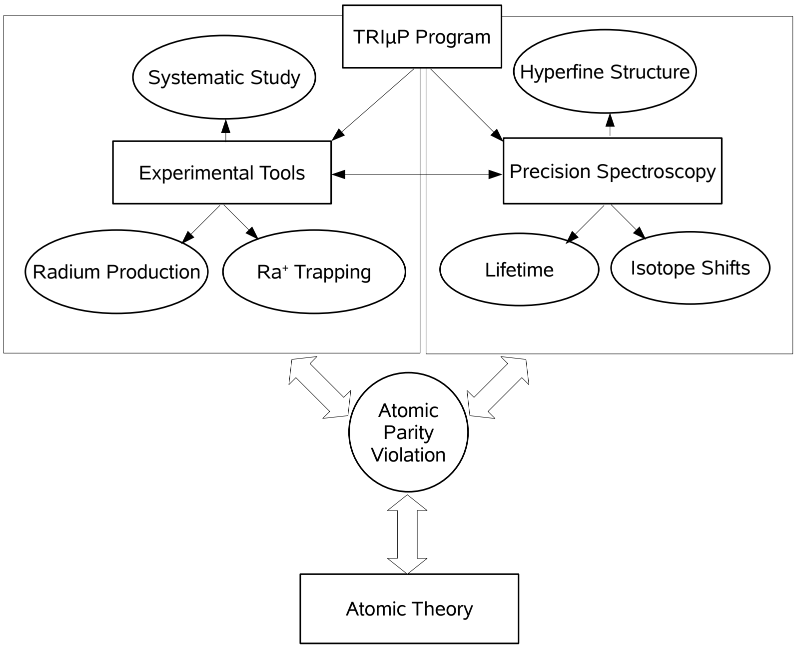

structure intervals, isotope shifts, and lifetime. They are important experimental input for improving the atomic structure calculations.

Chapter 6

Towards Single Ion Parity Violation Measurement

In this chapter the principle of measurement of a parity violating vector like AC Stark shift in the ground $7s\ ^2S_{1/2}$ state Zeeman sub-levels of a single trapped Ra^+ is described. Here the experimental method and some underlying physics are discussed. We start with an explanation on the coupling of states with some mathematical treatment for matrix elements and Rabi oscillations. The AC Stark shift is introduced thereafter which is followed by the principle of measurement of AC Stark shift using radio frequency spectroscopy. We end with a current status of the experiment in this direction.

6.1 Coupling of States

A two state coupling diagram that depicts two atomic levels $|1\rangle$ and $|2\rangle$ is shown in Fig. 6.1 where the ground state $|1\rangle$ and the excited state $|2\rangle$ are coupled by an interaction. The interaction is assumed to be near resonant with the atomic energy level splitting $\hbar\omega_0$. The resonant field that is responsible for the interaction Hamiltonian is oscillatory at $\omega_L = \omega_0 + \delta$, where δ is the detuning. For simplicity the spontaneous decay of the excited state is ignored.

An atomic Hamiltonian H_0 can be considered which includes all of the internal structures of the atom, e.g., electrostatic and fine structure energies, in order to have just two eigenstates $|1\rangle$ and $|2\rangle$ for the ground state and the excited state respectively. Using standard mathematical expressions [107,118] the Hamiltonian

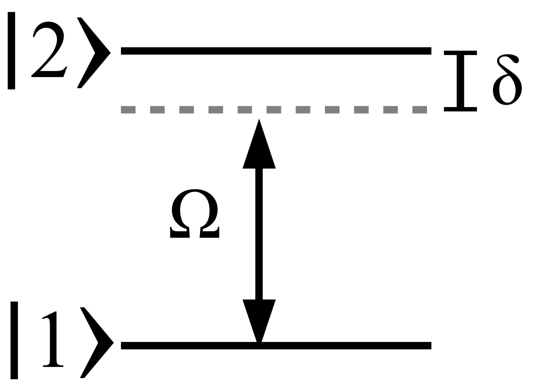

Fig. 6.1: A two level coupling diagram showing the ground state $|1\rangle$ and the excited state $|1\rangle$ which are coupled by an interaction $\Omega = \frac{1}{\hbar}\langle 1|H_{int}|2\rangle$. The interaction is assumed to be near resonant with the atomic energy level splitting $\hbar\omega_0$. The resonant field that is responsible for the interaction Hamiltonian H_{int} is oscillatory at $\omega_L = \omega_0 + \delta$, where δ is the detuning.

can be written as

$$H_0 = \hbar \sum_{i=1,2} \omega_i |i\rangle\langle i|, \tag{6.1}$$

where ω_i is the energy of the state i. The atomic Hamiltonian H_0 is perturbed by the comparatively small time varying interaction Hamiltonian H_{int} generated in the laboratory. Hence the total Hamiltonian is $H = H_0 + H_{int}(t)$.

An atomic wavefunction can be written as a linear combination of orthogonal eigenstates $\varphi_k(\vec{r})$,

$$\psi(\vec{r}, t) = \sum_{k=1,2} c_k(t)\varphi_k(\vec{r})e^{-i\omega_k t}. \tag{6.2}$$

The time dependent Schrödinger equation is applied to see how it evolves in time,

$$H\psi(\vec{r}, t) = i\hbar\frac{\partial}{\partial t}\psi(\vec{r}, t) \tag{6.3}$$

$$[H_0 + H_{int}(t)] \sum_{k=1,2} c_k(t)\varphi_k(\vec{r})e^{-i\omega_k t} = i\hbar\frac{\partial}{\partial t} \sum_{k=1,2} c_k(t)\varphi_k(\vec{r})e^{-i\omega_k t}. \tag{6.4}$$

The diagonal terms of $H_{int}(t)$ represent energy shifts and hence they can be absorbed into H_0 for now. Multiplying both sides by $\varphi_j(\vec{r})$ and integrating over $\vec{r}$ gives differential equations for the state amplitudes $c_1(t)$ and $c_2(t)$

$$i\hbar\frac{d}{dt}c_1(t) = c_2(t)\langle 1|H_{int}(t)|2\rangle e^{-i\omega_0 t} \tag{6.5}$$

$$i\hbar\frac{d}{dt}c_2(t) = c_1(t)\langle 2|H_{int}(t)|1\rangle e^{+i\omega_0 t}, \tag{6.6}$$

where the matrix elements introduced are defined as

$$\langle i|H_{int}(t)|j\rangle = \int \psi_i^*(\vec{r}) H_{int}(t)\psi_j(\vec{r}) d^3\vec{r}. \tag{6.7}$$

We now consider an interaction Hamiltonian $H_{int}(t)$ due to coherent electric field nearly resonant with this two state system

$$H_{int}(t) = -e\vec{E}(\vec{r},t)\cdot\vec{r}. \tag{6.8}$$

Here e is the electronic charge. $\vec{E}(\vec{r},t)$ is an oscillating electric field $\vec{E}\cos(\omega_L t + \vec{k}\cdot\vec{r} + \phi)$. In terms of two complex exponentials, the oscillating electric filed may be expressed as

$$\vec{E}(\vec{r},t) = \frac{\vec{E}}{2}\left[\exp\Big(+i[\omega_L t + \vec{k}\cdot\vec{r} + \phi]\Big) + \exp\Big(-i[\omega_L t + \vec{k}\cdot\vec{r} + \phi]\Big)\right]. \tag{6.9}$$

By choosing a constant phase ϕ=0, the interaction Hamiltonian becomes

$$H_{int}(t) = -\frac{e\vec{E}}{2}\left[\exp\Big(+i[\omega_L t + \vec{k}\cdot\vec{r}]\Big) + \exp\Big(-i[\omega_L t + \vec{k}\cdot\vec{r}]\Big)\right]\cdot\vec{r}. \tag{6.10}$$

Expansion of the exponential yields,

$$H_{int}(t) = -\frac{e\vec{E}}{2}\left[e^{+i\omega_L t}\Big(1 + i\vec{k}\cdot\vec{r} + \cdots\Big) + e^{-i\omega_L t}\Big(1 - i\vec{k}\cdot\vec{r} + \cdots\Big)\right]\cdot\vec{r}. \tag{6.11}$$

Since atomic dimensions ($a_0 \approx 0.5$ nm) $\ll$ wavelength of light ($\lambda \approx 500$ nm), according to the electric dipole approximation $\vec{k}\cdot\vec{r} \sim a_0/\lambda \ll 1$ and hence $\vec{k}\cdot\vec{r}$ and its higher order terms may be neglected. With this approximation $1 \pm i(\vec{k}\cdot\vec{r}) + \cdots \simeq 1$ which gives

$$H_{int}(t) = \sum_{i,j}\frac{\hbar}{2}\left(\Omega_{i,j}e^{-i\omega_L t} + \Omega_{i,j}^* e^{+i\omega_L t}\right), \tag{6.12}$$

where i and j both sum over the states $|1\rangle$ and $|2\rangle$. Ω_{ij} is called the Rabi oscillation frequency and is given by

$$\Omega_{i,j} = -\frac{e}{\hbar}\langle i|\vec{E}\cdot\vec{r}|j\rangle \tag{6.13}$$

$$= -\frac{e}{\hbar}\int \psi_i^*(\vec{r})\vec{E}\cdot\vec{r}\psi_j(\vec{r})d^3\vec{r}. \tag{6.14}$$

An extensive mathematical treatment of the physics of Rabi oscillation can be found in [45].

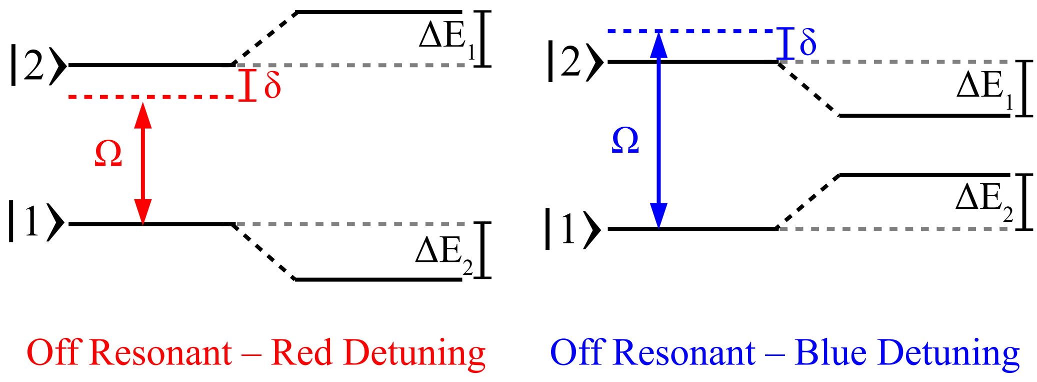

Fig. 6.2: Illustration of Stark shift on a two level system. The ground state $|1\rangle$ and the excited state $|2\rangle$ are coupled by an off-resonant laser light. The direction of energy shift is dependent on the direction of frequency detuning from the transition resonance.

6.2 The AC Stark Shift

An ion in an intense laser light field gets a light-induced polarization (atomic polarization) which interacts with the light field. The oscillating atomic polarization follows the light electric field either in phase or out of phase resulting in a decrease or increase of the energy level of a state. This shift in the energy of an atomic state is referred to as the AC Stark shift or *light shift*. Using first order perturbation theory and the mathematical treatment described in the previous section, the energy shift can be expressed as

$$\Delta E_{1,2} = \frac{\hbar}{2}(\mp\delta \pm \sqrt{\Omega^2+\delta^2}), \tag{6.15}$$

where Ω is the Rabi oscillation frequency which scales linearly with the light electric field strength and the atomic dipole matrix element $\langle 1|er|2\rangle$, and δ is the detuning of the laser frequency from the resonant frequency of the two states $|1\rangle$ and $|2\rangle$. An illustration of the AC Stark shift or light shift is shown in Fig. 6.2.

In the far off-resonance limit $|\delta| \gg \Omega$, and $\sqrt{\Omega^2+\delta^2} \simeq \delta(1+\frac{1}{2}\frac{\Omega^2}{\delta^2})$. Hence the energy sifts are

$$\Delta E_1 = \hbar\frac{\Omega^2}{4\delta} \quad \text{and} \quad \Delta E_2 = -\hbar\frac{\Omega^2}{4\delta}. \tag{6.16}$$

As depicted in Fig. 6.2, the sign of the shift depends on the detuning of the applied field from resonance. Using Ω from Eq. 6.14 and taking $\delta = E_1 - E_2 - \hbar\omega_L$, the AC Stark shift of the ground state energy can be written as

$$\Delta E_1^{Stark} = \hbar\frac{\Omega^2}{4\delta} = \frac{e^2}{4\hbar}\frac{|\langle 1|\vec{E}\cdot\vec{r}|2\rangle|^2}{(E_1 - E_2 - \hbar\omega_L)}. \tag{6.17}$$

When the laser frequency is far below the resonant frequency of the two states (red detuning), the atomic polarization follows the light electric field in phase. In this process the energy of the ground state ($|1\rangle$) is reduced. On the other hand, when the laser frequency is far above the resonant frequency (blue detuning), the atomic polarization follows the light electric field out of phase, thereby increasing the ground state energy.

6.3 A Discussion of Original Proposal

6.3.1 The Principle of Measuring the AC Stark Shift

The principle of measurement of AC stark shift or light shift is illustrated in Fig. 6.3. The physical location of a single trapped ion can be carefully engineered in such a way that it is placed at the antinode of a standing wave of laser light which is resonant with the $7s\ ^2S_{1/2}$ - $6d\ ^2D_{3/2}$ transition. The ion is simultaneously placed at the node of another standing wave of laser light in the perpendicular direction, which can be derived coherently from the same laser or from a different laser at the same frequency. At the antinode the intensity of electric field ($\vec{E'}$) is maximum whereas at the node the gradient of electric field ($\vec{E''}$) is maximum. The ion does not see the spatial electric field gradient due to $\vec{E'}$ and hence it does not drive the electric quadrupole (E2) transition between the $7s\ ^2S_{1/2}$ and $6d\ ^2D_{3/2}$ states. However it only couples the two states via a parity violating electric dipole (E1) transition. On the other hand the ion does see the spatial electric field gradient due to $\vec{E''}$. Hence it drives only the E2 transition and not the E1 transition. Let's denote the interaction Rabi frequencies of the E1 and E2 transitions as Ω' and Ω'' respectively. The two intensities can interfere with each other and add coherently to give

$$\Omega = \Omega' + \Omega''. \tag{6.18}$$

Light shifts are usually described in terms of the effective interaction [33] $\Omega^\dagger\Omega$

$$\begin{aligned}\Omega^\dagger\Omega &= (\Omega' + \Omega'')^\dagger(\Omega' + \Omega'') && (6.19)\\ &= (\Omega'^\dagger + \Omega''^\dagger)(\Omega' + \Omega'') && (6.20)\\ &= \Omega'^\dagger\Omega' + (\Omega'^\dagger\Omega'' + \Omega''^\dagger\Omega') + \Omega''^\dagger\Omega''. && (6.21)\end{aligned}$$

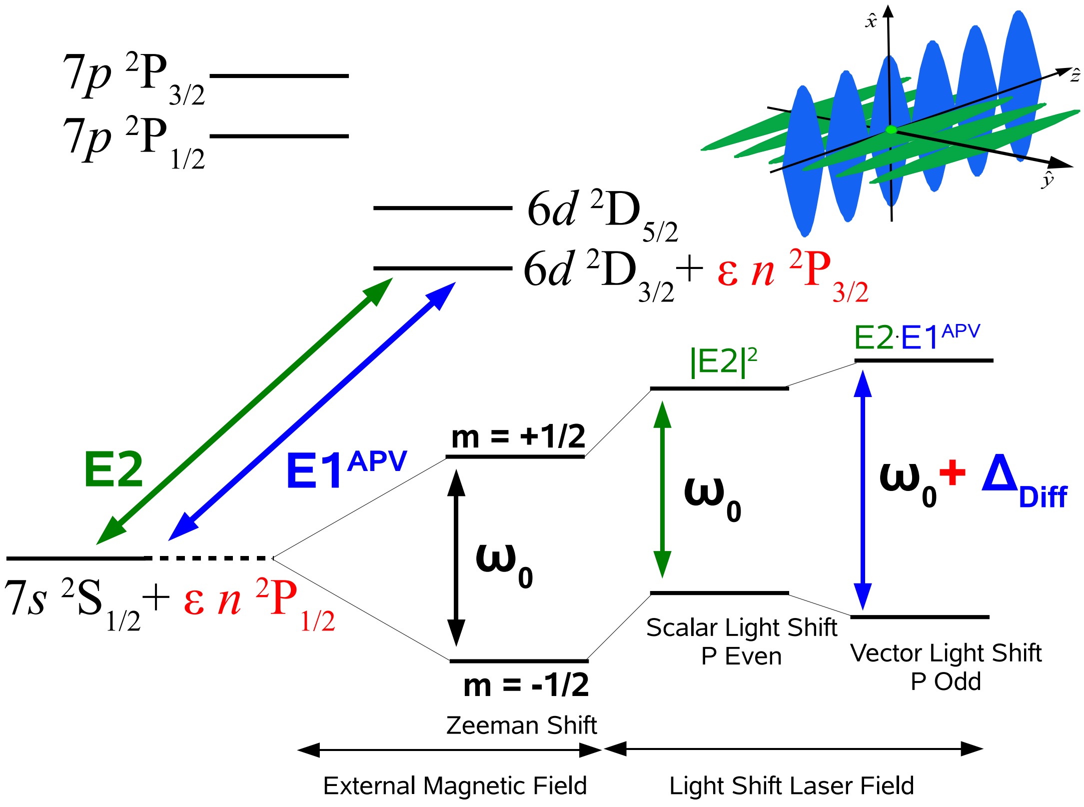

Fig. 6.3: Illustration of the measurement principle of a parity violating light shift in the $7s\ ^2S_{1/2}$ state of a single trapped Ra$^+$. The ion is placed at the antinode of a standing wave of laser light which is resonant with the $7s\ ^2S_{1/2}$ - $6d\ ^2D_{3/2}$ transition. This enables to drive the E1$^{\mathrm{APV}}$ transition. The ion is simultaneously placed at the node of an orthogonal standing wave of same frequency. This enables to drive the E2 transition.

The first term has a quadratic dependence on the very small parity violating E1 interaction. Since it is immeasurably small it may be neglected. The last term has a quadratic dependence on the very large E2 interaction. This is a purely electromagnetic term which is parity conserving. The two terms within the parentheses describe the interference between the electromagnetic and weak interactions. Neglecting the first term the experimental observable can be written as

$$\Omega^\dagger\Omega \simeq (\Omega'^\dagger\Omega'' + \Omega''^\dagger\Omega') + \Omega''^\dagger\Omega''. \tag{6.22}$$

Due to an external magnetic field the $7s\ ^2S_{1/2}$ state splits into two Zeeman sub-levels. Due to the pure electromagnetic contribution ($\Omega''^\dagger\Omega''$) each Zeeman sub-level undergoes a common energy shift. This is a scalar like AC Stark shift.

The Zeeman splitting or the Larmor precession frequency remains unchanged in this case. Due to the contribution from the interference of the weak and electromagnetic terms $(\Omega'^{\dagger}\Omega'' + \Omega''^{\dagger}\Omega')$ the Zeeman sub-levels undergo an additional shift. This is a vector like AC Stark shift. This differential shift itself is the signature of atomic parity violation.

6.3.2 Radio Frequency Spectroscopy

The differential light shift can be measured by performing radio frequency (RF) spectroscopy [119]. A block diagram of the steps involved in RF spectroscopy is shown in Fig. 6.4.

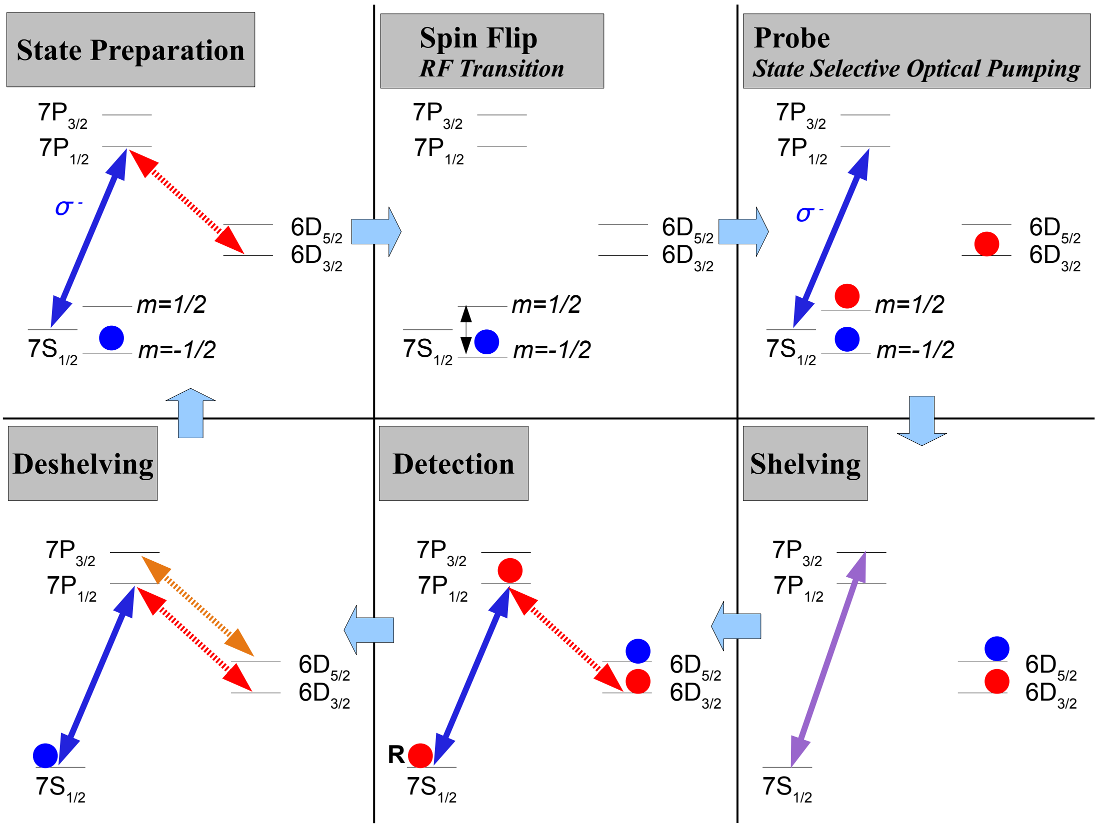

Fig. 6.4: Principle of RF Spectroscopy. The six crucial steps involved are shown. There is only one ion to be dealt with, but in some steps more than one ion is shown. This is to distinguish between the possible states where the ion can be found.

- *State preparation*: With linearly polarized cooling and repump laser beams the ion is kept in the fluorescence cycle. The ion is then prepared in a definite m state. For example, by using a σ^- polarized cooling laser beam the $m = -1/2$ state can be decoupled and after a few cycles the ion will be stuck in this state.

- *Spin flip by RF transition*: A RF transition is driven with a resonant RF pulse. A successful RF transition can change the spin state of the ion from $m = -1/2$ to $m = +1/2$.
- *Probe of spin state by optical pumping*: By applying a dim probe beam which is a σ^- polarized low intensity cooling laser beam, a state selective optical pumping is made. If a spin flip was successful in the previous step, the ion will be transferred to the $6d\ ^2D_{3/2}$ state via the $7p\ ^2P_{1/2}$ state. If a spin flip did not take place the ion is stuck at the $7s\ ^2S_{1/2}(m = -1/2)$ state.
- *Shelving*: If the ion is still stuck at the $7s\ ^2S_{1/2}(m = -1/2)$ state a shelving laser beam is used to transfer the ion to the metastable $6d\ ^2D_{5/2}$ state via the $7p\ ^2P_{3/2}$ state. Otherwise the ion will be at the metastable $6d\ ^2D_{3/2}$ state as a result of state selective optical pumping.
- *Detection*: In order to detect whether a shelving was successful or not, linearly polarized cooling and repump laser beams are turned on. If a shelving was successful no fluorescence will be detected. If shelving was not successful, the ion will be transferred from the $6d\ ^2D_{3/2}$ state to the $7p\ ^2P_{1/2}$ state and fluorescence will be detected from the $7p\ ^2P_{1/2}$ - $7s\ ^2S_{1/2}$ transition.
- *Deshelving*: If the ion was shelved, a deshelving laser beam can be used to bring the ion back to the ground $7s\ ^2S_{1/2}$ state. In addition, linearly polarized cooling and repump beams are applied to initiate the fluorescence cycle.

With the sequence of procedures described above the shelving probability is measured for a particular RF pulse. To obtain good statistical resolution the shelving probability is measured at different RF pulses and the RF resonance is mapped out at which the shelving probability drops (Fig. 6.5). The measurements are also repeated with and without the light shift laser. The difference in the resonant frequency with and without the light shift laser determines the differential light shift. The proof-of-principle of the light shift measurement in Ba^+ has been established by the research group of N. Fortson and elaborate details can be found in [33, 45].

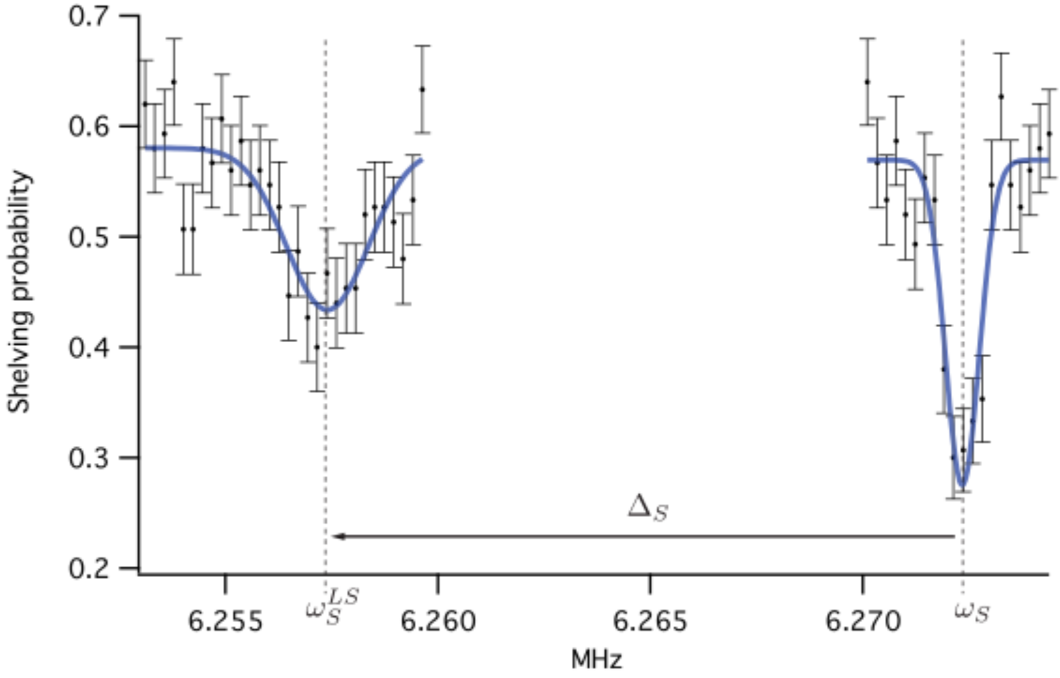

Fig. 6.5: Light shift in the $6s\ ^2S_{1/2}$ Zeeman sub-levels in Ba$^+$. The shelving probability is plotted as a function of radio frequency. ω_S is the resonant frequency without the light shift laser and ω_S^{LS} is the resonant frequency with the light shift laser. Δ_S, the difference between these two resonant frequencies, is the differential light shift. Adapted from [45].

6.4 Future Directions

A measurement of parity violation via a determination of the differential light shift is the final goal of this experiment. In order to achieve this goal we need to demonstrate and convince ourselves with our ability to trap a single radium ion in a linear Paul trap. The experimental results reported so far in this work reveal that the transitions are Doppler broadened and the line widths of the observed transition are about 500 MHz (FWHM), whereas the natural linewidths of such transitions are about 20 MHz. The parameters that are used to obtain those results are certainly optimal for an experiment in a gas-filled RFQ. But laser cooling of the trapped ions and eventually a single ion trapping require a much better experimental environment, e.g., a linear Paul trap with precise fields and absence of background gas. To realize this goal we have developed a dedicated beam line which ends with a linear Paul trap. The experimental description of this beam line has been given in section 4.2.3. The alignment of this newly

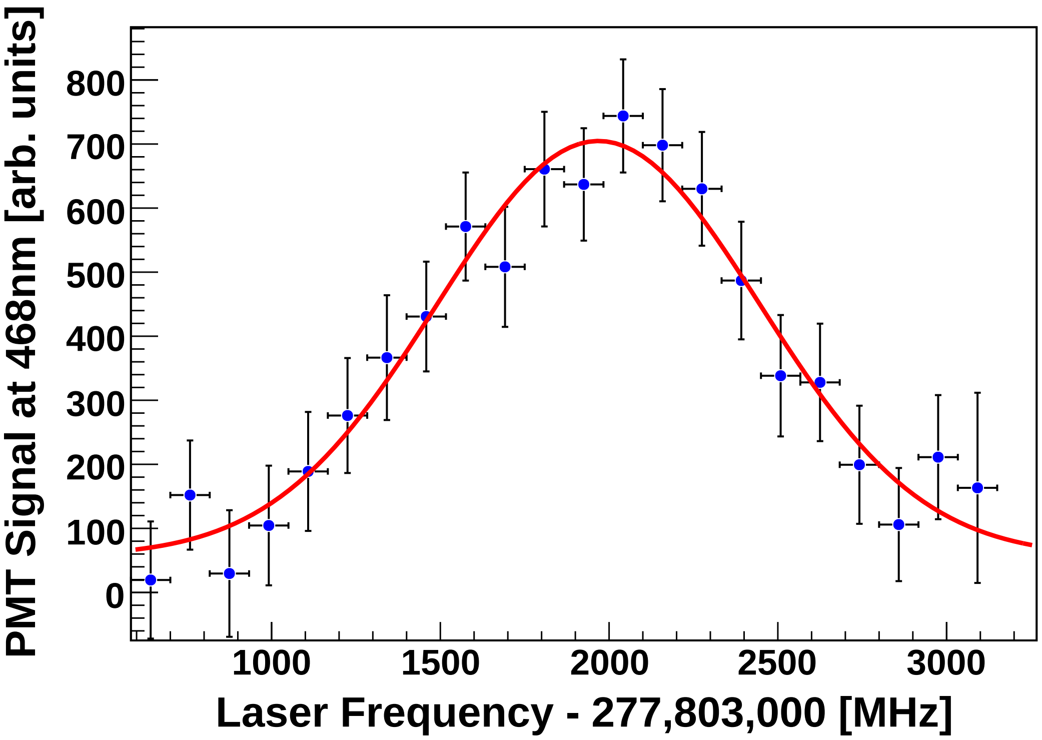

Fig. 6.6: First optical signal of trapped ^{212}Ra$^+$ in a linear Paul trap at the end of new beamline. The $6d\ ^2D_{3/2}$ - $7p\ ^2P_{1/2}$ transition is shown while the solid line represents a fit with a Gaussian function to the data.

commissioned beam line has been optimized with an optical signal of Ba$^+$ in the linear Paul trap at the end of low energy beam line (Fig. 4.15). In order to move a step further radium ions have been trapped in this trap and have been detected optically. A typical optical signal of trapped Ra$^+$ in this trap is shown in Fig. 6.6. This signal has been obtained with neon as a buffer gas. The signal size is comparatively lower than the signal sizes reported on the measurements with RFQ. This is due to losses at different parts of the low energy beam line. For example, the loss at the electrical mirror is about 50%. All such losses can be minimized by better alignment of the entire beam line.

Nevertheless a parity violation experiment requires a single ion. So the primary goal at this point of time is to laser cool a single ion. A smaller ion trap has been built to trap and laser cool a single ion. The trap is currently being tested to trap and laser cool a single barium ion. The concept and the technology will be replicated for the trapping and laser cooling of a single radium ion. A picture of the prototype of this trap is shown in Fig. 6.7.

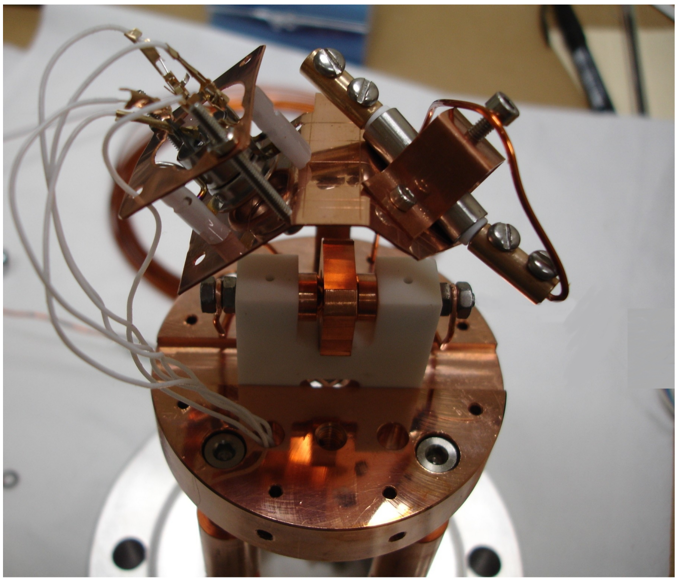

Fig. 6.7: An ion trap to confine a single ion. It can be loaded from a collector ion trap. It can also be loaded independently using a barium atomic beam and an electron beam crossing at the center of the trap.

The trap has a tip spacing of 2.5 mm and an optical access of about 1 mm. Currently the trap can be loaded with barium atoms from a barium ion source (SAES Ba dispenser ST2/FR/12 FT2 10+10). The atoms are converted to ions at the trap center using a commercial electron gun. Different systematic effects are being studied to optimize trapping conditions. Eventually this trap will be used in combination with a collector ion trap from which a few ions will be transported to this trap. Laser cooling and single ion trapping of Ba^+ is a well established technique. Hence it is only a matter of doing it. Then the technique needs to be adapted to Ra^+. It is essential to study the systematic effects and to obtain a good control over them and such studies require a lot of time. Based on the present status of the experiment and based on what needs to be done in the near future, a measurement of atomic parity violation in a trapped radium ion seems within reach. A replica of this experimental setup can be used to realize a high stability frequency standard [120].

Chapter 7

Summary of Results and Conclusion

Here we present a list of achievements and a compilation of final results achieved in the laser spectroscopy of Ra^+. This provides an indispensable ground work towards a high precision atomic parity violation experiment in this system.

- We have set up a dedicated laboratory to investigate trapping and cooling of Ba^+ which is indispensable for the work towards Ra^+. Several ion traps have been built, commissioned, and tested. Laser systems necessary for Ba^+ spectroscopy have been set up in this laboratory. Ba^+ ions have been gas cooled and trapped as a cloud. Trapping and laser cooling of a single Ba^+ ion is underway.

- A low energy beam line consisting of an electrostatic mirror, a drift tube, several lenses, several steering plates, and a linear Paul trap has been built and successfully commissioned to investigate trapping and cooling of Ra^+. Several commissioning measurement have been performed to test the integrity of this apparatus. Such measurements enable to draw conclusions about possible future upgrades in order to optimize the functionality of various parts of the apparatus.

- An independent data acquisition system has been set up for the experiment. This is an essential requirement for the online Ra^+ experiment followed by offline analysis of the experimental data.

- An isotopic chain of radium isotopes with different nuclear spins has been produced using the AGOR cyclotron and the TRIμP facility. A rotating target wheel has been developed to enhance the lifetime of the production target. The produced isotopes were thermalized and ionized to Ra$^+$ using a thermal ionizer and were extracted as a singly charged Ra$^+$ ion beam which was mass separated by a Wien filter system. The Ra$^+$ ion species were quantitatively characterized with a calibrated silicon detector. The results of radium production are listed in Table 7.1. The amount of radium ions produced are sufficient to carry out further experiments with their trapping and spectroscopy.

Table 7.1: An isotopic chain of radium isotopes was produced by shooting a $^{204/206}$Pb beam on a ^{12}C target.

Isotope	I	$T_{1/2}$ (s)	Nuclear Reaction	Beam Energy (MeV/u)	Production Rate (ions/s)
^{209}Ra$^+$	5/2	4.6(1.5)	^{204}Pb^{28+}+^{12}C	10.3	200
^{210}Ra$^+$	0	3.66(18)	^{204}Pb^{28+}+^{12}C	10.3	500
^{211}Ra$^+$	5/2	12.61(5)	^{204}Pb^{28+}+^{12}C	10.3	1000
^{212}Ra$^+$	0	12.5(1.0)	^{206}Pb^{27+}+^{12}C	8.5	800
^{213}Ra$^+$	1/2	162.0(1.7)	^{206}Pb^{27+}+^{12}C	8.5	2600
^{214}Ra$^+$	0	2.42(14)	^{206}Pb^{27+}+^{12}C	8.5	1000

- The Ra$^+$ ion beam was injected into a gas-filled radio frequency quadrupole operated in trapping mode. Transverse cooling and trapping of ions were realized here. Laser spectroscopy was performed on the trapped ion cloud which yielded new and high quality spectroscopic information on hyperfine structures, isotope shifts, and lifetime. Such results are important input to test the accuracy of atomic theory which is indispensable for the planned parity violation experiment. The results of the precision spectroscopy measurements are listed in Table 7.2 and 7.3. The relevant level schemes are displayed in Fig. 7.1 which are supplementary to the results presented.

- For laser cooling of Ra$^+$, the Ra$^+$ ion beam from thermal ionizer was transported to a linear Paul trap via the newly commissioned low energy beam line and trapping of Ra$^+$ in a buffer gas free environment was investigated.

- In conlusion, this work provides indispensable building blocks for a parity violation measurement in single trapped radium ion.

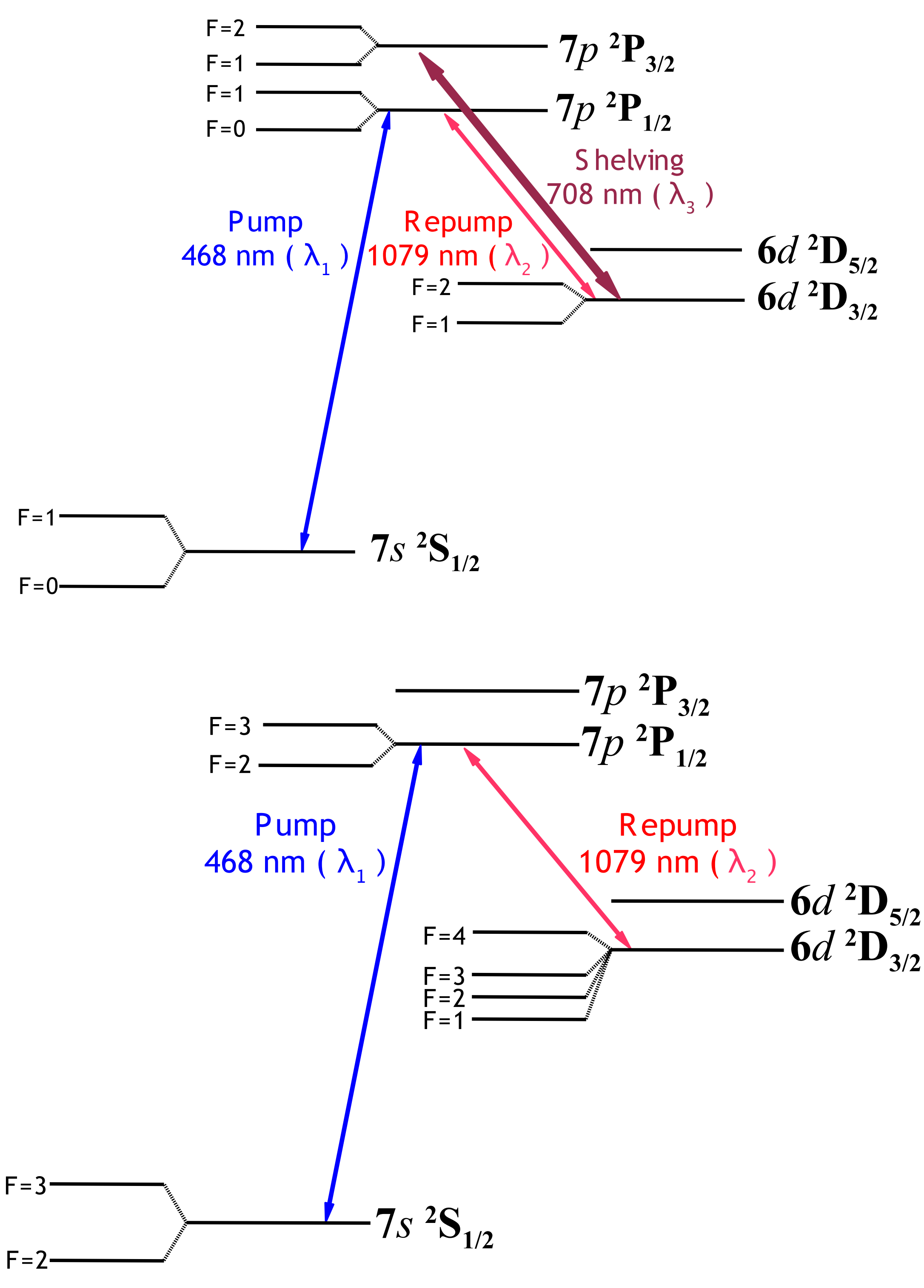

Fig. 7.1: Level schemes of odd isotopes with hyperfine structures. The upper figure corresponds to $^{213}\mathrm{Ra}^{+}$ (I=1/2) and the lower figure corresponds to $^{209,211}\mathrm{Ra}^{+}$ (I=5/2).

Table 7.2: Newly obtained results of hyperfine structure from precision laser spectroscopy of trapped radium ions. The hyperfine structure constants A and B for the odd isotopes were extracted for the $6d\ ^2D_{3/2}$ states. The measured hyperfine structure interval of the $7p\ ^2P_{1/2}$ state is in good agreement with a previous measurement [79].

Isotope	Nuclear Spin	Hyperfine Structure Constants (MHz)			Hyperfine Structure Interval (MHz)			
		$A(6d\ ^2D_{3/2})$	$B(6d\ ^2D_{3/2})$	$A(7p\ ^2P_{1/2})$	$6d\ ^2D_{3/2}$			$7p\ ^2P_{1/2}$
					F=4−F=3	F=3−F=2	F=2−F=1	F=1−F=0
^{209}Ra$^+$	5/2	148(10)	104(38)	-	673(28)	396(49)	-	-
^{211}Ra$^+$	5/2	151(2)	103(6)	-	687(9)	407(7)	-	-
^{213}Ra$^+$	1/2	528(5)	-	4542(7)	-	-	1055(10)	4542(7)

Table 7.3: Newly obtained results of isotope shift and lifetime from precision laser spectroscopy of trapped radium ions. The isotope shifts of the $6d\ ^2D_{3/2}$ - $7p\ ^2P_{1/2}$ and $6d\ ^2D_{3/2}$ - $7p\ ^2P_{3/2}$ transitions were determined with respect to ^{214}Ra$^+$. Lifetime of $6d\ ^2D_{5/2}$ state was measured only for ^{212}Ra$^+$.

Isotope	Isotope Shifts (MHz)		Absolute Frequency (MHz)		Lifetime (ms)
	$6d\ ^2D_{3/2}$ - $7p\ ^2P_{1/2}$	$6d\ ^2D_{3/2}$ - $7p\ ^2P_{3/2}$	$6d\ ^2D_{3/2}$ - $7p\ ^2P_{1/2}$	$6d\ ^2D_{3/2}$ - $7p\ ^2P_{3/2}$	$6d\ ^2D_{5/2}$
^{209}Ra$^+$	2645(56)	-	277,803,011(55)	-	-
^{210}Ra$^+$	1884(16)	-	277,803,772(11)	-	-
^{211}Ra$^+$	1755(14)	-	277,803,901(9)	-	-
^{212}Ra$^+$	1025(12)	707(50)	277,804,631(5)	423,434,288(44)	232
^{213}Ra$^+$	707(14)	453(34)	277,804,949(9)	423,434,536(25)	-
^{214}Ra$^+$	0	0	277,805,656(11)	423,434,989(23)	-

Chapter 8

Samenvatting van de Resultaten en Conclusies

Hier presenteren wij een lijst met behaalde doelstellingen en geven een compilatie van de uiteindelijke resultaten die werden behaald door middel van laserspectroscopie van Ra^+. Dit levert de onontbeerlijke basis voor de precisiemeting van atomaire pariteitschending in dit systeem.

- We hebben een laboratorium opgezet dat gewijd is aan het onderzoeken van het vangen en laserkoelen van Ba^+ ionen. Dit onderzoek is onmisbaar voor het werk aan Ra^+. Verschillende ionenvallen zijn gebouwd, getest en in gebruik genomen. De lasersystemen die nodig zijn voor het uitvoeren van spectroscopie van Ba^+ zijn opgezet in dit lab. Ba^+ ionen werden succesvol gasgekoeld en gevangen als ionenwolk. Laserkoeling van enkele Ba^+ ionen is gaande.

- Een bundellijn voor laag-energetische geladen deeltjes werd geconstrueerd. Deze bundellijn bestaat uit een elektrostatische spiegel, een "drift tube", verscheidene lenzen, verscheidene stuurplaten en een lineare Paul val. Deze onderdelen werd met succes in gebruik genomen. De bundellijn is bedoeld voor het transporteren, vangen en laserkoelen van Ra^+ ionen. Verscheidene experimenten werden uitgevoerd om het apparaat te testen. Zulke metingen stellen ons in staat om conclusies te trekken over mogelijke toekomstige verbeteringen die kunnen worden aangebracht.

- Een onafhankelijk data-acquisitiesysteem werd opgezet voor dit experiment. Dit is een vereiste om het Ra^+ experiment te kunnen monitoren, en om de experimentele data achteraf te kunnen analyseren.

- Een keten van radiumisotopen met verschillende kernspin werd geproduceerd, waarbij gebruik werd gemaakt van de deeltjesversneller AGOR en de TRIμP-faciliteit. Een roterend koolstof doelwit werd ontwikkeld om de levensduur van het productiedoelwit te verlengen. De geproduceerde isotopen werden gethermaliseerd en geïoniseerd tot Ra$^+$ gebruikmakende van een "thermal ionizer". De deeltjes werden vervolgens geëxtraheerd als een bundel van enkelvoudig geladen Ra$^+$ ionen. Deze ionenbundel werd massa-gefilterd in een Wien filter. De productie van Ra$^+$ isotopen werd kwantitatief geanalyseerd met behulp van een gekalibreerde silicium detector. De resultaten van de radiumproductie zijn samengevat in Tabel 8.1. De hoeveelheid geproduceerde isotopen is voldoende om verdere metingen uit te kunnen voeren aan de vangst en spectroscopie van radiumionen.

Table 8.1: Een keten van radiumisotopen werd geproduceerd door een $^{204/206}$Pb bundel op een ^{12}C doel te schieten.

Isotoop	I	$T_{1/2}$ (s)	Kernreactie	Bundelenergie (MeV/u)	Productietempo (ions/s)
^{209}Ra$^+$	5/2	4.6(1.5)	^{204}Pb^{28+}+^{12}C	10.3	200
^{210}Ra$^+$	0	3.66(18)	^{204}Pb^{28+}+^{12}C	10.3	500
^{211}Ra$^+$	5/2	12.61(5)	^{204}Pb^{28+}+^{12}C	10.3	1000
^{212}Ra$^+$	0	12.5(1.0)	^{206}Pb^{27+}+^{12}C	8.5	800
^{213}Ra$^+$	1/2	162.0(1.7)	^{206}Pb^{27+}+^{12}C	8.5	2600
^{214}Ra$^+$	0	2.42(14)	^{206}Pb^{27+}+^{12}C	8.5	1000

- De laag-energetische Ra$^+$ ionen-bundel werd geïnjecteerd in een gasgevulde radiofrequente quadrupool die werd gebruikt als ionenval. *Transversale vangst en koeling werd hier gerealiseerd.* Laserspectroscopie van de gevangen ionenwolk werd uitgevoerd hetgeen leidde tot data van hoge kwaliteit op het gebied van hyperfijnstructuur, isotoopverschuivingen en de levensduur van een meta-stabiele toestand. Deze resultaten leveren belangrijke gegevens op waaraan de nauwkeurigheid van de atoomtheorie, die onmisbaar is voor de geplande pariteitschendingsmeting, kan worden getoetst. De resultaten van deze precisiespectroscopie zijn samengevat in Tabel 8.2 en 8.3. De relevante energieniveaus van Ra$^+$ worden getoond in Fig. 8.1.

- Voor de laserkoeling van Ra$^+$ werd de ionenbundel van de "thermal ionizer" getransporteerd naar een lineare Paul val met behulp van de recentelijk in gebruik genomen lage-energie bundellijn. Het invangen van de deeltjes in een buffergasvrije omgeving werd getest.

- Concluderend, dit werk levert de onontbeerlijke bouwstenen voor een meting van atomaire pariteitschending in een enkel gevangen radiumion.

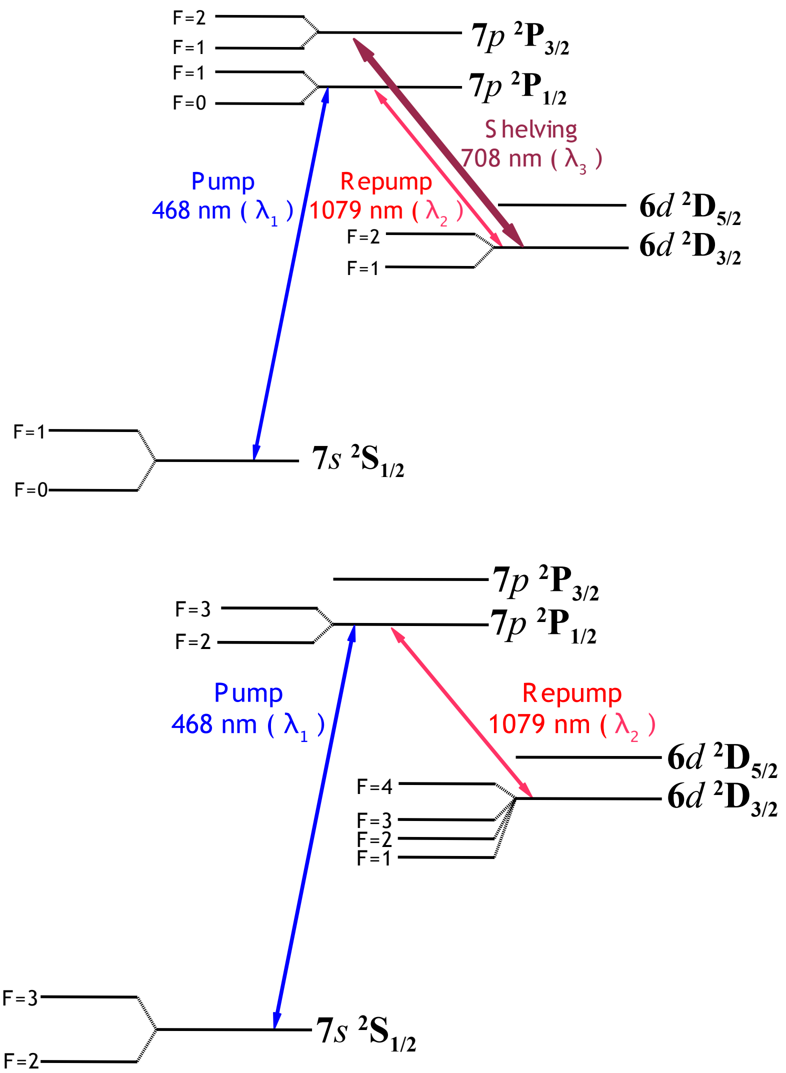

Fig. 8.1: Energieniveaus van oneven isotopen met hyperfijnstructuur. The bovenste figuur correspondeert met ^{213}Ra$^+$ (I=1/2) en de onderste figuur correspondeert met ^{209,211}Ra$^+$ (I=5/2).

Table 8.2: Nieuwe resultaten van de hyperfijnstructuur verkregen door middel van precisie laserspectroscopie van gevangen radiumionen. De hyperfijnstructuurconstanten A en B voor de oneven isotopen werden geëxtraheerd voor de $6d\ ^2D_{3/2}$ toestanden. Het gemeten hyperfijnstructuurinterval van de $7p\ ^2P_{1/2}$ toestand is in goede overeenkomst met een vorige meting [79].

Isotoop	Kernspin	Hyperfijnstructuurconstanten (MHz)			Hyperfijnstructuurinterval (MHz)			
		$A(6d\ ^2D_{3/2})$	$B(6d\ ^2D_{3/2})$	$A(7p\ ^2P_{1/2})$	$6d\ ^2D_{3/2}$			$7p\ ^2P_{1/2}$
					F=4−F=3	F=3−F=2	F=2−F=1	F=1−F=0
^{209}Ra$^+$	5/2	148(10)	104(38)	-	673(28)	396(49)	-	-
^{211}Ra$^+$	5/2	151(2)	103(6)	-	687(9)	407(7)	-	-
^{213}Ra$^+$	1/2	528(5)	-	4542(7)	-	-	1055(10)	4542(7)

Table 8.3: Nieuwe resultaten van isotoopverschuivingen en levensduur verkregen door middel van laserspectroscopie van gevangen radiumionen. De isotoopverschuivingen van de $6d\ ^2D_{3/2}$ - $7p\ ^2P_{1/2}$ en $6d\ ^2D_{3/2}$ - $7p\ ^2P_{3/2}$ overgangen werden bepaald relatief ten opzichte van ^{214}Ra$^+$. De levensduur van de $6d\ ^2D_{5/2}$ toestand werd alleen gemeten voor ^{212}Ra$^+$.

Isotoop	Isotoopverschuiving (MHz)		Absolute frequentie (MHz)		Levensduur (ms)
	$6d\ ^2D_{3/2}$ - $7p\ ^2P_{1/2}$	$6d\ ^2D_{3/2}$ - $7p\ ^2P_{3/2}$	$6d\ ^2D_{3/2}$ - $7p\ ^2P_{1/2}$	$6d\ ^2D_{3/2}$ - $7p\ ^2P_{3/2}$	$6d\ ^2D_{5/2}$
^{209}Ra$^+$	2645(56)	-	277,803,011(55)	-	-
^{210}Ra$^+$	1884(16)	-	277,803,772(11)	-	-
^{211}Ra$^+$	1755(14)	-	277,803,901(9)	-	-
^{212}Ra$^+$	1025(12)	707(50)	277,804,631(5)	423,434,288(44)	232
^{213}Ra$^+$	707(14)	453(34)	277,804,949(9)	423,434,536(25)	-
^{214}Ra$^+$	0	0	277,805,656(11)	423,434,989(23)	-

Appendix A

Discussion of Ion Trapping

In this section the basic principles of trapping ions are discussed. Elaborate treatment of these principles and related techniques can be found in [121, 122].

Earnshaw's theorem states that: *A charge acted on by electrostatic forces can not rest in stable equilibrium in an electric field.* It implies that it is not possible to generate a minimum of the electrostatic potential in free space. Hence it is not possible to confine an ion using a purely electrostatic field. However it is possible to circumvent Earnshaw's theorem by superimposing a magnetic field to create a *Penning trap* or by superimposing a time varying electric field to create a *Paul trap*. We will discuss the Paul traps and the underlying physics [107, 123]. Discussion of Penning traps can be found in [124].

A.1 Paul Trap

The principle of confining ions in a Paul trap can be understood using a simple mechanical analogue, a ball moving on a saddle-shaped surface which is shown in Fig. A.1. Rotation of the saddle-shaped surface, at a suitable speed about a vertical axis, can prevent the ball rolling off the sides of the saddle and gives stable confinement. The gravitational potential energy of a ball on a saddle-shaped surface has the same form as the potential energy of an ion close to a saddle point of the electrostatic potential in a Paul trap.

Confinement of charged particles requires a potential minimum at some point in space in order that the corresponding force is directed toward that point in all three dimensions. In general, the dependence of the magnitude of this force on the coordinates can have any arbitrary form. However, it is convenient to have a binding force that is harmonic, since it can simplify the analytical description of

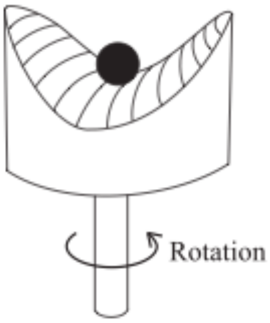

Fig. A.1: Mechanical model of dynamic stability. A rotating saddle shaped surface provides dynamic stability to a ball on this surface.

particle motion.

Particles are elastically bound to an axis or a coordinate system in space if a binding force acts on them which increases linearly with their distance r, for which we have

$$F \propto -r. \tag{A.1}$$

If $U = Q\Phi$ is the potential energy, then it follows from $F = -\nabla U$ that, the potential Φ is a quadratic function in cartesian coordinates

$$\Phi = \frac{\varphi}{2{r_0}^2}(\alpha x^2 + \beta y^2 + \gamma z^2). \tag{A.2}$$

The potential has to satisfy Laplace's equation in free space ($\nabla^2\Phi$=0). $\nabla^2\Phi$=0 imposes the condition $\alpha + \beta + \gamma$=0. There are two simple ways to satisfy this condition. $\alpha = 1 = -\beta$, γ=0 results in a two-dimensional field whereas $\alpha = \gamma = 1$, $\beta = -2$ results in a three-dimensional configuration,

$$\Phi = \frac{\varphi}{2{r_0}^2}(x^2 - y^2) \qquad \text{for } \alpha\text{=1=-}\beta,\ \gamma\text{=0} \tag{A.3}$$

$$= \frac{\varphi}{2{r_0}^2}(x^2 + y^2 - 2z^2) \qquad \text{for } \alpha\text{=}\beta\text{=1},\ \gamma\text{=-2.} \tag{A.4}$$

Trapping of Particles in a Two Dimensional Quadrupole Trap

A two dimensional configuration as in Eq. A.3 can be generated by four hyperbolically shaped electrodes linearly extended in the z-direction as shown in the Fig. A.2.

The filed strength is given by the field equations

$$E_x = -\frac{\varphi_0}{{r_0}^2}x, \quad E_y = \frac{\varphi_0}{{r_0}^2}y, \quad E_z = 0. \tag{A.5}$$

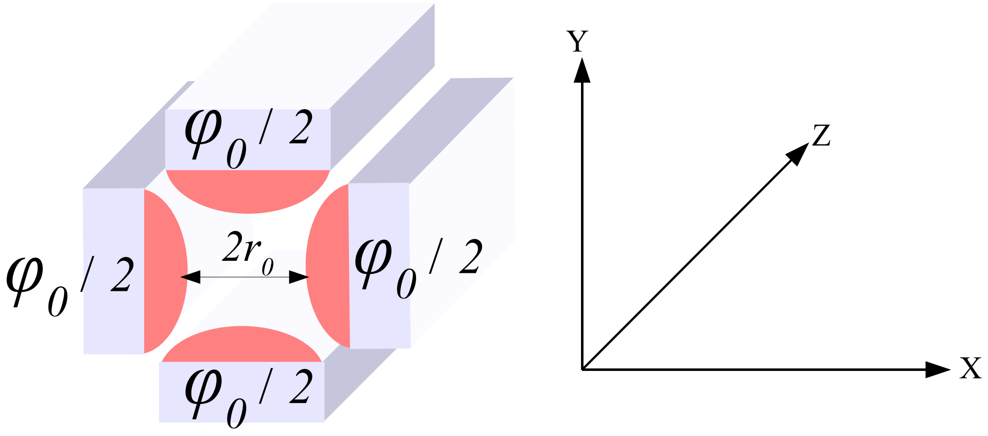

Fig. A.2: Electrode structure for a two dimensional quadrupole trap

If ions are injected along the z-direction, the electric field equations (A.5) suggest that the ions will perform harmonic oscillations in the x-z plane. However, the amplitude of oscillation in the y-direction will increase due to the opposite sign of the field E_y. This will create instability and as a result the ions will hit the electrodes and hence will be lost from the trap. Such a situation can easily be avoided by applying an additional voltage (φ_0) that is alternating in time. φ_0 can be made periodic with a DC voltage U and an RF voltage V with driving frequency ω

$$\varphi_0 = U + V\cos\omega t. \tag{A.6}$$

If the voltage φ_0 is applied between the electrode pairs then the potential on the electrodes is $\pm\varphi_0/2$. The non-relativistic motion of a charged particle in an electric filed is described by

$$\vec{F} = Q\vec{E}. \tag{A.7}$$

The equation of motion of the charged particle is written as

$$\ddot{r} = \frac{Q}{m}\vec{E}. \tag{A.8}$$

The equations of motion in x and y direction are given by

$$\ddot{x} = \frac{Q}{m}E_x = \frac{Q}{m}\left(-\frac{\varphi_0}{{r_0}^2}x\right), \qquad \ddot{y} = \frac{Q}{m}E_y = \frac{Q}{m}\left(\frac{\varphi_0}{{r_0}^2}y\right). \tag{A.9}$$

These equations may be rewritten in a more conventional way as

$$\frac{d^2x}{dt^2} + \frac{Q}{m{r_0}^2}\left(U + V\cos\omega t\right)x = 0 \tag{A.10}$$

$$\frac{d^2y}{dt^2} - \frac{Q}{m{r_0}^2}\left(U + V\cos\omega t\right)y = 0. \tag{A.11}$$

The differential equations A.10 and A.11 are knows as *Mathieu equations.* With some simple mathematical manipulation, the Mathieu equations can be written using dimensionless parameters a, q and τ. With τ=ωt/2 and $\frac{d^2}{dt^2} \equiv \frac{\omega^2}{2}\frac{d^2}{d\tau^2}$, the Mathieu equations can be written as

$$\frac{d^2x}{d\tau^2} + (a + 2q\cos 2\tau)x = 0 \tag{A.12}$$

$$\frac{d^2y}{d\tau^2} - (a + 2q\cos 2\tau)y = 0, \tag{A.13}$$

where the dimensionless parameters a, q and τ are given by

$$a = \frac{4QU}{m{r_0}^2\omega^2}, \quad q = \frac{2QV}{m{r_0}^2\omega^2}, \quad \tau = \frac{\omega t}{2}. \tag{A.14}$$

These dimensionless parameters are called Mathieu parameters. As expressed in Eq. A.14, the Mathieu parameters a and q depend on the DC voltage U and the RF voltage V respectively. Both parameters also depend on the charge-to-mass ratio Q/m of the ion and quadratically on the distance $2r_0$ between opposite rods and the oscillation frequency ω.

A.2 Stability of Ions in a Trap

The Mathieu equations have both stable and unstable solutions. In case of stable situation, the ions oscillate in the xy-plane with limited amplitude and they can travel through the quadrupole field along the z-direction without hitting the electrodes. In case of unstable solution, the amplitude of oscillation in the x, y, or both directions grows and the ions will be lost. The stability of the ions in the trap depends only on the Mathieu parameters a and q, and not on the initial parameters of the ion motion, Hence it is important to know the zones of stability in the a-q map, also know as *Mathieu stability diagram.*

The trapped ions are stable in all regions of Mathieu stability diagram where x-stable and y-stable portions overlap. As shown in Fig. A.3, there exist several regions of stability in the Mathieu stability diagram at high value of a and q. But the most used stability region is defined by $q < 0.91$ and small a. For fixed values of r_0, ω, U, and V, all ions with the same charge-to-mass ratio Q/m have the same operating point in the Mathieu stability diagram. Since a/q is equal to $2U/V$ and is independent of the mass m, all masses lie along the operating line a/q=constant (Fig. A.4).

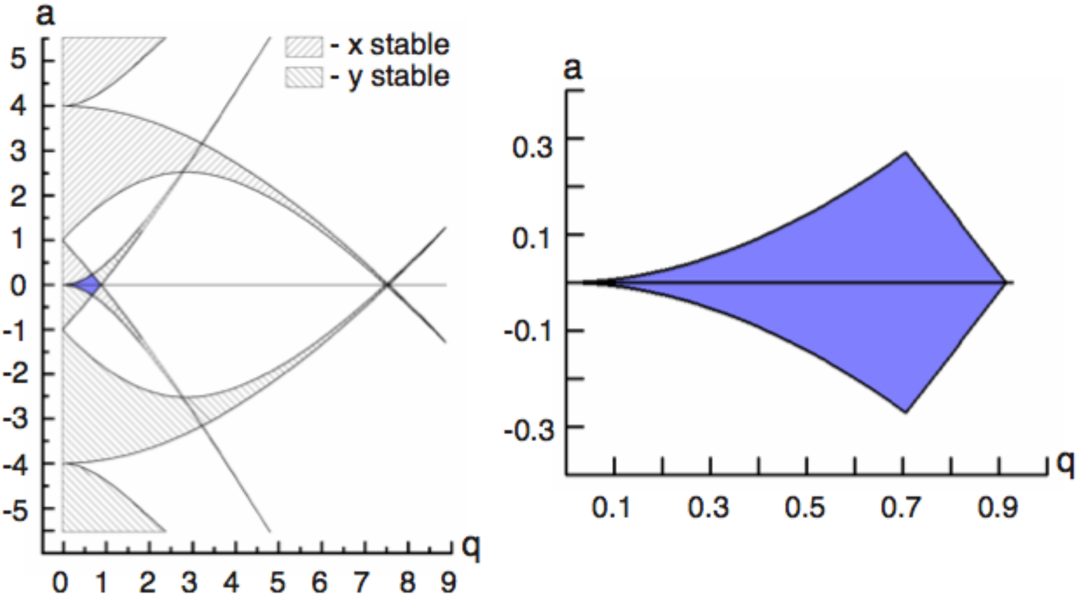

Fig. A.3: Mathieu stability diagrams in a two dimensional quadrupole trap. The right figure indicates the zone of stability. Adapted from [19].

Radial confinement of ions in a linear Paul trap relies on the inhomogeneity of electric fields between the electrodes. Only in a homogenous field the time-dependent term of the force cancels out in the time average. But in a quadrupole field, which is a periodic inhomogeneous field, there is a small average force left pointing toward the center of the trap which enables the ions to traverse the quadrupole field without hitting the electrodes. Hence the motion of the ions around the z axis can be stable with limited amplitude in x and y directions. In a quadrupole field the potential at the geometrical center between the electrodes is zero and it increases with the distance from center according to Eq. A.3. This field inhomogeneity leads to a small average force in the direction towards the low field regions (closer to the center of trap), resulting in a *pseudo potential well* for the ions [125]. With r as the distance from the trap axis the pseudo potential $\Phi_{PS}(r)$ for the ions confined by the RF field ($V \cos \omega t$) is given by

$$\Phi_{PS}(r) = \frac{qV}{4r_0^2} r^2. \tag{A.15}$$

A.3 Macromotion and Micromotion

The stable motion of ions in the RF quadrupole field can be decomposed into two separate oscillatory motions, the micromotion and the macromotion. The micromotion is caused directly by the electric field oscillations. Thus, it has the same frequency ω as that of RF, except it is out of phase with the field by π. It also follows the strength of the electric field. The macromotion or secular motion is associated with the pseudo potential and it has a lower frequency (ω_{macro}) which is related to the RF frequency (ω) as

$$\omega_{macro} = \frac{q}{2\sqrt{2}}\omega. \tag{A.16}$$

Trapping of Particles in a Three Dimensional Quadrupole Trap

Trapping of particles in a three dimensional quadrupole field is very similar to the two dimensional case as discussed before. A three dimensional configuration as in Eq. A.4. can be generated in many different ways, e.g., with a hyperbolically shaped ring electrode and two hyperbolic rotationally symmetric caps. The field equations in the three dimensional case are given by

$$E_x = \frac{\varphi_0}{{r_0}^2}x, \quad E_y = \frac{\varphi_0}{{r_0}^2}y, \quad E_z = -2\frac{\varphi_0}{{r_0}^2}z. \tag{A.17}$$

Using similar mathematical treatment as shown in the two dimensional case, one can arrive at the conclusion that the equations of motions of the ions in a three dimensional quadrupole trap can be represented by similar Mathieu equations

$$\frac{d^2x}{d\tau^2} - (a + 2q\cos 2\tau)x = 0 \tag{A.18}$$

$$\frac{d^2y}{d\tau^2} - (a + 2q\cos 2\tau)y = 0 \tag{A.19}$$

$$\frac{d^2z}{d\tau^2} + (a + 2q\cos 2\tau)z = 0, \tag{A.20}$$

where the dimensionless parameters a, q and τ are given by

$$a_x = a_y = 2a_z = \frac{4QU}{m{r_0}^2\omega^2} \tag{A.21}$$

$$q_x = q_y = 2q_z = \frac{2QV}{m{r_0}^2\omega^2} \tag{A.22}$$

$$\tau = \frac{\omega t}{2}. \tag{A.23}$$

Accordingly the region of stability in the a-q map for a three dimensional trap has a different shape, as shown in Fig. A.4. Similar to the two dimensional counterpart, the motion of ions in a three dimensional quadrupole trap is described as a slow secular motion modulated with a micromotion. The pseudo potential [125]

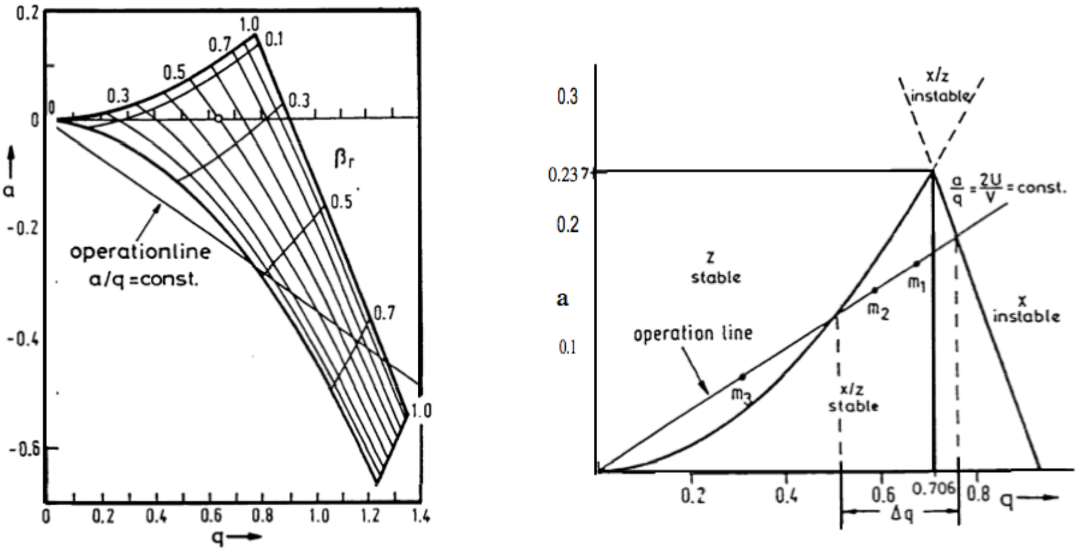

Fig. A.4: Mathieu stability diagram in a quadrupole trap for two dimensional (right) and three dimensional (left) case . Adapted from [123].

in a three dimensional quadrupole field is given by

$$\Phi_{PS} = D\frac{x^2 + y^2 + 4z^2}{r_0^2 + 2z_0^2}, \tag{A.24}$$

where, D is the potential depth. Both in two and three dimensional quadrupole traps the radio frequency voltage amounts to be a few hundred volts and potential depth is of the order of 10 volts. The width of the potential well is defined by the geometrical dimension of the trap.

Appendix B

Discussion of Hyperfine Structure

B.1 Hyperfine Structure Interval

The term hyperfine structure refers to a structure in atomic spectra which results from the existence of spins and electromagnetic multipole moments of atomic nuclei. The interactions of these nuclear moments with the electrons lead to an additional splitting of the spectral lines which is knows as the hyperfine structure.

B.2 Spins and Electromagnetic Multipole Moments

If the nucleus has a nonzero nuclear spin I, then it is said to possess a nuclear angular momentum $\vec{I}$, where

$$|\vec{I}| = \sqrt{I(I+1)}\hbar. \tag{B.1}$$

The quantum number I may be integral or half integral[1]. Similar to electronic angular momentum, the nuclear angular momentum is observable along the quantization axis, e.g., in the z-direction where an applied magnetic field is oriented. The x and y components have time averages equal to zero and hence are not observable. For the z-component $(\vec{I})_z$=$m_I\hbar$ with m_I=*I, I-1, ..., 0, ..., -I+1, I.* Thus there are $2I$+1 possible orientations of nuclear angular moment relative to

---

[1] Stable atomic nuclei are known with $0 < I < 15/2$.

the quantization axis, corresponding to the possible values of nuclear magnetic quantum number m_I.

B.3 The Hyperfine Interaction

In addition to spin a nucleus has also electromagnetic multipole moments. The interactions between those moments and the electromagnetic field produced by the electrons at the nucleus are responsible for the hyperfine structure.

By arguments of parity and time-reversal symmetry the only non-vanishing multipole (2^k-pole) moments, apart from the electric charge for k=0, are the magnetic moments for odd k and the electric moments for even k. Interactions of the higher order multipole moments ($k \geq 3$) with the electrons are negligibly small. Hence the two lowest orders of interaction, i.e., the magnetic dipole interaction and the electric quadrupole interaction are of physical importance with regard to hyperfine structure.

B.3.1 Magnetic Dipole Interaction

Magnetic dipole interaction is the interaction of a point nuclear magnetic moment $\vec{\mu}_I$ with the magnetic field $\vec{B}_J$ produced by the electrons at the nucleus. The nuclear magnetic moment $\vec{\mu}_I$ is connected with nuclear angular momentum $\vec{I}$ as

$$\vec{\mu}_I = \gamma \vec{I} = \frac{g_I \mu_N}{\hbar} \vec{I}, \tag{B.2}$$

where γ is the *gyromagnetic ratio.* g_I is the nuclear g-factor. $\mu_N = e\hbar/2m_p$ is the unit of nuclear magnetic moment (nuclear magneton) which is analogous to the Bohr magneton $\mu_B = e\hbar/2m_e$.
Following the quantization rules for the angular momentum

$$(\vec{\mu}_I)_z = \frac{g_I \mu_N}{\hbar} (\vec{I})_z = g_I \mu_N m_I. \tag{B.3}$$

The Hamiltonian for the magnetic dipole interaction is given by

$$H_D = -\vec{\mu}_I \cdot \vec{B}_J. \tag{B.4}$$

This is to be treated as a small perturbation. $\vec{\mu}_I$ depends on nuclear coordinates only and $\vec{B}_J$ depends on electronic coordinates only. With an adoption of IJ coupling approximation, one can write $\vec{B}_J \propto \vec{J}$, as $\vec{B}_J$ operates in the space of electronic coordinates only. Hence Eq. B.4 can take the form

$$H_D = A \vec{I} \cdot \vec{J}, \tag{B.5}$$

where A is the *hyperfine structure constant*, an experimentally measurable quantity. According to IJ coupling approximation

$$\vec{F} = \vec{I} + \vec{J} \tag{B.6}$$

$$\vec{F}^2 = (\vec{I} + \vec{J})^2 = \vec{I}^2 + \vec{J}^2 + 2\vec{I}.\vec{J} \tag{B.7}$$

$$\vec{I}.\vec{J} = \frac{1}{2}\left[\vec{F}^2 - \vec{I}^2 - \vec{J}^2\right]. \tag{B.8}$$

To first order[2], the energy shift of a level J is given by the expectation value of the interaction Hamiltonian (for magnetic dipole interaction) of Eq. B.5

$$\Delta E_D = \langle IJFm_F|H_D|IJFm_F\rangle \tag{B.9}$$

$$= \langle IJFm_F|A\vec{I}\cdot\vec{J}|IJFm_F\rangle \tag{B.10}$$

$$= \frac{A}{2}\left[F(F+1) - J(J+1) - I(I+1)\right]. \tag{B.11}$$

In summary, a level with well-defined total angular momentum J splits into hyperfine states, labelled by F, which are $(2F+1)$-fold degenerate. The hyperfine structure constant A is a measure of the splitting and there is an interval rule,

$$\Delta E_F - \Delta E_{F-1} = AF. \tag{B.12}$$

F has $2I$+1 values for $I<J$ or $2J$+1 values for $J \leq I$. The electric dipole selection rule for F is ΔF=0,±1 while F=0 → F=0 is forbidden.

B.3.2 Electric Quadrupole Interaction

Electric quadrupole interaction is the interaction between the nuclear electric quadrupole moment and the electric field of electrons. The nuclear electric quadrupole moment depends on the nuclear charge distribution. For nucleus with $I > 1/2$, the quadrupole moment is non-zero. It is positive for prolate[3] and negative for oblate[4] charge distribution.

The quadrupole interaction causes a shift of the hyperfine levels. In first order, the energy shift is

$$\Delta E_Q = \langle IJFm_F|H_Q|IJFm_F\rangle \tag{B.13}$$

$$= \frac{B}{4}\left[\frac{\frac{3}{2}K(K+1) - 2I(I+1)J(J+1)}{I(2I-1)J(2J-1)}\right], \tag{B.14}$$

---

[2] Consideration of configuration mixing and relativistic effects, though important in hyperfine structure, is beyond the scope of this thesis.

[3] Cigar-shaped charge distribution, elongated along the direction of I.

[4] Pin-cushioned shaped charge distribution, flattened perpendicular to I.

where $K = [F(F+1) - J(J+1) - I(I+1)]$. B is another hyperfine structure constant. The quadrupole interaction vanishes for S terms because of spherically symmetric electron charge distribution. The quadrupole interaction also vanishes unless $I \geq 1,\ J \geq 1$.

Combining the magnetic dipole and electric quadrupole shifts from Eq. B.11 and Eq. B.14, the hyperfine structure interval can be written as

$$\Delta E_{HFS} = \frac{A}{2}K + \frac{B}{4}\left[\frac{\frac{3}{2}K(K+1) - 2I(I+1)J(J+1)}{I(2I-1)J(2J-1)}\right]. \tag{B.15}$$

This shows that the electric quadrupole interaction gives rise to a departure from the interval rule, because its dependence on F is different from that of magnetic dipole interaction. When B/A is sufficiently large the order of F-levels may even be different from that when B/A=0.

Appendix C

Discussion of Isotope Shift

C.1 Isotope Shift

Bohr's model predicts that for a transition between energy levels with principal quantum numbers n_1 and n_2, an atom emits light with a wave number given by

$$\tilde{\nu}_\infty = R_\infty \left(\frac{1}{n_1^2} - \frac{1}{n_2^2} \right), \tag{C.1}$$

where R_∞ is the Rydberg constant. The subscript ∞ indicates that the nucleus is assumed to be infinitely massive.
But the spectral lines in hydrogen obey the mathematical formula

$$\tilde{\nu} = R_H \left(\frac{1}{n_1^2} - \frac{1}{n_2^2} \right). \tag{C.2}$$

There is a subtle difference between R_∞ and R_H. In reality, the electron and the nucleus move around the center of mass of the system. Mathematically R_∞ can be expressed as

$$hcR_\infty = \frac{(e^2/4\pi\varepsilon_0)^2 m_e}{2\hbar^2}. \tag{C.3}$$

For a hydrogen nucleus of finite mass m_p,

$$hcR_H = \frac{(e^2/4\pi\varepsilon_0)^2 m}{2\hbar^2}, \tag{C.4}$$

where m is the reduced mass of the electron, $\frac{m_e m_p}{m_e + m_p}$.
Now it is evident that

$$R_H = R_\infty \frac{m_p}{m_e + m_p}. \tag{C.5}$$

This reduced mass correction is not the same for different isotopes of a particular element, e.g., hydrogen and deuterium. This leads to a measurable difference in the frequency of a spectral line for two different isotopes. This is called *isotope shift*. For many-electron atoms the nuclear properties that contribute towards isotope shifts are the finite mass (*mass effect*) and the extended charge distribution of the nucleus (*field effect*).

C.2 Mass Effect

The mass effect may be treated by considering the kinetic energy operator in Schrödinger's equation

$$T = \frac{\vec{P}_N^2}{2M_N} + \sum_i \frac{\vec{p}_i^2}{2m_e}, \tag{C.6}$$

where P_N and M_N are the momentum and mass of the nucleus, while p_i and m_e are the momentum and mass of the i^{th} electron. By following the principle of conservation of momentum for a stationary atom,

$$\vec{P}_N = -\sum_i \vec{p}_i. \tag{C.7}$$

Hence,

$$T = \frac{(\sum_i p_i)^2}{2M_N} + \frac{\sum_i p_i^2}{2m_e} \tag{C.8}$$

$$= \frac{\sum_i p_i^2}{2M_N} + \frac{1}{M_N}\sum_{i>j} p_i \cdot p_j + \frac{\sum_i p_i^2}{2m_e}. \tag{C.9}$$

The second term in Eq. C.9, which contains the dot product of electron momenta, can be ignored for single electron systems, e.g., hydrogen and deuterium. The remaining two terms can be combined with the introduction of the reduced mass $m = \frac{m_e m_p}{m_e + m_p}$. Thus an energy level $E(M_N)$ for an atom whose nucleus has a finite mass M_N is raised above the fictitious level (E_∞) for a 'theoretical' atom whose nucleus is infinitely heavy. This can be expressed as

$$E(M_N) = E_\infty \frac{M_N}{m_e + M_N}. \tag{C.10}$$

In terms of wavenumber

$$\tilde{\nu} = \tilde{\nu}_\infty \frac{M_N}{m_e + M_N} \tag{C.11}$$

$$\simeq \tilde{\nu}_\infty \left(1 - \frac{m_e}{M_N}\right). \tag{C.12}$$

However, $\tilde{\nu}_\infty$ can not be measured and only the difference in wave numbers between two isotopes of an element can be observed. Considering two isotopes with nuclear masses $M_N^{'}$ and $M_N^{''}$, the wavenumber shift for the observed spectral line is

$$\begin{aligned}
\Delta\tilde{\nu}_{mass} &= \nu_{M_N^{''}} - \nu_{M_N^{'}} && \text{(C.13)}\\
&\simeq \tilde{\nu}_\infty \left[\left(1 - \frac{m_e}{M_N^{''}}\right) - \left(1 - \frac{m_e}{M_N^{'}}\right)\right] && \text{(C.14)}\\
&\simeq \tilde{\nu}_\infty m_e \left(\frac{M_N^{''} - M_N^{'}}{M_N^{''} M_N^{'}}\right) && \text{(C.15)}\\
&\simeq \frac{m_e \delta M_N}{M_N^{'} - M_N^{''}} \tilde{\nu}_\infty, && \text{(C.16)}
\end{aligned}$$

where the isotope of greater mass has the larger wavenumber. This phenomenon is known as *normal mass shift*. This shift is the largest for hydrogen-deuterium. Since the mass shift is proportional to $\frac{1}{M^2}$, the mass effect is small for heavy elements.

For multi-electron systems, the cross term in Eq. C.9 can not be neglected and it leads to an additional isotope shift known as the *specific mass shift*. Since the cross term involves a correlation between the motions of electron pairs, this effect is very difficult to calculate for many electron atoms. For lighter elements the specific mass shift has the same order of magnitude as the normal mass shift. But in heavy elements, the effect is small.

C.3 Field Effect

Isotope shifts originating from the variations of the nuclear charge distribution from one isotope to another is referred to as field shifts. Such shifts are of physical significance because the measurement of field shifts in spectral lines helps one study the size and shape of nucleus as a function of neutron number. The field effects can be treated by understanding the electric monopole interaction between the nucleus and the electrons, and considering its departure (for real nuclei) from the pure coulomb potential of a point nuclear charge. To probe the nuclear charge distribution the s-electron must be considered whose charge density does not vanish in the region of the nucleus[1]. Then an isotope shift is expected in a spectral line for which the number of s-electrons is different in the

---

[1] Relativistically, $\mathrm{P}_{1/2}$ electrons also have a non-vanishing charge density in the region of nucleus. Other electrons with $l \neq 0$ have a negligible charge density.

two terms involved in the transition. Without considering relativistic and higher order perturbation treatment it is possible to estimate an order of magnitude of the field effects in heavy elements.

For simplicity we consider a nuclear model which assumes a spherically symmetric nuclear charge distribution. For example, the liquid drop model assumes a spherically symmetric nuclear charge distribution with radius r_0 given by

$$r_0 \simeq 1.2 \times A^{1/3} \text{ fm}. \tag{C.17}$$

We consider the isotope shift of a term for two isotopes whose nuclear radii differ by

$$\frac{\delta r_0}{r_0} = \frac{1}{3}\frac{\delta A}{A}. \tag{C.18}$$

This field effect, in particular, is known as *volume shift.* In first order, the contribution to the energy shift of a term for each electron is the expectation value of the electrostatic potential energy difference $V(r) - V(r_0)$, where $V(r)$ and $V_0(r)$ are the potential energies appropriate to an extended nucleus and to a point nucleus respectively. Thus,

$$\Delta E_{volume} = \int_0^\infty \psi^* \left[V(r) - V_0(r)\right] \psi 4\pi r^2 \mathrm{d}r \tag{C.19}$$

$$\simeq |\psi(0)|^2 \int_0^{r_0} \left[V(r) - V_0(r)\right] 4\pi r^2 \mathrm{d}r. \tag{C.20}$$

The range of integration is restricted to $0 \leq r \leq r_0$ since, by Gauss's theorem, $V(r) = V_0(r)$ for $r \geq r_0$ and over this range the electron charge density (ρ_e) is assumed to be approximately constant

$$\rho_e \simeq -e|\psi(0)|^2. \tag{C.21}$$

For a point nuclear charge

$$V_0(r) = -\frac{Ze^2}{4\pi\varepsilon_0 r} \qquad (\text{ r} > 0 \text{ }), \tag{C.22}$$

and, for a uniform nuclear charge distribution

$$V(r) = \frac{Ze^2}{4\pi\varepsilon_0 r_0}\left(-\frac{3}{2} + \frac{1}{2}\frac{r^2}{r_0^2}\right) \qquad (0 \leq \text{r} \leq \text{r}_0 \text{ }). \tag{C.23}$$

By substitution in Eq. C.20 and upon integration

$$\Delta E_{volume} = \frac{4\pi}{10}|\psi(0)|^2 \frac{Ze^2}{4\pi\varepsilon_0} r_0^2. \tag{C.24}$$

The quantity that is directly related to the observation of isotope shift is the difference in $\Delta\mathrm{E}_{volume}$ for the two isotopes

$$\delta(\Delta E_{volume}) = \frac{4\pi}{10}|\psi(0)|^2\frac{Ze^2}{4\pi\varepsilon_0}2r_0\delta r \tag{C.25}$$

$$= |\psi(0)|^2\frac{Ze^2}{5\varepsilon_0}r_0^2\frac{\delta r}{r_0} \tag{C.26}$$

$$= |\psi(0)|^2\frac{Ze^2}{15\varepsilon_0}r_0^2\frac{\delta A}{A} \qquad \text{using Eq. C.18.} \tag{C.27}$$

Hence the isotope shift caused by the volume effect is

$$\delta\tilde{\nu}_{volume} = \frac{\delta(\Delta E_{volume})}{hc} = |\psi(0)|^2\frac{Ze^2}{15hc\varepsilon_0}r_0^2\frac{\delta A}{A}. \tag{C.28}$$

Accurate determination of isotope shift through precision laser spectroscopy is an excellent way to probe nuclear shape and size, though it is necessary to know the absolute value of nuclear charge radius by another means.

Appendix D

Settings of the LEBL

Here the typical settings of various experimental parameters are recorded.

Table D.1: Settings of the low energy beam line and the linear Paul trap.

LEBL Component	HV Module	Channel A	Channel B
Lens A2	NIM08	0	1852
Wien Filter	NIM09	2890	2715
Bending Plate (Top/Bottom)	NIM10	2793	2818
Bending Plate (Left/Right)	NIM11	2808	180
Mirror	NIM24	1800	-
Einzel Lens 2 / Einzel Lens 1	NIM25	1650	1450

LEBL Component	HV Module	Channel Number							
		0	1	2	3	4	5	6	7
Bending Plate IN[a]	EHQ19	0	0	0	0	0	0	0	0
Bending Plate OUT[b]	EHQ20	115	85	32.5	25	0	0	0	0
Ion Trap DC Voltages	EHQ22	5	20	5	5	20	5	5	0

---

[a] Before Switch Point

[b] After Switch Point

LEBL Component	Setting
Drift Tube (After TI)	22 kHz, HV High: 84.0/30 kV, HV Low: 0 V
Drift Tube (Before Trap)	22 kHz, HV High : 80.6/30 kV, HV Low: −0.1 kV
Paul Trap	Frequency: 974.19 kHz, Voltage: 600 V (Peak-Peak)
Extraction TI	−6.85 kV
Deceleration Lens	−2.8 kV

Bibliography

[1] A. Salam. Gauge unification of fundamental forces. *Rev. Mod. Phys.*, 52(3):525, 1980.

[2] S. Glashow. Towards a unified theory: Threads in a tapestry. *Rev. Mod. Phys.*, 52(3):539, 1980.

[3] S. Weinberg. Conceptual foundations of the unified theory of weak and electromagnetic interactions. *Rev. Mod. Phys.*, 52(3):515, 1980.

[4] M.K. Gaillard, P.D. Grannis, and F.J. Sciulli. The Standard Model of particle physics. *Rev. Mod. Phys.*, 71(2):S96, 1999.

[5] M.J. Ramsey-Musolf. Nuclear science and the new Standard Model. *Nucl. Phys. A*, 805:138, 2008.

[6] S. Weinberg. *The quantum theory of fields. Vol. 3: Supersymmetry.* Cambridge University Press, 2000.

[7] C.T. Hill and E.H. Simmons. Strong dynamics and electroweak symmetry breaking. *Phys. Rept.*, 381:235–402, 2003.

[8] H. Georgi and S. L. Glashow. Unity of all elementary-particle forces. *Phys. Rev. Lett.*, 32(8):438–441, 1974.

[9] J. Polchinski. *String Theory.* Cambridge Univ. Press, 1998.

[10] M. Peskin and T. Takeuchi. Estimation of oblique electroweak corrections. *Phys. Rev. D*, 46(1):381–409, 1992.

[11] K. Jungmann. Fundamental symmetries and interactions - Some aspects. *Eur. Phys. J. A*, 25:677–683, 2005.

[12] K. Jungmann. Tests of fundamental symmetries and interactions using nuclei and lasers. *Hyperfine Interact.*, 171:41–55, 2006.

[13] K. Jungmann. Fundamental symmetries and interactions. *Nucl. Phys. A*, 751:87c–106c, 2005.

[14] H.W. Wilschut, U. Dammalapati, D.J. van der Hoek, K. Jungmann, W. Kruithof, C.J.G. Onderwater, B. Santra, P.D. Shidling, and L. Willmann. β-decay and the electric dipole moment: Searches for time-reversal violation in radioactive nuclei and atoms. *Pramana J. Phys.*, 75(1):163–170, 2010.

[15] H.W. Wilschut, D.J. van der Hoek, K. Jungmann, W. Kruithof, C.J.G. Onderwater, B. Santra, P. Shidling, and L. Willmann. β-decay and the electric dipole moment: Searches for time-reversal violation in radioactive nuclei and atoms. *Nucl. Phys. A*, 844:143C–149C, 2010.

[16] M. Sohani. Setup for precise measurements of β-decay in optically trapped radioactive Na. *Ph.D. Thesis, University of Groningen*, pages 1–180, 2008.

[17] S. De. Laser cooling and trapping of barium. *Ph.D. Thesis, University of Groningen*, pages 1–148, 2008.

[18] U. Dammalapati. Metastable D-state spectroscopy and laser cooling of barium. *Ph.D. Thesis, University of Groningen*, pages 1–156, 2006.

[19] E. Traykov. Production of radioactive beams for atomic trapping. *Ph.D. Thesis, University of Groningen*, pages 1–146, 2006.

[20] A. Rogachevskiy. Production and trapping of Na isotopes for beta-decay studies. *Ph.D. Thesis, University of Groningen*, pages 1–124, 2007.

[21] G.P.A Berg, P. Dendooven, O. Dermois, M.N. Harakeh, R. Hoekstra, K. Jungmann, S. Kopecky, R. Morgenstern, A. Rogachevskiy, R. Timmermans, L. Willmann, and H.W. Wilschut. TRIμP - A radioactive isotope trapping facility under construction at KVI. *Nucl. Instr. Meth. B*, 204:532, 2003.

[22] C.S. Wood, S.C. Bennett, D. Cho, B.P. Masterson, J.L. Roberts, C.E. Tanner, and C.E. Wieman. Measurement of parity nonconservation and an anapole moment in cesium. *Science*, 275(5307):1759–1763, 1997.

[23] S.C. Bennett and C.E. Wieman. Measurement of the 6S→7S transition polarizability in atomic cesium and an improved test of the Standard Model. *Phys. Rev. Lett.*, 82(12):2484–2487, 1999.

[24] S.C. Bennett, J.L. Roberts, and C.E. Wieman. Measurement of the DC stark shift of the 6S → 7S transition in atomic cesium. *Phys. Rev. A*, 59(1):R16–R18, 1999.

[25] B.K. Sahoo, L.W. Wansbeek, K. Jungmann, and R.G.E. Timmermans. Light shifts and electric dipole matrix elements in Ba^+ and Ra^+. *Phys. Rev. A*, 79(5):052512, 2009.

[26] L.W. Wansbeek, B.K. Sahoo, R.G.E. Timmermans, K. Jungmann, B.P. Das, and D. Mukherjee. Atomic parity nonconservation in Ra^+. *Phys. Rev. A*, 78(5):050501, 2008.

[27] J.S.M. Ginges and V.V. Flambaum. Violations of fundamental symmetries in atoms and tests of unification theories of elementary particles. *Phys. Rep.*, 397:63, 2004.

[28] W.J. Marciano and J.L. Rosner. Atomic parity violation as a probe of new physics. *Phys. Rev. Lett.*, 65(24):2963–2966, 1990.

[29] S.G. Porsev, K. Beloy, and A. Derevianko. Precision determination of electroweak coupling from atomic parity violation and implications for particle physics. *Phys. Rev. Lett.*, 102(18):181601, 2009.

[30] M.A. Bouchiat, J. Guena, L. Pottier, and L. Hunter. New observation of a parity violation in Cesium. *Phys. Lett. B*, 134(6):463–468, 1984.

[31] N. Fortson. Possibility of measuring parity nonconservation with a single trapped atomic ion. *Phys. Rev. Lett.*, 70(16), 1993.

[32] J.A. Sherman, A. Andalkar, W. Nagourney, and E.N. Fortson. Measurement of light shifts at two off-resonant wavelengths in a single trapped Ba^+ ion and the determination of atomic dipole matrix elements. *Phys. Rev. A*, 78(5):052514, 2008.

[33] T. Koerber. Measurement of light shift ratios with a single trapped $^{138}\mathrm{Ba}^+$ ion, and prospects for a parity violation experiment. *Ph.D. Thesis, University of Washington*, pages 1–240, 2003.

[34] E.P. Wigner. Events, laws of nature, and invariance principles. *Nobel Lectures Physics*, 1963-1970:6–17, 1963.

[35] T.D. Newton and E.P. Wigner. Localized states for elementary systems. *Rev. Mod. Phys.*, 21(3):400–406, 1949.

[36] H.A. Kramers. *Proc. K. Ned. Acad. Wet.*, 40:814, 1937.

[37] K. Blaum and F. Herfurth. Trapped charged particles and fundamental interactions. *Springer Lecture Notes in Physics 749*, pages 1–192, 2008.

[38] J. Schwinger. The theory of quantized fields I. *Phys. Rev.*, 82(6):914–927, 1951.

[39] T. Lee and C. Yang. Question of parity conservation in weak interactions. *Phys. Rev.*, 104(1):254, 1956.

[40] E.M. Purcell and N.F. Ramsey. On the possibility of electric dipole moments for elementary particles and nuclei. *Phys. Rev.*, 78(6):807, 1950.

[41] C. Wu, E. Ambler, R. Hayward, and D. Hoppes. Experimental test of parity conservation in beta decay. *Phys. Rev.*, page 1413, 1957.

[42] Y. Zeldovich. Nonconservation of first order parity in electron scattering and other effects with weak interaction constant. *Zhur. Eksptl'. i Teoret. Fiz.*, 9:682, 1959.

[43] M.A. Bouchiat and C.C. Bouchiat. Weak neutral currents in atomic physics. *Phys. Lett. B*, 48(2):111–114, 1974.

[44] T.W. Koerber, M. Schacht, W. Nagourney, and E.N. Fortson. Radio frequency spectroscopy with a trapped Ba^+ ion: recent progress and prospects for measuring parity violation. *J. Phys. B - At. Mol. Opt.*, 36(3):637–648, 2003.

[45] J.A. Sherman. Single barium ion spectroscopy: light shifts, hyperfine structure, and progress on an optical frequency standard and atomic parity violation. *Ph.D. Thesis, University of Washington*, pages 1–296, 2009.

[46] J.A. Sherman, T.W. Koerber, A. Markhotok, W. Nagourney, and E.N. Fortson. Precision measurement of light shifts in a single trapped Ba^+ ion. *Phys. Rev. Lett.*, 94(24):1–4, 2005.

[47] D. DeMille, D. Budker, and E.D. Commins. Measurement of the stark-induced amplitudes of the $6P_{1/2}{\rightarrow}7P_{1/2}$ transition in atomic Thallium. *Phys. Rev. A*, 50(6):4657–4670, 1994.

[48] S. Sanguinetti, J. Guena, M. Lintz, P. Jacquier, A. Wasan, and M.A. Bouchiat. Prospects for forbidden-transition spectroscopy and parity violation measurements using a beam of cold stable or radioactive atoms. *Eur. Phys. J. D*, 25(1):3–13, 2003.

[49] O.O. Versolato, G.S. Giri, L.W. Wansbeek, J.E. van den Berg, D.J. van der Hoek, K. Jungmann, W.L. Kruithof, C.J.G. Onderwater, B.K. Sahoo, B. Santra, P.D. Shidling, R.G.E. Timmermans, L. Willmann, and H.W. Wilschut. Laser spectroscopy of trapped short-lived Ra^+ ions. *Phys. Rev. A*, 82(1):010501, 2010.

[50] K. Tsigutkin, D. Dounas-Frazer, A. Family, J.E. Stalnaker, V.V. Yashchuk, and D. Budker. Observation of a large atomic parity violation effect in ytterbium. *Phys. Rev. Lett.*, 103(7):071601, 2009.

[51] K. Tsigutkin, D. Dounas-Frazer, A. Family, J.E. Stalnaker, V.V. Yashchuk, and D. Budker. Parity violation in atomic ytterbium: Experimental sensitivity and systematics. *Phys. Rev. A*, 81(3):032114, 2010.

[52] J.A. Sherman, T.W. Koerber, A. Markhotok, W. Nagourney, and E.N. Fortson. Precision measurement of light shifts in a single trapped Ba^+ ion. *Phys. Rev. Lett.*, 94(24):243001, 2005.

[53] D. DeMille. Parity nonconservation in the $6s^{2\,1}S_0 \rightarrow 6s5d\,^3D_1$ transition in atomic ytterbium. *Phys. Rev. Lett.*, 74(21):4165–4168, 1995.

[54] K. Jungmann. Good fortune from a broken mirror. *Physics*, 2:68, 2009.

[55] F. Hasert, S. Kabe, W. Krenz, and J. Von Krogh. Observation of neutrino-like interactions without muon or electron in the gargamelle neutrino experiment. *Phys. Lett. B*, 46(1):138, 1973.

[56] C. Prescott, W. Atwood, and R. Cottrell. Parity non-conservation in inelastic electron scattering. *Phys. Lett. B*, 77(3):347, 1978.

[57] P. Bagnaia, F. Bonaudi, and M. Borghini. Evidence for $Z^0 \rightarrow e^+e^-$ at the CERN $\bar{p}$p collider. *Phys. Lett.*, 129(1-2):130, 1983.

[58] G. Arnison, A. Astbury, B. Aubert, C. Bacci, and G. Bauer. Experimental observation of lepton pairs of invariant mass around 95 Gev/c^2 at the CERN SPS collider. *Phys. Lett. B*, 126(5):398, 1983.

[59] J. Erler and M.J. Ramsey-Musolf. Weak mixing angle at low energies. *Phys. Rev. D*, 72(7):073003, 2005.

[60] P. Anthony, R. Arnold, C. Arroyo, and K. Baird. Precision measurement of the weak mixing angle in moeller scattering. *Phys. Rev. Lett.*, 95:018601, 2005.

[61] G. Zeller, K. McFarland, T. Adams, and A. Alton. Precise determination of electroweak parameters in neutrino-nucleon scattering. *Phys. Rev. Lett.*, 88:091802, 2002.

[62] The ALEPH, the DELPHI, the L3, the OPAL, the SLD Collaborations, the LEP Electroweak Working Group, The SLD Electroweak, and Heavy Flavour Groups. Precision electroweak measurements on the Z resonance. *Physics Reports*, 427(5-6):257 – 454, 2006.

[63] A. Akhundov. Precision tests of electroweak interactions. *AIP Conf. Proc.*, 1006:43–48, 2008.

[64] P. Anthony, R. Arnold, C. Arroyo, and K. Baird. Observation of parity nonconservation in moeller scattering. *Phys. Rev. Lett.*, 92:181602, 2004.

[65] V. Dzuba and V. Flambaum. Calculations of parity-nonconserving S-D amplitudes in Cs, Fr, Ba^+, and Ra^+. *Phys. Rev. A*, 63(6):062101, 2001.

[66] M.A. Bouchiat and C.C. Bouchiat. Parity violation in atoms. *Rep. Prog. Phys.*, 60:1351–1396, 1997.

[67] A. Derevianko and S.G. Porsev. Theoretical overview of atomic parity violation. *Eur. Phys. J. A - Hadrons and Nuclei*, 32(4):517–523, 2007.

[68] E.N. Fortson. Atomic parity nonconservation experiments. *Physics Reports*, 113(5):289–344, 1984.

[69] M.J.D. Macpherson, K.P. Zetie, R.B. Warrington, D.N. Stacey, and J.P. Hoare. Precise measurement of parity nonconserving optical rotation at 876 nm in atomic bismuth. *Phys. Rev. Lett.*, 67(20):2784–2787, 1991.

[70] D.M. Meekhof, P. Vetter, P.K. Majumder, S.K. Lamoreaux, and E.N. Fortson. High-precision measurement of parity nonconserving optical rotation in atomic lead. *Phys. Rev. Lett.*, 71(21):3442–3445, 1993.

[71] P.A. Vetter, D.M. Meekhof, P.K. Majumder, S.K. Lamoreaux, and E.N. Fortson. Precise test of electroweak theory from a new measurement of parity nonconservation in atomic thallium. *Phys. Rev. Lett.*, 74(14):2658–2661, 1995.

[72] D.M. Lucas, R.B. Warrington, D.N. Stacey, and C.D. Thompson. Search for parity nonconserving optical rotation in atomic samarium. *Phys. Rev. A*, 58(5):3457–3471, 1998.

[73] C.E. Wieman. Parity nonconservation in atoms - Past work and trapped atom future. *Hyperfine Interact.*, 81(1-4):27–34, 1993.

[74] S. Sanguinetti, S.N. Atutov, R. Calabrese, L. Corradi, A. Dainelli, A. Khanbekyan, E. Mariotti, C. Mauro, P. Minguzzi, L. Moi, G. Stancari, L. Tomassetti, and S. Veronesi. Prospects for parity violation measurements in cold francium atoms. In *Proceedings of The 3rd Workshop From Parity Violation to Hadronic Structure*, pages 185–187. Springer Berlin Heidelberg, 2007.

[75] B.K. Sahoo, B.P. Das, R.K. Chaudhuri, D. Mukherjee, R.G.E. Timmermans, and K. Jungmann. Investigations of Ra^+ properties to test possibilities for new optical-frequency standards. *Phys. Rev. A*, 76(4):040504, 2007.

[76] E. Rasmussen. Serien im Funkenspektrum des Radiums Ra II. *Z. Phys. A - Hadrons and Nuclei*, 86(1-2):24–32, 1933.

[77] E. Rasmussen. Das bogenspektrum des Radiums. *Z. Phys. A - Hadrons and Nuclei*, 87(9-10):607–615, 1934.

[78] H. Russell. The spectrum and ionization potential of Radium. *Phys. Rev.*, 46(11):989–990, 1934.

[79] K. Wendt, S. Ahmad, W. Klempt, and R. Neugart. On the hyperfine structure and isotope shift of radium. *Z. Phys. D*, 4:227–241, 1987.

[80] S. Ahmad, W. Klempt, R. Neugart, and E. Otten. Determination of nuclear spins and moments in a series of radium isotopes. *Phys. Lett. B*, 133(1-2):47–52, 1983.

[81] W. Neu, R. Neugart, E. Otten, G. Passler, and K. Wendt. Quadrupole moments of radium isotopes from the $7^2P_{3/2}$ hyperfine structure in Ra II. *Z. Phys. D.*, 11:105–111, 1989.

[82] S.A. Ahmad, W. Klempt, R. Neugart, E.W. Otten, P.G. Reinhard, G. Ulm, and K. Wendt. Mean-square charge radii of radium isotopes and octupole deformation in the $^{220-228}$Ra region. *Nucl. Phys. A*, 483(2):244–268, 1988.

[83] E. Arnold, W. Borchers, M. Carre, H.T. Duong, P. Juncar, J. Lerme, S. Liberman, W. Neu, R. Neugart, E.W. Otten, M. Pellarin, J. Pinard, G. Ulm, J.L. Vialle, and K. Wendt. Direct measurement of nuclear magnetic moments of radium isotopes. *Phys. Rev. Lett.*, 59(7):771–774, 1987.

[84] R. Pal, D. Jiang, and M. Safronova. Calculation of parity-nonconserving amplitude and other properties of Ra^+. *Phys. Rev. A*, 79(6):062505, 2009.

[85] B.K. Sahoo, R.G.E. Timmermans, B.P. Das, and D. Mukherjee. Comparative studies of dipole polarizabilities in Sr^+, Ba^+, and Ra^+ and their applications to optical clocks. *Phys. Rev. A*, 80:062506, 2009.

[86] J. Emsley. *The elements.* Oxford Univ. Press, 1995.

[87] B.K. Sahoo, Md. R. Islam, and D. Mukherjee. Lifetimes of the metastable $^2D_{3/2,5/2}$ states in Ca^+ , Sr^+ , and Ba^+. *Phys. Rev. A*, 74(6):1–6, 2006.

[88] V.A. Dzuba and V.V. Flambaum. Calculation of nuclear-spin-dependent parity nonconservation in S-D transitions of Ba^+, Yb^+ and Ra^+ ions. *arXiv:1104.0086v1 [physics.atom-ph]*, 2011.

[89] L.W. Wansbeek. *Ph.D. Thesis, University of Groningen*, 2011.

[90] Web page of Accelerator and Ion Source Research at KVI, `http://www.rug.nl/kvi/Research/acceleratorPhysics/index`.

[91] P.D Shidling, G.S. Giri, D.J. van der Hoek, K. Jungmann, W. Kruithof, C.J.G. Onderwater, M. Sohani, O.O. Versolato, L. Willmann, and H.W. Wilschut. Production of short lived radioactive beams of radium. *Nucl. Instr. Meth. A*, 606(3):305–309, 2009.

[92] A. Gavron. Statistical model calculations in heavy ion reactions. *Phys. Rev. C*, 21(1):230–236, 1980.

[93] G.P.A. Berg, O.C. Dermois, U. Dammalapati, P. Dendooven, M.N. Harakeh, K. Jungmann, C.J.G. Onderwater, A. Rogachevskiy, M. Sohani, E. Traykov, L. Willmann, and H.W. Wischut. Dual magnetic separator for TRIμP. *Nucl. Instr. Meth. A*, 560(2):169–181, 2006.

[94] E. Traykov, A. Rogachevskiy, M. Bosswell, U. Dammalapati, P. Dendooven, O.C. Dermois, K. Jungmann, C.J.G. Onderwater, M. Sohani, L. Willmann, H.W. Wilschut, and A.R. Young. Production of radioactive nuclides in inverse reaction kinematics. *Nucl. Instr. Meth. A*, 572(2):580–584, 2007.

[95] O.B. Tarasov and D. Bazin. Lise++: Radioactive beam production with in-flight separators. *Nucl. Instr. and Meth. B*, 266(19-20):4657 – 4664, 2008.

[96] E. Traykov, U. Dammalapati, S. De, O.C. Dermois, L. Huisman, K. Jungmann, W. Kruithof, A.J. Mol, C.J.G. Onderwater, A. Rogachevskiy, M. da Silva e Silva, M. Sohani, O. Versolato, L. Willmann, and H.W. Wilschut. Development of a thermal ionizer as ion catcher. *Nucl. Instr. Meth. B*, 266(19-20):4478–4482, 2008.

[97] G. Savard et al. Development and operation of gas catchers to thermalize fusion-evaporation and fragmentation products. *Nucl. Instr. Meths. B*, 204:582 – 586, 2003.

[98] P. Dendooven, S. Purushothaman, and K. Gloos. On a cryogenic noble gas ion catcher. *Nucl. Instr. Meths. A*, 558(2):580 – 583, 2006.

[99] G. Bollen, D.J. Morrissey, and S. Schwarz. A study of gas-stopping of intense energetic rare isotope beams. *Nucl. Instr. Meths. A*, 550(1-2):27 – 38, 2005.

[100] Decay Data Home Page, Isotopes Project, Nuclear Science Division, LBNL, `http://ie.lbl.gov/decay.html`.

[101] P.D. Shidling, G.S. Giri, D.J. van der Hoek, K. Jungmann, W.L. Kruithof, C.J.G Onderwater, B. Santra, M. Sohani, O.O. Versolato, L. Willmann, and H.W. Wilschut. Thermalization of different alkali and alkali-earth elements at the TRIμP facility. *Nucl. Instr. Meth. A*, 622(1):11–16, 2010.

[102] W. Paul, H. Reinhard, and U. von Zahn. Das Elektrische Massenfilter als Massenspektrometer und Isotopentrenner. *Z. Phys. A - Hadrons and Nuclei*, 152(2):143–182, 1958.

[103] M. Knoop, M. Vedel, and F. Vedel. Collisional quenching and j-mixing rate constants for the 3D levels of Ca^+. *Phys. Rev. A*, 58(1):264–269, 1998.

[104] C.E. Wieman. Frequency stabilization of a diode laser using simultaneous optical feedback from a diffraction grating and a narrowband fabry–perot cavity. *Rev. Sci. Instrum.*, 1991.

[105] H. Patrick and C. Wieman. Using diode lasers for atomic physics. *Rev. Sci. Instrum.*, 62(11):25933–2595, 1991.

[106] P.A. Franken, A.E. Hill, C.W. Peters, and G. Weinreich. Generation of optical harmonics. *Phys. Rev. Lett.*, 7(4):118–119, 1961.

[107] C.J. Foot. *Atomic physics.* Oxford Univ. Press, 2005.

[108] S. Gerstenkorn, J. Verges, and J. Chevillard. *Atlas du spectre d'Absorption de la Molecule de d'iode*, CNRSII, Laboratoire Aim Cotton, 91405 Orsay (France)(11.000 cm^{-1}-14.000 cm^{-1} edition), 1982.

[109] U. Dammalapati, S. De, K. Jungmann, and L. Willmann. Isotope shifts of $6s5d\,^3D$-$6s6p\,^1P_1$ transitions in neutral barium. *Eur. Phys. J. D*, 53(1):1–8, 2009.

[110] J. Cariou and P. Luc. *Atlas du spectre d'Absorption de la Molecule de Tellure*, CNRS, Paris, 1980.

[111] Web page of CERN ROOT, `http://root.cern.ch/`.

[112] G.K. Woodgate. *Elementary Atomic Structure.* Oxford University Press, 1983.

[113] B.H. Bransden and C.J. Joachain. *The Physics of Atoms and Molecules.* Pearson Education Limited, 2003.

[114] A.-M. Mårtensson−Pendrill and A. Ynnerman. Isotope shift and nuclear charge radii of barium isotopes. *J. Phys. B*, 25:551, 1992.

[115] W.H. King. Peculiarities of the isotope shift in the samarium spectrum. *J. Opt. Soc. Am.*, 53(5):638, 1963.

[116] Atomic Weights and Isotopic Compositions, NIST Standard Reference Database 144, `http://www.nist.gov/pml/data/comp.cfm`.

[117] N. Yu, W. Nagourney, and H. Dehmelt. Radiative lifetime measurement of the Ba^+ metastable $D_{3/2}$ state. *Phys. Rev. Lett.*, 78(26):4898–4901, 1997.

[118] H.J. Metcalf and P. van der Straten. *Laser cooling and trapping*. Springer, 1999.

[119] H. Dehmelt. Radiofrequency spectroscopy of stored ions II: Spectroscopy. *Advances in Atomic and Molecular Physics*, 1969.

[120] O.O. Versolato. *Ph.D. Thesis, University of Groningen*, 2011.

[121] F. Major, V. Gheorghe, and G. Werth. *Charged Particle Traps: Physics and Techniques of Charged Particle Field Confinement*. Springer Series on Atomic, Optical, and Plasma Physics, 2005.

[122] P.K. Ghosh. *Ion Traps*. Oxford Univ. Press, 1995.

[123] W. Paul. Electromagnetic traps for charged and neutral particles. *Rev. Mod. Phys.*, 62(3):531–542, 1990.

[124] F. Penning. Die Glimmentladung bei niedrigem Druck zwischen koaxialen Zylindern in einem axialen Magnetfeld. *Physica Scripta*, 3(9):873–894, 1936.

[125] H. Dehmelt. Radiofrequency spectroscopy of stored ions I: Storage. *Advances in Atomic and Molecular Physics*, 1968.

List of Publications

1. *Isotope shifts of 6d* $^2D_{3/2}$ *- 7p* $^2P_{1/2}$ *transition in trapped short-lived* $^{209-214}Ra^+$, **G.S. Giri**, O.O. Versolato, J.E. van den Berg, O. Böll, U. Dammalapati, D.J. van der Hoek, K. Jungmann, W. Kruithof, S. Müller, M. Nuñez Portela, C.J.G. Onderwater, B. Santra, R.G.E. Timmermans, L.W. Wansbeek, L. Willmann, H.W. Wilschut,
   http://arxiv.org/abs/1108.0795, Accepted for Phys. Rev. A(R).

2. *Hyperfine structure of the 6d* $^2D_{3/2}$ *level in trapped short-lived* $^{211,209}Ra^+$ *ions*, O.O. Versolato, **G.S. Giri**, J.E. van den Berg, O. Böll, U. Dammalapati, D.J. van der Hoek, S. Hoekstra, K. Jungmann, W. Kruithof, S. Müller, M. Nuñez Portela, C.J.G. Onderwater, B. Santra, R.G.E. Timmermans, L.W. Wansbeek, L. Willmann, H.W. Wilschut,
   Phys. Lett. A **375**(35), 3130 (2011), DOI: 10.1016/j.physleta.2011.07.002.

3. *Atomic parity violation in a single trapped radium ion*,
   O.O. Versolato, L.W. Wansbeek, **G.S. Giri**, J.E. van den Berg, D.J. van der Hoek, K. Jungmann, W.L. Kruithof, C.J.G. Onderwater, B.K. Sahoo, B. Santra, P.D. Shidling, R.G.E. Timmermans, L. Willmann, and H.W. Wilschut,
   Hyperfine Interact, DOI: 10.1007/s10751-011-0296-6 (2011).

4. *Precision spectroscopy of trapped radioactive radium ions*,
   G.S. Giri, O.O. Versolato, L.W. Wansbeek, J.E. van den Berg, D.J. van der Hoek, K. Jungmann, W.L. Kruithof, C.J.G. Onderwater, B.K. Sahoo, B. Santra, P.D. Shidling, R.G.E. Timmermans, L. Willmann, and H.W. Wilschut,
   Can. J. Phys. **89**(1), 69 (2011), DOI: 10.1139/P10-089.

5. *Atomic parity violation in a single trapped radium ion*,
   O.O. Versolato, L.W. Wansbeek, **G.S. Giri**, J.E. van den Berg, D.J. van

der Hoek, K. Jungmann, W.L. Kruithof, C.J.G. Onderwater, B.K. Sahoo, B. Santra, P.D. Shidling, R.G.E. Timmermans, L. Willmann, and H.W. Wilschut,
Can. J. Phys. **89**(1), 65 (2011), DOI: 10.1139/P10-051.

6. *Thermalization of different alkali and alkali-earth elements at the TRIμP facility*,
   P.D. Shidling, **G.S. Giri**, D.J. van der Hoek, K. Jungmann, W. Kruithof, C.J.G. Onderwater, B. Santra, M. Sohani, O.O. Versolato, L. Willmann, H.W. Wilschut,
   Nucl. Instr. and Meth. A **622**, 11 (2010), DOI: 10.1016/j.nima.2010.07.048.

7. *Laser spectroscopy of trapped short-lived Ra$^+$ ions*,
   O.O. Versolato, **G.S. Giri**, L.W. Wansbeek, J.E. van den Berg, D.J. van der Hoek, K. Jungmann, W.L. Kruithof, C.J.G. Onderwater, B.K. Sahoo, B. Santra, P.D. Shidling, R.G.E. Timmermans, L. Willmann, H.W. Wilschut,
   Phys. Rev. A **82**, 010501(R) (2010), DOI: 10.1103/PhysRevA.82.010501.

8. *Production of short lived radioactive beams of radium*,
   P.D. Shidling, **G.S. Giri**, D.J. van der Hoek, K. Jungmann, W. Kruithof, C.J.G. Onderwater, M. Sohani, O.O. Versolato, L. Willmann, H.W. Wilschut,
   Nucl. Instr. and Meth. A **606**, 305 (2009), DOI: 10.1016/j.nima.2009.05.007.

Acknowledgment

The completion of this thesis would have been impossible without the guidance and knowledgable support of my co-advisor Dr. Lorenz Willmann and advisor Prof. Klaus Jungmann.

I would like to thank my doctor father, Klaus, for helping me enrich my knowledge base and expertise as an experimentalist. He is a great teacher and researcher with a unique spirit and scientific temperament. Klaus never allows a time interval between planning and execution and that makes him very special among his peers.

It was very educational and fun to work with my co-adviser, Lorenz. I learned from him how to work in the lab in a constructive way and how to keep an experimental set up tidy. Laboratory is the place where one can find him with highest probability. At times he works with more responsibility than the students and that makes him special among his peers.

I am grateful to Prof. Reinhard Morgenstern (Professor Emeritus, University of Groningen), Prof. Bhanu Pratap Das (Indian Institute of Astrophysics) and Prof. Gisbert zu Putlitz (Professor Emeritus, Physikalisches Institut, Universität Heidelberg) for spending their valuable time on careful reading of my thesis and for their constructive comments and suggestions.

I would like to thank the Foundation for Fundamental Research on Matter (FOM) and the Netherlands Organization for Scientific Research (NWO) for financially supporting this work. I am thankful to the Foundation FOM for being the source of my bread and butter for the last four years.

I would like to thank my colleagues Prof. Hans Wilschut, Prof. Ronnie Hoekstra, Prof. Rob Timmermans, Dr. Gerco Onderwater, Dr. Otto Dermois, Dr. Umakanth Dammalapati, Dr. Stefan Müller, Leo Huisman, Oliver Böll, Oscar Versolato, Lotje Wansbeek, Joost van den Berg, Bodhaditya Santra, Mayerlin

Nuñez Portela, Wilbert Kruithof, Duurt Johan van der Hoek, Dr. Steven Hoekstra, Hendrik Bekker, Corine Meinema, and Sophie Schlesser for their scientific help in the course of this work. I am also thankful to former colleagues Dr. Praveen Shidling, Dr. Moslem Sohani, Dr. Subhadeep De, Dr. Marlene da Silva e Silva, Sander Rikhof, Samuel Hoekman, Eric Prinsen, and Ulrike Wegner.

I am thankful to my colleagues Oscar, Duurt, and Rob for helping me write the Dutch summary ("Nederlandse Samevatting") of the thesis.

I would like to thank all my colleagues in the electronics, mechanical, electrical, vacuum, and IT departments of KVI for their help and cooperation. I am also grateful to the KVI administration, financial department and personnel department. As soon as I accepted the job offer from KVI, I started to get a very bad impression about procedures and paperworks in Dutch bureaucracy. I no longer have such a feeling because of Ms. Hilde van der Meer who took care of all the paperworks. I offer my special thanks to her.

I acknowledge my sincere thanks to Prof. Bhanu Pratap Das. He is the reason why I came to KVI. It was him who made me aware of the TRIμP research program. I am thankful towards Prof. Niranjan Barik who taught me to chant the mantra "I can do it". This powerful mantra is the driving force behind me. I bow my head before him.

I am thankful to my parents for their patience and support. I get a continuous flux of inspiration and encouragement from them. My father has always wanted me to be a medical doctor. I was unfortunate not to fulfill his dream. But after successful completion and defense of this PhD thesis I will be able to use those wonderful letters before my name which medical doctors use as well. I dedicate this thesis to my parents. I am also thankful to my relatives and friends for their support and encouragement. I must thank my wife Priyanka for her support and encouragement. Without her sacrifice I would not have been able to concentrate on my research work. I also thank my little daughter Lisanne for coming into my life and thereby bringing a lot of happiness for me.

Last but not the least, I am thankful to "Groningen", the only place on this planet which witnesses my evolution into a husband, a father, and a doctor.

Gouri Shankar Giri